united nations
educational, scientific
and cultural
organization

international atomic
energy agency

the
abdus salam
international centre for theoretical physics
40th anniversary
1964
2004

H4.SMR/1586-14

"7th Workshop on Three-Dimensional Modelling
of Seismic Waves Generation and their Propagation"

25 October - 5 November 2004

Inversion of Focal Mechanisms for Stress Field Determination

F.H. Cornet
Institut de Physique du Globe de Paris,
Paris, France

strada costiera, 11 - 34014 trieste italy - tel. +39 040 2240111 fax +39 040 224163 - sci_info@ictp.trieste.it - www.ictp.trieste.it

Inversion of Focal Mechanisms for Stress field determination

F.H. Cornet
Institut de Physique du Globe de Paris

Lecture notes prepared for

7th Workshop on three dimensional modeling of Seismic Waves Generation, Propagation and their inversion

UNESO Abdus Salam International Center for Theoretical Physics

Trieste; October 25 – November 5 2004

Table of content

One of the key variables involved in the understanding of deformation processes of the crust is stress. Because stresses are an essential boundary condition to many an applied engineering problem, be it mining, civil or petroleum, most techniques for determining stresses at depth have involved measurements in boreholes. But deformation processes in the crust involve depths that are generally not accessible to boreholes. Hence, methods based on remote observations are being developed for determining the stress field at depth greater than a few kilometers. Presently two methods are being used routinely, the analysis of shear wave polarization (shear wave splitting analysis) and the inversion of double couple focal mechanisms.

This presentation first recalls some elementary principles for stability analysis. Then two methods of fault plane solution inversions are presented. Examples where they have been applied are discussed. They help precise conditions that must be satisfied for the methods to be valid. It is shown that, when applied to microseismicity induced by fluid injections, they may help to map the pore pressure field. An example chosen from a geothermal field located on a creeping segment of the Philippine fault shows that this fault segment is normal to the regional **minimum** principal stress direction.

1.Elementary failure criteria for the crust

(Typing convention: bold letters are vectors, bold letters underlined by tilde are tensors)

1.1 the stress vector and the Mohr representation

The stress vector is defined by:

$$\mathbf{t} = \underset{\sim}{\boldsymbol{\sigma}}\,\mathbf{n}, \tag{1}$$

t is the stress vector acting on a surface element S, with normal **n** and unit area, on which exists at all points the stress tensor $\underset{\sim}{\boldsymbol{\sigma}}$. In this expression, the unit area is assumed to be small as compared to distances for which stress variations are significant so that stress gradients may be neglected. Hence, all components of the stress tensor are constant.

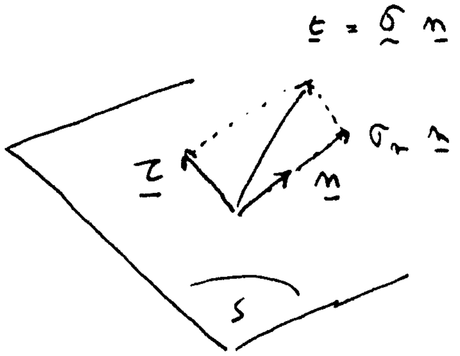

The stress vector has a normal component, (called the normal stress (scalar)) :

$$\sigma_n = \underset{\sim}{\sigma}\,\mathbf{n}\,.\,\mathbf{n} \tag{2}$$

and a shear component (vector):

$$\boldsymbol{\tau} = \underset{\sim}{\sigma}\,\mathbf{n} - (\underset{\sim}{\sigma}\,\mathbf{n}\,.\,\mathbf{n})\,\mathbf{n} \tag{3}$$

The stress tensor $\underset{\sim}{\sigma}$ is symmetrical when there exists no moment in any small volume of the body under consideration. Hence it is characterized by six components, i.e. σ_{ij} , with i, j = 1,2,3, the components in any frame of reference, or its eigen values (σ_1 , σ_2 , σ_3 , with the classical convention $\sigma_3 < \sigma_2 < \sigma_1$) and its eigen vectors **e**$_1$, **e**$_2$, **e**$_3$. The eigen vectors are defined by three independent angles, called the Euler angles, namely ψ , φ and θ. ψ and φ correspond to the azimuth and dip of **e**$_1$ in the frame of reference (defined by the unit vectors **I**$_1$, **I**$_2$, **I**$_3$, which may be the geographical frame of reference so that North is **I**$_1$, East is **I**$_2$, and **I**$_3$ is vertical positive downward). Once the frame of reference has been rotated so that **I**$_1$ becomes **e**$_1$ and **I**$_2$ becomes **I**$_2$' , θ is the rotation about **e**$_1$ which brings **I**$_2$' parallel to **e**$_2$.

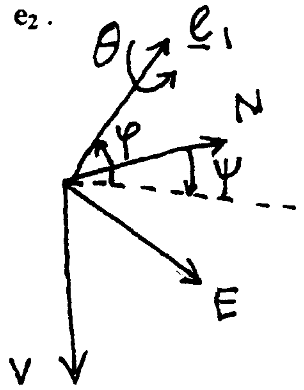

For **n** parallel to any eigen vector, $\tau = \mathbf{0}$. Given that σ_n and $|\tau|$ vary with the orientation of **n**, the set of all couples of values σ_n and $|\tau|$ corresponds to the area limited by the three Mohr circles as shown on figure 1.

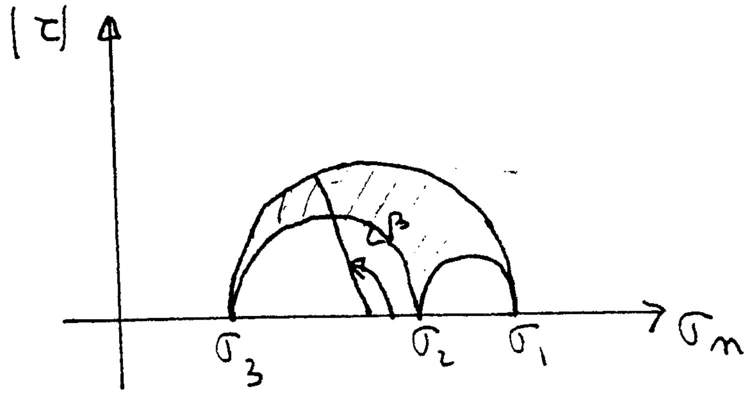

Figure 1 : The Mohr Circles. Each circle corresponds to the set of values for σ_n and $|\tau|$ when **n** is perpendicular to either **e**$_1$, **e**$_2$ or **e**$_3$.

When **n** is perpendicular to **e**$_2$, the values for σ_n and $|\tau|$ are :

$$\sigma_n = (\sigma_1 + \sigma_3)/2 + [(\sigma_1 - \sigma_3)/2] \cos(2\beta) \qquad (4)$$

$$|\tau| = [(\sigma_1 - \sigma_3)/2] \sin(2\beta) \qquad (5)$$

where β is the angle between the normal **n** and **e**$_1$ (see figure 1)

The rock mass is globally in equilibrium (i.e. in between slip events, whether seismic or aseismic), so that the stress components must satisfy the equilibrium equation:

$$\sigma_{ij,i} + \rho\, b_j = 0 \; ; \; i, j = 1,3 \qquad (6)$$

with $\mathbf{b} = g\delta_j 3\ \mathbf{I}_j$, the gravity, and ρ the rock density. Typically, for rocks, the vertical component of the vertical stress gradient is of the order of 2 to 3 mPa per 100 meters.

1.2. Stress failure criteria for rock masses submitted to compressive stresses

A rock mass involves both, intact rock volumes and preexisting fractures and faults. Hence failure criteria must address both the failure of intact rocks and that of preexisting weakness planes.

1.2.1 Criteria of failure for intact rocks

Once the minimum principal stress gets larger than 2 to 5 mPa, failure in compression involves the formation of macroscopic shear zones. Various stress criteria have been proposed to characterize the stress condition that must be met for these shear zones to appear.

The Tresca criterion.

$$(\sigma_1 - \sigma_3) = K \qquad (7)$$

The Tresca criterion assumes that failure occurs when the maximum differential stress in the material reaches a critical value, which is independent of the minimum principal stress magnitude. Note (see the Mohr representation on figure 2) that this assumes that the corresponding shear zone is inclined 45 ° to the maximum stress orientation. Laboratory work has shown that for rock, this is valid only for very soft material like clay or salt, or for stress and temperature conditions which, for most rocks, correspond to depths greater than 20 km. It is not valid for seismicity observed in the upper 10 to 15 km.

The Coulomb criterion and the Mohr envelope

$$|\tau| = \mu\, \sigma_n + C_0 \qquad (8)$$

μ is called the internal friction angle and C_0 is called the cohesion. This criterion has been found to be valid for limited stress domains. For large stress domains the so-called friction angle decreases as the minimum principal stress increases. It gets close to 0 when both the minimum principal stress and the temperature gets large so that the criterion of failure gets close to the Tresca criterion (see figure 2). Hence the failure criterion is not represented by the simple linear law proposed by Coulomb but may be approached by a parameterization of the so-called Mohr envelope. This envelope corresponds to the set of values for $|\tau|$ and σ_n for which failure occurs. It is often assumed to be independent of the intermediate principal stress magnitude, so that failure surfaces are assumed to be parallel to the intermediate principal stress direction. However recent laboratory work, in particular by Haimson et al.(1997), has shown this not always to be valid. This will not be discussed further here for it has no incidence for our discussion

The effective stress principle

When the rock mass is saturated with a fluid under pressure, experiments show that, under compressive conditions, failure is controlled by so-called effective stresses rather than by total stresses. The effective stress tensor $\underset{\sim}{\sigma}'$ is defined as :

$$\underset{\sim}{\sigma}' = \underset{\sim}{\sigma} - P\underset{\sim}{I} \tag{9}$$

where **I** is the unit tensor and P is pore pressure. Note that, on the Mohr diagram, subtracting P to all diagonal terms of the stress tensor matrix corresponds to shifting all Mohr circles to the left, leaving unchanged their radius.

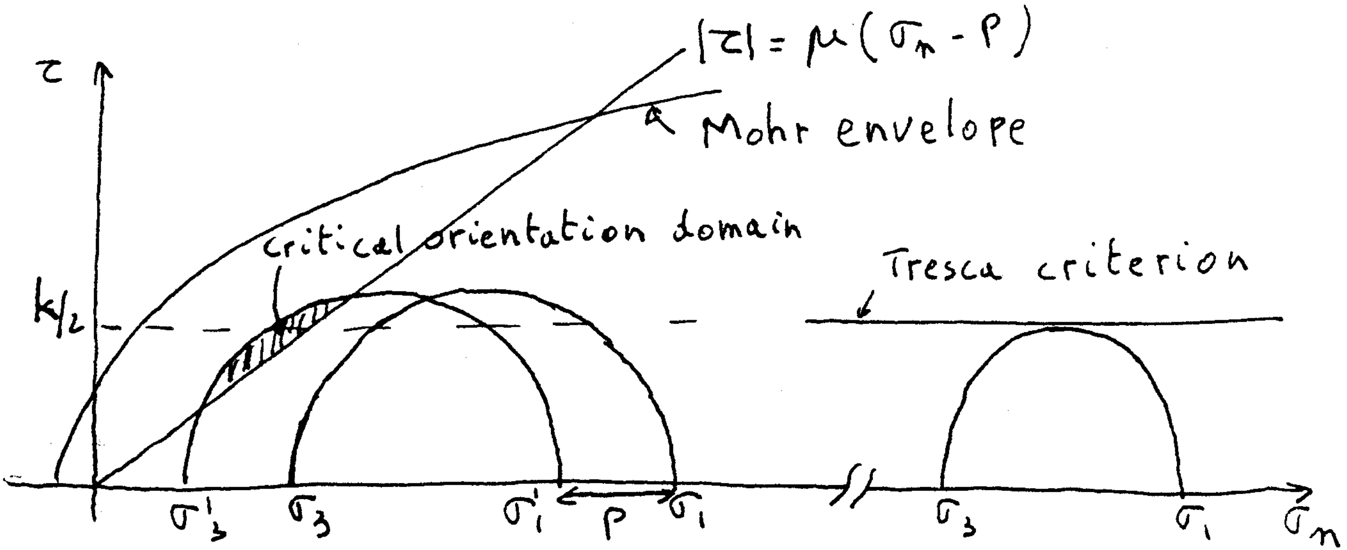

Figure 2 Description of failure conditions in a rock mass. It includes both, failure in the intact rock and failure along preexisting weakness planes as expressed in terms of effective stresses.

1.2.2 Failure along preexisting weakness planes

It is generally accepted that failure along preexisting planes is well represented by Coulomb's friction law, expressed in terms of effective stresses :

$$|\tau| = \mu(\sigma_n - P) + C_0 \tag{10}$$

Byerlee (1978) has shown that for most rocks the friction coefficient ranges from 0.6 to 0.9. For wet rocks, most field data point out to values for the friction coefficient ranging from 0.6 to 0.8 and negligible cohesion, so that the failure along preexisting weakness planes at depths greater than a few hundred meters is well represented by Byerlee's law :

$$|\tau| = \mu(\sigma_n - P);\ 0.6 \leq \mu \leq 0.8 \tag{11}$$

It may be noted that $|\tau|$ and σ_n are computed for the corresponding weakness plane. Hence, it is possible for the Mohr circles to intersect the line which corresponds to Byerlee's law and yet to observe stability. This is possible if there is no preexisting plane in the critical orientation domain. However, it has been argued that fractured rock masses have a long enough tectonic history that there always exists a plane with critical orientation. Hence it is often considered that the Mohr circle representing the stress at any point in the rock mass is at most tangent to the straight line which corresponds to Byerlee's law.

Let us observe that, because sliding depends on effective stresses, planes with a great variety of orientations may slip if the local pore pressure becomes large enough, as pointed out by McKenzie (1969).

The equilibrium of rock masses is classically analyzed with a Mohr diagram as shown on figure 2. Note that failure along preexisting weakness planes is the controlling phenomenon in most cases. An important difference between the development of new shear zones and the slipping along preexisting weakness planes, is that the orientation of new shear planes may be determined from the principal stress directions, if the corresponding internal friction coefficient is known (the Mohr circle at rupture is tangent to he Mohr envelope), but this is not true for preexisting weakness planes, given the role of pore pressure.

It is concluded that seismicity occurring in the upper 15 to 20 km of the crust involves fracture planes that make an unknown angle with respect to the principal stress directions.

In the above discussion, the friction angle and the cohesion are isotropic so that, if slip occurs, it will occur in the direction of the resolved shear stress (τ) in the plane (Bott, 1959). But this direction of resolved shear stress depends on the relative orientation of the slip plane with respect to the principal directions as well as on the relative magnitude of principal stress components. This is the basic principle underlying stress determinations from a collection of fault planes solutions.

2. Inversion of double couple focal mechanisms for stress determination

2.1 data produced by Fault plane solutions

Focal mechanisms of pure shear faults (pure double couples, no significant dilatancy), yield for both nodal planes the dip and azimuth of the plane (d and a) as well as the slip direction in the plane (rake angle r of slip vector s) when it corresponds to the fault plane.

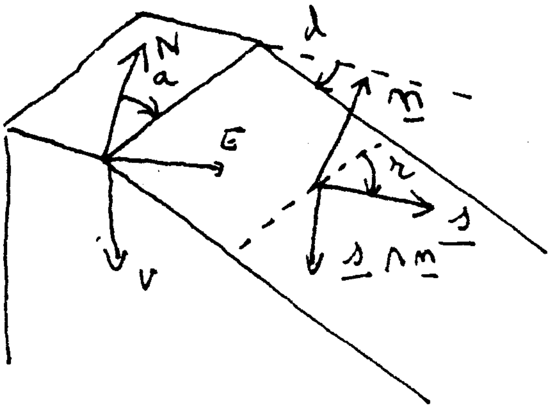

But it is impossible to identify which of the two nodal planes is the actual fault plane, if only the polarity of P waves is considered. The method proposed by Zollo and Bernard (1989, 1991) for determining focal plane solutions conducts an exhaustive search of all possible solutions and each solution is associated with a probability. Hence solutions with 60 %, 90 % and 99 % confidence levels are determined. These confidence level domains are used then to determine the corresponding uncertainty associated with the various angles determination.

Note that when enough three components stations are being used, the radiation pattern for S waves helps identify the fault plane. In the following, it is considered that the fault plane has not been identified so that both nodal planes are equally likely to be the fault plane. Hence for each focal mechanism, a set of 12 values is identified : (a_1, d_1, r_1, εa_1, εd_1, εr_1 , a_2, d_2, r_2, εa_2, εd_2 , εr_2).

It is customary to identify P and T axis with focal mechanisms. These are inclined 45° with respect to the nodal planes. It has been proposed sometimes to associate these axes respectively with the maximum and minimum principal stress direction. It should be noted here that, only when failure occurs according to the Tresca failure criterion (i.e. for very deep earthquakes) is this proposition valid. Hence this proposition is erroneous for most seismic events of the upper crust since either these correspond to the reactivation of preexisting weakness planes, or the newly formed shear zones are inclined by less than 45° with respect to the maximum principal stress orientation.

2.2 Determination of the regional stress field from focal mechanisms

Gephart and Forsyth's approximate method

The method (Gephart and Forsyth, 1984) is based on the following assumptions :

1. Slip occurs parallel to the direction of the resolved shear stress;
2. All seismic events are distant enough from each other that the stress perturbation induced by each event does not alter the stress field for other events;
3. The original stress field is uniform within the volume sampled by the various events.

Validity of hypothesis 1 implies that the shear strength in all planes is isotropic while hypothesis 3 implies that events are not too distant from each other so that stress gradients may be neglected. This has implication for the depth ranges of events considered for a single inversion.

Because focal mechanisms yield only the direction (and sense) of slip and not the magnitude, the stress tensor cannot be fully determined. Only four parameters are determined : the three Euler angles and an aspect ratio R defined as :

$$R = (\sigma_2 - \sigma_1) / (\sigma_3 - \sigma_1) \qquad (12)$$

So that $0 \leq R \leq 1$. Indeed, the stress at any point may be rewritten :

$$\sigma = \sigma_1 \; I + (\sigma_3 - \sigma_1) \, T \qquad (13)$$

with :

$$(T) = \begin{pmatrix} 0 & 0 & 0 \\ 0 & R & 0 \\ 0 & 0 & 1 \end{pmatrix}$$

so that $\underset{\sim}{\mathbf{T}}$ is characterized by 4 parameters (ψ , φ , θ , R). Note that ψ ranges from 0 to 360 °, while the range for φ is 90° and that for θ is 180°. Hence, the complete set of solutions for $\underset{\sim}{\mathbf{T}}$ is fairly limited and it can be fully explored with a grid search method. The solution is that which fits best the collection of focal mechanisms.

Let us determine now the condition for $\underset{\sim}{\mathbf{T}}$ to be consistent with a given focal mechanism, i.e. the tensor $\underset{\sim}{\mathbf{T}}$ for which the resolved shear stress τ_0 on a fault plane is parallel to the observed slip vector s. First it will be noted that $\tau_0 . s > 0$.

We consider now two frames of reference : the first one (R) is associated with the eigen vectors of $\underset{\sim}{\mathbf{T}}$. The second one (R') is associated with the fault plane (**n** , s $\wedge$ **n** , s).

Let $\underset{\sim}{\beta}$ be the orthogonal tensor which rotates R to R'. It may be observed that in R', the stress component σ'_{12} is null. Hence, given the definition of R, we obtain :

$$\sigma'_{12} = \sigma_1 \beta_{11} \beta_{21} + \sigma_2 \beta_{12} \beta_{22} + \sigma_3 \beta_{13} \beta_{23} = 0 \qquad (14)$$

so that

$$R = (\sigma_2 - \sigma_1) / (\sigma_3 - \sigma_1) = - \beta_{13} \beta_{23} \; / \; \beta_{12} \beta_{22} \qquad (15)$$

For a given fault plane defined by the triplet (a, d, r), and given a tensor $\underset{\sim}{\mathbf{T}}$ with Euler angles ψ , φ , θ, there is a unique value of R which fits the direction of slip in the corresponding plane. This is taken to advantage for identifying both the best solution $\underset{\sim}{\mathbf{T}_s}$ for the given set of focal mechanisms and its domains of confidence level.

The idea is to explore the set of possible solutions and to identify that which fits best observations, namely the tensor, which yields resolved shear stress directions closest to observed slip vector directions. The problem is three folds :

1. Identify for each focal mechanism which nodal plane is the fault plane;

2. For all focal mechanisms define a measure of their misfit with a given tensor $\underset{\sim}{\mathbf{T}}$.

3. Identify the best solution and associated confidence level domains.

The measure of misfit and the identification of fault planes

It has been proposed sometimes to characterize the misfit between a given fault plane and a given tensor $\underset{\sim}{\mathbf{T}}$ by the angle between the shear stress resolved on that plane and the observed slip vector. But this assumes that the fault plane is known exactly while in reality this is not the case as mentioned here above. Gephart and Forsyth (1984) proposed to consider as measure of misfit, for any given plane, the smallest rotation which brings s parallel to the resolved shear stress in the plane (τ). They observe that this misfit is a well behaved function so that it suffices to consider only three rotations axis, namely **n**, s $\wedge$ n and **s.**

The rotation angles are computed according to equation (15) once R' has been replaced by the frame of reference R" that corresponds to the rotated R' :

$$\underset{\sim}{R}'' = \underset{\sim}{\alpha}(i)\,\underset{\sim}{R}' \qquad (16)$$

where $\underset{\sim}{\alpha}(i)$ is the orthogonal tensor corresponding to rotations about **n**, s ∧ n or s . The angles of rotation are given here below :

Table 1

Expressions for rotations about axes of fault plane geometry.

Rotation axis	Algorithm	Period
n	$\theta = -\tan^{-1}\left[\dfrac{RB_{12}B_{22} + B_{13}B_{23}}{RB_{12}B_{32} + B_{13}B_{33}}\right]$	Π
s ∧ n	$\theta = \tan^{-1}\left[\dfrac{RB_{12}B_{22} + B_{23}B_{13}}{RB_{22}B_{32} + B_{23}B_{33}}\right]$	Π
s	$\theta = \dfrac{1}{2}\tan^{-1}\left(\dfrac{2}{k}\right)$	
	where $k = \dfrac{R(B_{12}^2 - B_{22}^2) + B_{13}^2 - B_{23}^2}{RB_{12}B_{22} + B_{13}B_{23}}$	$\dfrac{\Pi}{2}$

For any given $\underset{\sim}{T}$ and any focal mechanism six rotation angles are computed : 3 for the first nodal plane and 3 for the second nodal plane. The nodal plane which yields the smallest rotation is chosen as fault plane and the measure of misfit for the corresponding plane is the smallest rotation. Hence, the misfit value associated to any given $\underset{\sim}{T}^{(i)}$, is the sum of the misfit measures for all focal mechanisms. It is given by :

$$m_i = \sum_{k=1}^{N} \min(x_k^l, l = 1,6) \qquad (17)$$

where x_k^1 is the 1th rotation for focal plane solution k.

The solution is the tensor for which m_i is minimum. The corresponding value for the misfit is noted m_{min}. Here, the L_1 norm has been chosen rather than a least squares norm. Indeed, the choice of the nodal plane as fault plane is either right or wrong so that the error associated with the rotation angle determination does not obey a Gaussian law.

It has been proposed (Julien and Cornet, 1987) to introduce weight factors in the misfit function by dividing the minimum rotation angle by the uncertainty on the orientation of the nodal plane as defined by the focal mechanism determination. Also, when the rotation angle is larger than the solid angle that corresponds to the 90 % confidence level for the fault plane orientation, the focal mechanism is considered to be heterogeneous with the corresponding tensor. Then the quality of the solution is defined not only by the misfit value but also by the number of inconsistent data. Indeed, it may be argued that a solution which requires very small rotation angles but is heterogeneous with more than 50 % of the data is not satisfactory.

Let m_{50} and m_{90} be the values for the bounds of the misfit function which characterize respectively the 50 % and the 90 % confidence levels. For the L1 norm, Parker and McNutt (1980) have showed that these bounds may be defined with respect to the best solution as :

$$m_{90} = \{\ [1.645(\pi/2-1)^{1/2} N^{1/2} + N\ ] / (N-k)\}\ m_{min} \qquad (18)$$

and

$$m_{50} = \{\ [0.676(\pi/2-1)^{1/2} N^{1/2} + N\ ] / (N-k)\}\ m_{min} \qquad (19)$$

where k is the number of parameters in the model (here k= 4) and N is the total number of focal mechanisms.

Hence, all solutions for which the misfit m_i is found to be smaller than either m_{50} or m_{90} are plotted on a stereo net. The contour plot of these solutions identifies the 50 and 90 % confidence levels.

Once the approximate solution and its associated confidence levels are known, fault planes have been identified for each focal mechanism. Cornet and Julien (1987) have proposed a method based on a least squares method for identifying the best solution, once the approximate solution is known. However, experience has shown that this refining of the solution is not necessary for the solution remains within the 50 % confidence level domain. It suffices to run the approximate method with a finer grid restricted to the 90 % confidence level domain.

Stress determination in large volumes

When inverting for tensor $\underset{\sim}{\mathbf{T}}$, it is assumed that the stress is uniform throughout the volume sampled by the various focal mechanisms. But, if only because of gravity, it is known that the stresses vary with depth and possibly also laterally. Hence the question arises as to the validity of this hypothesis.

Interestingly, most stress field measurements have shown that the stress varies linearly with depth. Further, as shown by Mc Garr (1980), when there is no lateral stress variation, the vertical direction is principal. Hence, in many a situation, the stress field may be written :

$$\underset{\sim}{\sigma}(x_3) = \underset{\sim}{\sigma}(x_c) + (x_3 - x_{3c})\ \underset{\sim}{\alpha} \qquad (20)$$

where $\underset{\sim}{\sigma}(x_3)$ is the stress at depth x_3, $\underset{\sim}{\sigma}(x_c)$ is the stress at the reference depth x_c (6 independent components) and $\underset{\sim}{\alpha}$ is the vertical stress gradient (six independent components which reduce to 4 independent components, namely the three eigen values and the orientation of one of the horizontal eigen vectors, when there is no lateral stress variation).

Equation (20) has revealed very useful for interpreting direct stress measurements in boreholes. Indeed, it is usually found that close to ground surface many perturbations of the stress field exist whichmay be lumped as a fixed term for a given depth interval. But, as depth gets larger, the gradient term becomes more significant so that, when depth gets greater than 1 km, it may be considered that the vertical stress gradient dominates the stress field and that the constant term may be neglected. When this is the case, then the stress field can again be simplified so as to be characterized by only four parameters, namely the three Euler angles and the R aspect ratio. However, now, R describes the aspect ratio of the vertical stress gradient and not the complete stress tensor at depth z ;

$$R = (\alpha_2 - \alpha_1) / (\alpha_3 - \alpha_1) \qquad (21)$$

Given that usually the rock mass density α_3, is rather well known, the determination of the ratio R provides constraints on the relative variations of both horizontal stress components when there is no lateral stress variation.

This observation opens the door now to a possibility of extrapolating borehole stress determinations, which are usually conducted in the upper kilometer of the crust, down to depths of natural microseismic activity. This is possible provided the stress gradient is continuous and stable for the complete depth interval. Hence the mapping of the complete stress field at the scale of the crust may become realistic, when combining borehole data and focal mechanisms of natural seismicity.

2.3 Integrating focal plane solutions with other data for a complete stress determination

A great diversity of methods has been developed for determining the stress field in the vicinity of boreholes (Cornet, 1993). One of the most efficient such method is hydraulic fracturing and its generalization, the so-called Hydraulic Test on Preexisting Fractures (HTPF) method. The HTPF method basically provides measurements of the normal stress supported by fractures of known orientation (Cornet, 1993).

It has been applied to investigate the validity of stress determination from focal mechanisms of microseismic events induced by large fluid injections. In this example, microseismic events are within the same volume as that in which the stress measurements have been conducted. This is presented in the two following papers. In the first one, the method for integrating HTPF results with focal mechanisms is presented. In the second paper, results from the induced seimicity experiment are presented together with a brief overview of the HTPF method. The joint inversion helps characterize the stress field as well as the pore pressure field in the rock mass. In addition, it points out the fact that natural faults are zones of local stress heterogeneity so that microseismic events which occur within major fault zones may not be representative of the regional stress away from the fault. Orders of magnitudes for the stress heterogeneity are presented.

References

Bott B., 1959, The mechanics of oblique slip faulting, Geol. Mag., vol 96, nb 2, pp 109-117

Byerlee J., 1978, Friction of rocks, Pure and App. Geophys., vol 116, pp 615-626

Cornet F.H.; 1993; Stresses in Rock and Rock Masses; Comprehensive Rock Engineering (Hudson ed.), vol. 3, ch. 12, pp 297-327, Pergammon Press Oxford.

Cornet F.H.; 1993; The HTPF and the Integrated stress determination methods; Comprehensive Rock Engineering (Hudson ed.); Vol 3, ch. 15, pp 413-432 Pergammon Press, Oxford.

Gephart J.W. and D.W. Forsyth, 1984, An improved method for determining the regional stress tensor using earthquake focal mechanism data : application to the SanFernando earthquake sequence, jou. Geophys. Res., vol 89, nb b11, pp 9305-9320

Julien Ph. and F.H. Cornet; 1987; Stress Determination from Aftershocks of the Campania-Lucania Earthquake of November 23, 1980; Ann. Geoph., vol. 5b, no 3, pp 289-300.

Mc Garr A., 1980, Some constraints on levels of shear stress in the crust from observation and theory, Jou. Geophys. Res., vol. 85, p 6231

McKenzie D.P., 1969, The relation between fault plane solutions for earthquakes and the directions of principal stresses, Bull. Seism. Soc. Am., vol 59, nb 2, pp 591-601

Parker R. L. and M.K. McNutt; 1980, Statistics or the one norm misfit measure, Jou. Geophys. Res., vol 85, p 4489.

Zollo A and P. Bernard; 1989, S-wave polarization inversion of the 15 October 1979, 23:19 Imperial Valley aftershock : evidence for anisotropy and a single source mechanisms, Geophys. Res. Let., vol 16, pp 1047-1050

Zollo A and P. Bernard, 1991, How does an asperity break/new elements from the wave form inversion of accelerograms for the 2319 UT, October 15, 1979 Imperial valley after shock, Geophys. Res. Let. Vol 23, pp 111-126

GEOPHYSICAL RESEARCH LETTERS, VOL. 21, NO. 24, PAGES 2645-2648, DECEMBER 1, 1994

Integrated stress determination by joint inversion of hydraulic tests and focal mechanisms

J. M. Yin and F. H. Cornet
Département de Sismologie, Institut de Physique du Globe de Paris

Abstract. An inversion method, based on a genetic algorithm, is proposed for interpreting jointly various kinds of stress data in order to overcome the limitation, in number and quality, of each data set. The method has been applied to results from hydraulic tests in boreholes and to focal mechanisms of induced seismicity observed within the same depth interval. The regional stress field is described by two symmetrical tensors. The first one represents the stress at a given depth and the second one the vertical stress gradient. Results indicate that one of the principal directions is vertical. They are consistent with all but one of the hydraulic tests considered in the inversion and with about 70% of the focal mechanisms. This inversion confirms previous results suggesting that, for the scale of these induced microseismic events, the regional stress field cannot be determined solely from an inversion of the fault plane solutions.

Introduction

Many techniques have been developed for determining the natural stress field at depth but none of them yield directly all the stress components. Further, because these techniques seldom provide means to assess the precision of the determination, investigators often try to compare results obtained by more than one technique (Barton et al., 1988; Haimson et al., 1989).

We present in this paper a method for inverting jointly hydraulic test measurements and focal mechanisms of induced microseismicity obtained within the same depth interval.

Data and separate determinations

The granite test site at Le Mayet de Montagne, in central France, has been developed for conducting large scale in-situ experiments on forced water circulation. The stress field was investigated by the Hydraulic Tests on Preexisting Fractures (HTPF) method which is based on measurements of the normal stress supported by various preexisting fractures of known orientation (Cornet and Valette, 1984). Prior to the water circulation experiments, 18 HTPF measurements were conducted in various boreholes at the site. They have been successfully inverted with a stress field model which assumes a vertical principal direction throughout the volume of interest and a linear variation with depth. The results are consistent with the regional stress field determined in neighbouring sites (Cornet and Burlet, 1992). Two years after the water circulation tests had been completed, another 13 HTPF measurements were conducted. They are quite consistent with the stress field initially determined except for two tests located near one of the most hydraulically conductive zones (Scotti and Cornet, 1994).

The water injections induced some microseismicity which was monitored with a network of fifteen 3-D seismic stations (Cornet and Julien, 1989; Cornet et al., 1992). About 200 events were recorded and located with more than 12 P waves and 10 S waves arrivals. Out of these, 87 events yield well constrained fault plane solutions characteristic of shear slip (i.e. two nodal planes with standard deviation generally less than 10° on their strike and dip determination). For the remaining events, only one nodal plane was determined because of insufficient or poor spatial coverage of polarity measurements.

These focal mechanisms were separated into two groups corresponding respectively to the 70-hour initial injection and to the large scale circulation test which lasted four months in total. For both sets of focal mechanisms, the regional stress field has been determined using Julien and Cornet's inversion method (1987) which is derived from that initially proposed by Gephart and Forsyth (1984). The slip vector in the fault plane is assumed to be parallel to the resolved shear stress supported by the plane. The principal directions and a shape factor R $((\sigma_2-\sigma_1)/(\sigma_3-\sigma_1))$ are supposed to be uniform throughout the volume considered. The inversion of the focal mechanisms obtained during the preliminary injection yields a solution significantly different from that obtained with the HTPF data (Cornet and Julien, 1989). Scotti and Cornet (1994) have suggested that some microseismic events induced by this injection were associated with local stress heterogeneities. Indeed, results obtained from the microseismic events observed during the subsequent large scale injection revealed nearly consistent with the HTPF solution (Cornet et al., 1992; Yin, 1994). However, these results are only fairly constrained. Also, for the various depth intervals, the maximum horizontal principal stress direction exhibits a systematic clockwise rotation equal to about 30° in comparison with the HTPF solution. Such discrepancy may be due to the parameterization difference between the two methods. In order to alleviate the hypotheses associated with each determination technique taken alone, a joint inversion has been attempted.

Joint inversion method

Parameterization. Because of the absence of strong topography and because of the homogeneity of the granite, we adopt a stress model with linear vertical variation but with no variation in horizontal directions. No assumption is made concerning the verticality of one principal stress, unlike in the previous model chosen for fitting only the HTPF data. Thus ten parameters suffice to represent the stress field $\sigma(z)$: $\sigma(z) = S_{z_0} + (z - z_0)\alpha$. Here S_{z_0} is the stress tensor at a given depth z_0, α is the vertical gradient tensor. S_{z_0} is characterized by three principal values (S_1, S_2 and S_3) and three Euler angles (λ_1, λ_2 and λ_3). From equilibrium conditions it is found that the horizontal uniformity assumption implies that the vertical direction is principal for α. So α is characterized by four parameters: three principal values (α_1, α_2 and α_3) and the azimuth (η) of the maximum horizontal principal component (α_1).

Inversion strategy. Our objective is to search for the optimal solution and its confidence limit. The inversion of

Paper number 94GL02584
0094-8534/94/94GL-02584$03.00

focal mechanisms is a non-linear problem and this makes the joint inversion also non-linear, so that an extensive exploration of the model space is required. The minimum absolute criterion (ℓ_1-norm) is adopted for the measurement of misfit. Given the diversity of data considered in the inversion, this criterion has been shown to exhibit a stronger robustness than the least squares criterion (e.g. Tarantola, 1987).

Misfit function. A dimensionless misfit function is defined to deal with different data sets. Let Φ_h be the measure of misfit associated with the N HTPF data:

$$\Phi_h = \sum_{i=1}^{N} |\sigma^i_{no} - \sigma^i_{np}|/\delta^i_h \qquad (1)$$

where σ^i_{no} is the observed normal stress for the ith HTPF datum, σ^i_{np} is the predicted one, δ^i_h is the sum of the standard deviation associated with σ^i_{no} and another term representing the uncertainty on the normal stress because of the error associated with the identification of the normal to the corresponding fracture plane.

For the jth focal mechanism, let χ^j be the minimum rotation angle that brings the observed slip vector into coincidence with the resolved shear direction as computed for the currently tested stress model. Following Gephart and Forsyth's approximate method (1984), the minimum angle is searched among three orthogonal rotations (one about the slip vector **s**, one about the normal to the nodal plane **n** and one about the axis coaxial with **n**×**s**) for each of the two nodal planes. The fault plane is chosen to be the nodal plane which requires the smallest rotation. The measure of misfit Φ_f associated with M focal mechanisms is:

$$\Phi_f = \sum_{j=1}^{M} |\chi^j|/\delta^j_f \qquad (2)$$

δ^j_f is the standard deviation associated with the evaluation of the nodal plane geometry.

Because the number of data of one kind is generally different from that of the other kind and also, because the error range is fairly different for the two data sets, weighting factors for the two measures of misfit are introduced in the global misfit function. First, the two sets of data are inverted separately so as to estimate, for each data set, the largest number of data (N_c^{max} and M_c^{max}) consistent with the stress model as well as the corresponding minimum measure of misfit (Φ_h^{min} and Φ_f^{min}) as defined by (1) and (2). The criterion for consistency is defined by assuming that errors are normally distributed and by rejecting data which do not belong to the 99% confidence level. Then, we define the measure of global misfit so as to give an equal weight to each data set by normalizing the two measures of misfit separately:

$$\Phi_s = \frac{1}{2}\frac{N_c^{max}}{N_c}\frac{\Phi_h}{\Phi_h^{min}} + \frac{1}{2}\frac{M_c^{max}}{M_c}\frac{\Phi_f}{\Phi_f^{min}} \qquad (3)$$

N_c and M_c are the number of data which are consistent with the currently tested model.

It may happen that one type of data, such as the focal mechanisms in our application, does not constrain all the parameters of the stress model. An approximate partial model is considered sufficient to make a reasonable estimation of the corresponding weighting factor. For example, the stress model has been reduced to seven parameters for the evaluation of the weighting factor associated with the focal mechanisms, as is discussed later.

Inversion procedure. A genetic algorithm (GA) is used first for estimating Φ_h^{min}, Φ_f^{min}, N_c^{max} and M_c^{max}, then for searching the optimal model corresponding to Φ_s^{min}. The classic Monte Carlo (MC) technique is applied to find a random sample of models for establishing the corresponding 95% confidence level according to the ℓ_1-norm criterion. GA is a very efficient optimization technique which has been recently introduced in geophysical inverse problems as a guided MC (e.g., Gallagher et al., 1991). However, the classic MC method has been chosen for error analysis because, to our knowledge, the practical use of GA for this purpose has not yet been published. Some essentials of GA are recalled here for presenting the particular adaptation used in this paper. After discretizing the parameters, a population of Q models are generated at random and coded in Q binary strings. GA optimizes the models by strings manipulation through a 3-step iteration (or generation): reproduction, cross-over and mutation. (1) The reproduction step selects the models from those of the previous iteration via a misfit dependent probability Pr(i), chosen as a linear form: $Pr(i) = [\Phi_s^{max} - \Phi_s(i)]/[Q(\Phi_s^{max} - \Phi_s^{avg})] (i = 1,...,Q)$, where Φ_s^{max} and Φ_s^{avg} are respectively the maximum and the mean value of $\Phi_s(i)$. This choice of Pr has a wide distribution; thus it avoids favoring excessively the better models. Yet, the best model is forced to be selected at least once. (2) The cross-over step creates new models by transposing one of two string segments (cut at a randomly chosen position) between randomly paired models with a probability Pc. Large Pc values are chosen (Pc>0.8) for speeding up exploitation of the model information contained in the initial population. (3) The mutation step perturbs the string bits with a small probability Pm (Pm < 1/10000, as proposed by Holland, 1992). This step is designed for introducing some diversity into the model population. Pm is kept small in order to avoid a degeneracy of GA into a conventional MC.

Results from Le Mayet de Montagne

The complete data involve 31 HTPF measurements within the 50-780 m depth interval and 87 focal mechanisms within the 300-950m depth interval. Seven HTPF data in the upper 200m and another two near 780m are not taken into account because of the absence of seismic data at the shallowest depth range on one hand and, on the other hand, the existence of a greatly altered zone around 780m well documented by various borehole logs (Scotti and Cornet, 1994). Thus only 22 HTPF data are involved in the joint determination. In contrast, all the focal mechanisms are considered because no a priori information is available for examining their consistency with the global stress field.

Searching the optimal model with GA. The discretization interval for the angular parameters is 2° or 3° (covering the full range of 180°), that for stress magnitudes is 0.2 MPa in a range of 13 MPa and that for stress gradients is 0.0003 MPa/m in a range of 0.02 MPa/m. All ranges are centered around the corresponding values of previous regional stress field determination (Cornet and Burlet, 1992). The specific weight of overburden (α_3) is fixed at 0.0265 MPa/m. This leaves nine parameters to be determined. Our GA implementation uses a 6 bits coding for each parameter so tha each parameter may take 63 possible values. Each model o nine parameters forms a string of 54 bits.

The GA is first applied only to the HTPF data. Fig.1(a shows the mean and the minimum misfit evolution for three different model populations. For each of them, the minimum misfit is obtained as early as the 200th iteration although the mean value for larger populations may decrease mor slowly. The corresponding stress model is found to be th same as that obtained by a least squares method (Corne and Valette, 1984) for the two larger populations.

In the case of focal mechanisms, there is no information constraining the absolute stress magnitudes, so the GA i applied by fixing the vertical stress magnitude (not necessarily being a principal stress) and another eigenvalue, i.e only seven parameters are searched. Fig.1(b) shows a performance of GA similar to that observed for the HTPF data

These two analyses yield: Φ_h^{min}=13.0, N_c^{max}=22

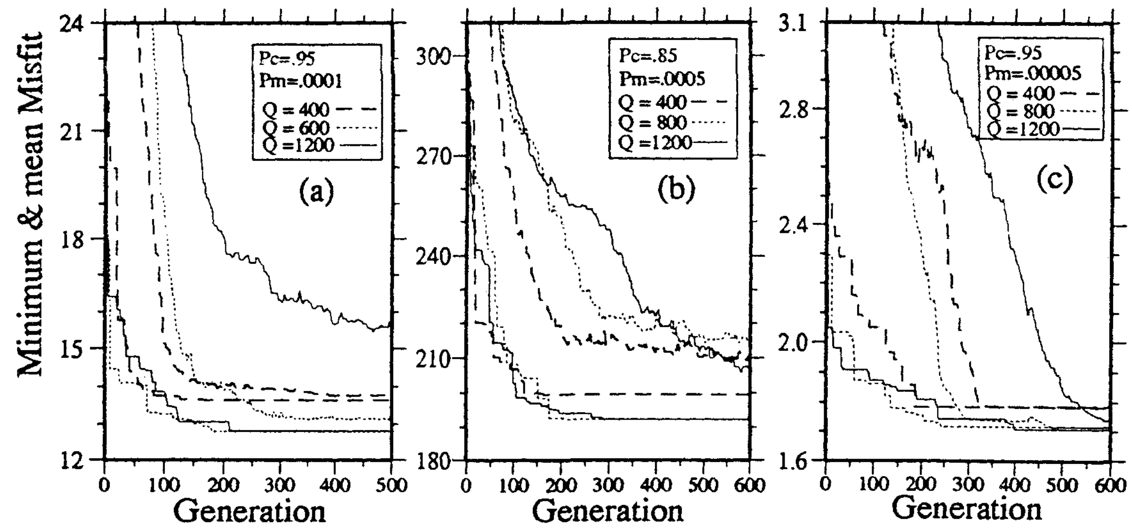

Figure 1 : Performance evolution and comparison of GA used in the various inversions: (a) HTPF data alone, (b) focal mechanisms alone and (c) joint inversion. In each inversion, GA was run with three different population size Q, with the crossover probability Pc and mutation probability Pm. Each run is displayed by two curves in the same style, the upper one represents the average misfit while the lower one represents the minimum misfit.

Φ_s^{min}=192.0 and M_c^{max}=72. The joint inversion by GA brings again a performance similar to the two previous ones as illustrated by Fig.1(c). The optimal model is chosen as that for which the minimum misfit has been found (Φ_s^{min} =1.71): $S_1 = 20$, $S_2 = 19.4$, $S_3 = 11.8$MPa, $\lambda_1 = -34^0$, $\lambda_2 = 86^0$, $\lambda_3 = 88^0$ ($z_0 = 750$m, λ_1 and λ_2 are respectively the strike and dip of S_1 axis, λ_3 is the angle between S_2 axis and the horizontal line in the plane perpendicular to S_1); $\alpha_1 = .0258$, $\alpha_2 = .0146$, $\alpha_3 = .0265$MPa/m, $\eta = 162^0$ (azimuth of α_1). This model fits 21 HTPF data and 63 focal mechanisms (Nc=21 and Mc=63 in eq.(3)).

Note that for all three cases, the minimum population size which allows identification of the optimal model lies around 600~800.

Model space exploration by MC. 30 million models generated at random, within a regular grid twice as coarse as that used for the GA, have been tested. 430 models for which the misfit Φ_s is less than the 95% confidence limit $\Phi_s^{95\%}$ (=2.13) are retained. They are used to establish the 95% confidence level of the optimal stress model obtained from GA (Fig.2a). They are quite concentrated around the optimal solution. These models explain in average 95% of the HTPF data and 70% of the focal mechanisms. For the other 30% of the focal mechanisms, the mean rotation angle exceeds either 18° or three times the corresponding standard deviation (eq.2) for more than 50% of these 430 models.

During this exploration we have also retained some 60000 models fitting only the HTPF data by the same confidence limit criterion. A sample of 3000 of them is used to draw the 95% confidence level of the optimal HTPF solution (Fig.2b).

A comparison between Fig.2a and Fig.2b brings the fol-

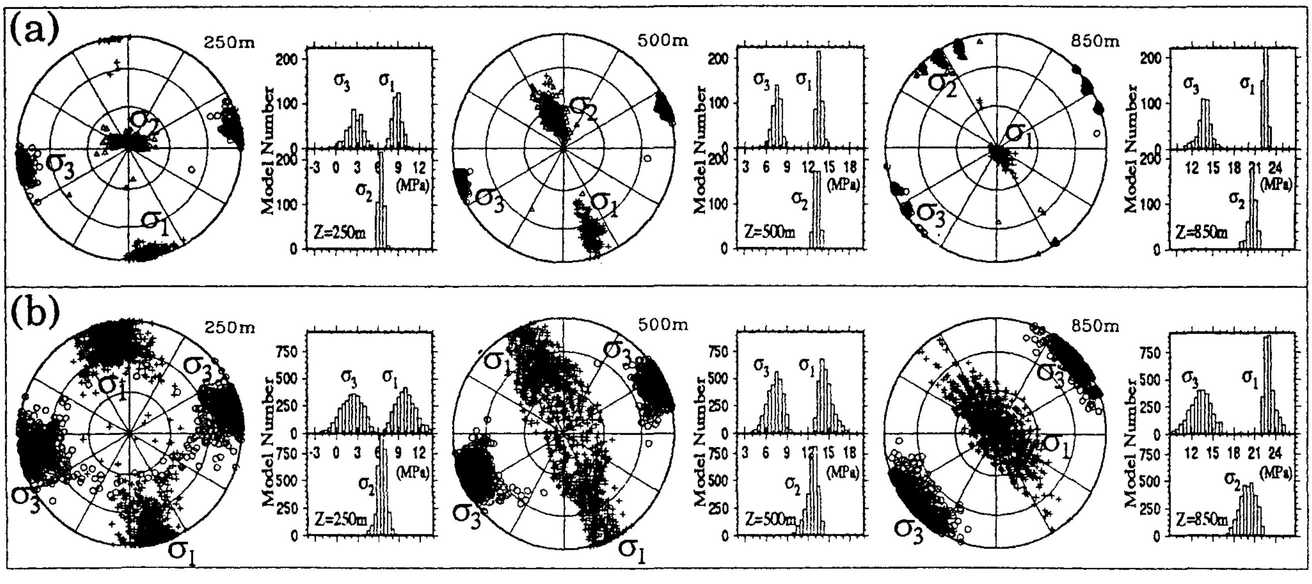

Figure 2 : (a) Lower hemisphere equal area projection of principal stress axes and Histogram of principal stress magnitudes, for various depths, for the joint inversion. (b) Results obtained by inversion of the sole HTPF data. Same notations as for (a), but the σ_2 axes are not shown.

lowing observations: The model space is fully explored as shown in Fig.2a, so the retained models of joint inversion are representative of all the possible solutions, and the confidence zonation is significant. The joint results are similar in magnitudes as well as in principal orientation to those obtained with the sole HTPF data, but their certainty increases clearly. The major horizontal stress direction of the joint results shows a clockwise rotation of 5 to 10° in comparison with the HTPF results. Such a difference has the same tendency as already mentioned for the results obtained by inversion of the focal mechanisms taken alone and with a uniform stress model of four parameters. However, the difference with respect to this former solution is larger than 30° (see Table 1). This implies that the seismic data have effectively contributed to the joint result but their role is not as important as that of the HTPF data. However, it has been statistically verified that the weight of the focal mechanisms is slightly greater than that of HTPF data (the mean ratio of the second term over the first one in eq.(3) is equal to about 1.16). This paradox can be explained by the fact that the seismic data are less consistent than the HTPF data in term of the regional stress field. The earthquakes are located in or near the hydraulically conductive fractured zones which often coincide with altered zones, while the borehole intervals of the HTPF tests were intentionally selected in intact rock. This proposition is supported by the observation that the inversion of various sets of HTPF data has consistently led to similar results while the four parameter inversion of focal mechanisms observed during the initial injection tests yields results significantly different from those derived from the focal mechanisms observed during the large scale injections.

It can be concluded that the discrepancy between the results obtained by previous separate inversions disappears in the joint inversion. However, some focal mechanisms remain inconsistent with the joint results (up to 30% of the whole). This implies first, that when only focal mechanisms are used for the stress determination, those which are inconsistent with the regional stress field influence significantly the output of the inversion. Thus for the scale of these events (slip zones of the order of 1 m^2), the regional stress field cannot be determined by the sole inversion of focal mechanisms of induced microseismicity. Further, the joint inversion provides means to identify those focal mechanisms which are heterogeneous with the regional stress field and this may reveal powerful for identifying the main zones of alteration.

Table 1. Azimuth of the maximum horizontal stress

Results type	Z=450-550m	Z=750-900m
HTPF (1)	NE 155±20°	NE 140 ± 23°
Focal mech.(2)	NE 30±20°	NE 170 ± 18°
Joint method	NE 160± 8°	NE 146 ± 15°

(1) Same for Cornet et al.(1992) and the present study.
(2) From Cornet et al. (1992).

Conclusion

A joint inversion method has been proposed for integrating two or more kinds of data gathered in the same rock mass for the sake of determining the regional stress field. It includes an optimal model search using a genetic algorithm and the error analysis by the classic Monte Carlo technique. Successful application of this method to HTPF measurements and focal mechanisms of induced seismicity illustrates the improvement that the joint inversion technique brings as compared to the results obtained with the separate determinations.

The results of the joint inversion has demonstrated that the concept of the regional stress field is valid for large volumes of rock (about 1 km^3). It also outlines the existence of focal mechanisms which are not consistent with the regional stress field. These inconsistent focal mechanisms should reveal helpful for identifying zones of stress heterogeneities.

Acknowledgements. This work was funded by Centre National de la Recherche Scientifique (PIRSEM) and by the European Economic Communities (DG XII). The help of B. Bert, L. Martel and G. Rozières for the data acquisition process is greatfully acknowledged.

References

Barton C.A., M.D. Zoback and K.L. Burns, In situ stress orientation and magnitude at the Fenton Hill geothermal site, New Mexico, determined from wellbore breakouts, *Geophys. Res. Lett.*, 15, No.5, 467-470, 1988.

Cornet F.H. and Burlet D., Stress field determinations in France by hydraulic tests in boreholes. *J. Geophys. Res.*, 97, B8, 11,829-11,849, 1992.

Cornet F.H. and Julien Ph., Stress determination from hydraulic tests data and focal mechanisms of induced seismicity.*Intern. J. Rock Mech. Min. Sci. & Geomech. Abs.*, 26, 235-248, 1989.

Cornet F.H. and B. Valette, In-situ stress determinations from hydraulic injection test data. *J. Geophys. Res.*, 89, B13, 11,527-11,537, 1984.

Cornet F.H., J.M. Yin and L. Martel, Stress heterogeneity and flow path in a granite rock mass, in *Fractured and jointed rock masses* (L. Myer ed.), vol.1, 80-87, Lawrence Berkeley Laboratory report LBL - 32379, 1992.

Gallagher K., M. Sambridge and G. Drijkoningen, Genetic Algorithms: an evolution on Monte Carlo methods in strongly non-linear geophysical optimization problems, *Geophys. Res. Lett.*, 18, No.12, 2177-2180, 1991.

Gephart J.W. and D.W. Forsyth, An improved method for determining the regional stress tensor using earthquake focal mechanism data: application to the San Fernando earthquake sequence. *J. Geophys. Res.*, 89, 9305-9320, 1984.

Haimson B.C., L.W. Tunbridge, M.Y. Lee and C.M. Cooling, Measurement of rock stress using the hydraulic fracturing method in Cornwall, U.K.—Part II. Data reduction and stress Calculation, *Int. J. Rock Mech. Min. Sci.* 26, 6, 361-372, 1989.

Holland J.H. Genetic algorithms. *Scientific American*, July 1992, 44-50, 1992.

Julien Ph. and F.H. Cornet, Stress determination from aftershocks of the Campania-Lucania earthquake of November 23, 1980. *Ann. Geophys.*, 5, No.3, 289-300, 1987.

Scotti O. and F.H. Cornet, In situ evidence for fluid induced aseismic slip event along fault zones, *Int. J. Rock Mech. Min. Sci.* 31, 347-358, 1994.

Tarantola A, Inverse problem theory: Methods for data fitting and model parameter estimation, Elsevier, 1987.

Yin J.M., Détermination du champ de contrainte regional à partir des tests hydrauliques et des mécanismes au foyer de microséismes induits, Ph.D. thesis of Université Paris 7, 1994.

F.C. Cornet and J.M. Yin, Sismologie, Institut de Physique du Globe de Paris, 4 Place Jussieu, 75252 Paris, France.

(Received April 27, 1994; revised August 29, 1994;
accepted September 13, 1994.)

PAGEOPH, Vol. 145, Nos. 3/4 (1995)

0033-4553/95/040677-24$1.50 + 0.20/0

Analysis of Induced Seismicity for Stress Field Determination and Pore Pressure Mapping

F. H. CORNET[1] and YIN JIANMIN[1]

Abstract—The focal mechanisms of some one hundred microseismic events induced by various water injections have been determined. Within the same depth interval, numerous stress measurements have been conducted with the HTPF method. When inverted simultaneously, the HTPF data and the focal plane solutions help determine the complete stress field in a fairly large volume of rock (about 15×10^6 m^3). These results demonstrate that hydraulically conductive fault zones are associated with local stress heterogeneities. Some of these stress heterogeneities correspond to local stress concentrations with principal stress magnitudes much larger than those of the regional stress field. They preclude the determination of the regional stress field from the sole inversion of focal mechanisms. In addition to determining the regional stress field, the integrated inversion of focal mechanisms and HTPF data help identify the fault plane for each of the focal mechanisms. These slip motions have been demonstrated to be consistent with Terzaghi's effective stress principle and a Coulomb friction law with a friction coefficient ranging from 0.65 to 0.9. This has been used for mapping the pore pressure in the rock mass. This mapping shows that induced seismicity does not outline zones of high flow rate but only zones of high pore pressure. For one fault zone where no significant flow has been observed, the local pore pressure has been found to be larger than the regional minimum principal stress but no hydraulic fracturing has been detected there.

Key words: Induced seismicity, stress determination, stress heterogeneity, fluid flow, fault morphology.

1. Introduction

The injection of water in a fractured rock mass generates some seismicity when the injection pressure becomes large enough (e.g., PEARSON, 1981; NIITSUMA *et al.*, 1982; CORNET *et al.*, 1982; PINE and BATCHELOR, 1984; TALEBI and CORNET, 1987; HOUSE, 1987; FEHLER, 1989). In most cases this microseismicity is caused by shear events generated by the decrease in effective normal stress, supported by pre-existing fracture surfaces. This decrease in effective normal stress is caused by the increase in interstitial pressure induced by water injection.

In this paper, attention focuses on an analysis of focal plane solutions of microseismic events induced by various water injections in a granite rock mass. This

---

[1] Département de Sismologie, Institut de Physique du Globe de Paris, 4 place Jussieu, 75252 Paris cedex 05, France.

analysis concerns first the possibility of using focal mechanisms for determining the regional stress field. Results obtained with a stress determination method, which integrates hydraulic test data and focal plane solutions, are discussed.

This regional stress field determination, combined with the identification of the proper fault plane for each of the consistent focal mechanisms, helps constrain the friction coefficient and the effective stress law which control the stability of this rock mass. These values provide means to map the fluid pressure away from the injection well within two fault structures which exhibit different hydraulic connection patterns.

2. *Injection Tests at Le Mayet de Montagne*

The granite test site at Le Mayet de Montagne, located in central France some 25 km to the southeast of Vichy, has been developed for conducting large-scale *in situ* experiments on forced water circulation (CORNET, 1989). The first deep borehole, INAG III-8, reaches 780 m, while the second one, INAG III-9, is 840 m deep and located 100 m away. Preliminary injection tests were run in these wells at flow rates equal to 8.6 l/s in order to identify the main flowing zones in the lowest 250 m from the bottom of the wells. In INAG III-9 only four significant flowing zones have been identified. The upper one occurs around 650 m.

During the early stage of the reservoir development, a small-scale circulation test was conducted between the two boreholes. Water was injected through the 250 m open hole section at the bottom of INAG III-9, with a 8.3 l/s injection flow rate and a 8.2 MPa well head pressure, for about 70 hours. At the end of this circulation test, the production well (INAG III-8) was shut off while injection proceeded for another 3 hours at 22.2 l/s (12 MPa well head pressure).

During this preliminary reservoir development, the induced seismicity was monitored with a network of fifteen 3D seismic stations. P- and S-wave velocities were determined by detonating small charges of dynamite at various depths in the two deep wells as well as in some superficial ones so as to cover various azimuths and the entire depth range in which events were expected. These blasts were also favorably utilized to determine the orientation of the horizontal components of the seismic stations. The velocity field identified in this manner has been found to be fairly anisotropic and this anisotropy has been taken into account in locating events (TALEBI and CORNET, 1987). About 100 events were recorded during the small-scale circulation experiment, from which 31 well-defined focal mechanisms could be computed (CORNET and JULIEN, 1989; see also Table 1).

The large-scale reservoir development involved three phases during which the induced microseismicity was continuously monitored by the previously mentioned network. During the first phase, injection proceeded through INAG III-8 between the bottom of the well and an inflatable packer set at 713 m. Two inflatable packers

Table 1

Location and focal plane solutions for the microseismic events observed during the initial reservoir development. Events 100, 101 and 102 were observed during initial stimulations in the well INAG III-8 while all the others correspond to injections in the well INAG III-9. Origin of coordinates is on the INAG III-8 well head. For the nodal planes, d is azimuth and p is dip while i is rake. δ and ε refer to standard deviations of the parameter shown as index

				First nodal plane						Second nodal plane					
No.	*X* (east)	*Y* (north)	*Z* (downward)	(*d*1,	*p*1,	*i*1)	(δ*d*1,	δ*p*1,	δ*i*1)	(*d*2,	*p*2,	*i*2)	(δ*d*2,	δ*p*2,	δi2)
1	87 ± 7	−56 ± 4	850 ± 13	266	66	48	30	7	20	150	48	146	20	3	15
2	68 ± 8	−96 ± 8	640 ± 8	342	78	223	12	4	7	240	48	343	12	5	8
7	92 ± 7	−108 ± 1	664 ± 10	96	32	226	7	5	6	326	67	294	7	4	6
8	88 ± 7	−101 ± 5	655 ± 8	356	58	237	10	5	10	226	45	310	10	6	12
12	71 ± 8	−56 ± 10	656 ± 8	183	71	199	10	2	5	87	72	340	14	4	3
14	95 ± 5	−37 ± 2	532 ± 2	120	84	36	5	2	5	25	55	173	1	5	3
15	55 ± 2	−78 ± 3	770 ± 13	172	80	230	4	2	3	70	40	345	4	2	2
21	63 ± 15	−58 ± 4	830 ± 15	339	58	21	11	4	4	237	72	146	11	3	5
23	75 ± 8	−42 ± 2	823 ± 13	354	79	205	2	1	6	258	65	347	2	6	1
24	55 ± 3	−142 ± 3	478 ± 6	209	88	238	15	4	6	115	32	356	15	4	6
26	95 ± 2	−107 ± 2	668 ± 9	194	84	40	3	2	5	99	50	172	4	5	2
27	67 ± 3	−50 ± 2	831 ± 13	180	89	224	2	2	2	90	46	359	2	2	2
29	87 ± 6	−122 ± 6	660 ± 15	78	65	188	1	5	2	346	82	335	3	1	5
31	75 ± 3	−40 ± 4	800 ± 6	182	70	203	1	4	2	85	68	339	2	2	4
32	98 ± 3	−108 ± 5	770 ± 15	160	75	221	6	2	6	56	45	339	6	3	3
33	92 ± 3	−64 ± 3	763 ± 12	142	86	220	8	2	3	48	50	355	9	2	3
34	50 ± 0	−100 ± 5	950 ± 10	22	81	181	1	1	1	291	89	352	1	1	1
38	75 ± 2	−62 ± 8	798 ± 5	140	85	220	9	2	2	46	50	354	11	2	2
43	52 ± 3	1 ± 3	520 ± 12	248	42	56	10	9	27	108	56	116	20	7	25
45	86 ± 2	−109 ± 4	653 ± 4	242	88	54	10	2	3	150	36	177	13	2	5
49	66 ± 4	11 ± 5	486 ± 10	296	74	24	3	2	3	199	68	163	1	3	2
51	61 ± 3	12 ± 4	509 ± 9	243	48	18	5	13	3	142	76	136	5	2	7
52	61 ± 1	−49 ± 2	449 ± 5	72	79	38	2	2	2	334	54	167	2	2	2
55	73 ± 3	−66 ± 3	816 ± 11	170	84	225	5	2	2	74	46	350	7	2	2
58	61 ± 2	25 ± 3	482 ± 11	256	46	35	5	7	10	140	66	131	5	5	8

Continued overleaf

Table 1 (*Contd.*)

				First nodal plane						Second nodal plane					
No.	X (east)	Y (north)	Z (downward)	($d1$,	$p1$,	$i1$)	($\delta d1$,	$\delta p1$,	$\delta i1$)	($d2$,	$p2$,	$i2$)	($\delta d2$,	$\delta p2$,	$\delta i2$)
59	55 ± 2	-29 ± 3	825 ± 10	160	80	223	8	4	2	60	48	346	8	4	5
61	87 ± 1	-5 ± 8	555 ± 17	50	50	185	1	1	3	317	88	320	5	4	1
62	101 ± 3	-12 ± 14	770 ± 30	324	77	211	13	4	4	224	60	344	3	4	4
66	83 ± 1	-84 ± 2	521 ± 6	324	80	231	14	4	5	221	40	344	14	5	5
69	80 ± 2	-69 ± 3	477 ± 5	340	72	261	6	2	2	185	20	293	21	10	20
70	74 ± 3	-2 ± 4	512 ± 6	230	50	12	5	4	2	132	80	140	3	3	5
71	71 ± 3	-50 ± 3	827 ± 3	168	81	221	5	2	4	70	50	349	6	3	3
100				305	69	61				195	48	140			
101				325	68	8				233	85	149			
102				330	68	15				236	80	149			

were also placed in INAG III-8 in order to limit as much as possible short circuits caused by the well. Injection proceeded for 210 hours at a flow rate equal to 8.3 l/s with a well head pressure which varied from 7.5 MPa at the beginning of the test to 9.1 MPa (stabilized value at the end of the test). Only two microseismic events were observed during this phase. Thereafter the injection flow rate was increased to 16.7 l/s with a well head pressure reaching 10.8 MPa (total injected volume of 11 665 m^3). During this phase eleven microseismic events were monitored, ten of which yielded clear fault plane solutions (Table 2).

During the second phase, injection proceeded through the 250 m long open hole section at the bottom of INAG III-9 at a flow rate equal to 8.3 l/s with a well head pressure equal to about 9.2 MPa. A stationary condition was reached after one week of injection. This stationary condition was maintained for about 21 days so that the total injected volume for this phase reached 14 790 m^3. During this phase, 50 microseismic events were recorded from which 23 yielded well-defined focal mechanisms (Table 2).

The third phase (injection between 600 m and 840 m in INAG III-9) involved a first period designed for characterizing the hydraulic properties of the system while the second period was run for testing long duration stationary circulation conditions. During the first period the system was tested for various flow rates. Each flow rate was maintained constant for periods ranging from 5 to 3 days. The maximum flow rate reached 21.1 l/s with a well head pressure equal to 12.5 MPa after three days of pumping, then the flow rate was decreased to 16.6 l/s. During this third period 46 microseismic events were recorded from which 19 yielded a well-defined focal mechanism (Table 2). No event was recorded during the pumping tests at flow rates smaller than, or equal to, 8.3 l/s (well head pressures smaller than 9.3 MPa). All events occurred during the initial period of this phase except for one event which occurred just before the end of pumping, when the flow rate had been increased to 12.5 l/s (well head pressure equal to 10.2 MPa) and another one occurred when pumping had stopped. The total injected volume during the first period of this phase reached 16 310 m^3.

Thus, while the seismic activity monitored during the early reservoir development (about one hundred events) corresponds to a total injected volume of about 2200 m^3, the various seismically active phases (11 events, 50 events, 46 events) associated with the large-scale injection tests correspond to injected volumes ranging from 11 665 m^3 to 16 310 m^3. The location of all events recorded while injection was proceeding through the well INAG III-9 are shown on Figure 1.

The duration of most events ranges between 0.3 and 0.5 seconds, with the largest ones reaching 0.6 s. The *P*-wave corner frequencies vary between 200 and 400 Hz while the seismic moments vary between 10^7 and 10^8 Nm. Accordingly, the magnitudes of these events range between -2 and -1.

Three main active zones can be identified in Figure 1: a deeper zone, in which no clear structure has been identified, and two subplanar structures. CORNET and

Table 2

Location and focal plane solutions for the microseismic events observed during the large-scale injection tests. Coordinate system is centered on the well head of INAG III-8. For the nodal planes d is azimuth and p is dip, i is rake; ε and δ refer to the standard deviation of the parameter shown as index

				First nodal plane						Second nodal plane					
No.	X(east)	Y(north)	Z(down)	($d1$,	$p1$	$i1$)	($\delta d1$,	$\delta d1$,	$\delta d1$)	($d2$,	$p2$,	$i2$)	($\delta 2$,	$\delta p2$,	$\delta i2$)
2	21 ± 7	51 ± 16	803 ± 3	28	75	196	5	4	3	294	75	345	5	2	4
3	22 ± 6	50 ± 5	757 ± 15	121	70	184	6	2	3	30	86	340	7	3	2
4	22 ± 1	−124 ± 7	557 ± 10	326	80	227	5	2	6	225	44	345	8	5	4
5	22 ± 3	−118 ± 4	553 ± 2	49	85	2	5	3	3	319	88	175	5	3	3
6	23 ± 2	−248 ± 3	428 ± 6	34	70	11	4	3	10	300	80	160	6	9	3
7	166 ± 8	78 ± 2	849 ± 7	28	77	206	6	5	4	292	65	346	8	3	5
8	91 ± 14	−14 ± 4	505 ± 8	324	80	190	3	3	3	232	80	350	4	2	3
9	5 ± 6	−254 ± 2	385 ± 8	53	80	20	5	2	6	319	70	169	6	6	3
10	46 ± 3	1 ± 2	464 ± 12	356	70	190	5	5	2	262	80	340	3	1	5
11	32 ± 4	−109 ± 5	562 ± 25	76	82	16	3	2	2	344	74	172	5	2	3
13	26 ± 4	−131 ± 3	601 ± 3	344	88	212	3	2	7	253	58	358	5	7	2
15	70 ± 3	−45 ± 1	494 ± 7	332	85	202	4	2	3	240	68	355	5	3	3
16	83 ± 4	−67 ± 9	439 ± 12	350	88	18	2	2	2	259	72	178	4	2	2
17	100 ± 5	−51 ± 3	523 ± 3	22	70	219	4	2	9	277	54	335	10	7	6
19	14 ± 15	−68 ± 5	858 ± 13	296	70	191	3	5	2	202	80	336	4	1	5
20	69 ± 2	−42 ± 4	498 ± 14	348	78	201	6	2	3	254	70	347	8	3	3
21	100 ± 10	−100 ± 2	798 ± 2	284	72	186	4	4	2	192	84	342	3	2	5
23	73 ± 6	−74 ± 4	416 ± 1	83	78	14	7	2	2	350	76	168	6	2	2
24	99 ± 10	−56 ± 9	813 ± 7	141	86	206	4	2	3	49	64	356	3	3	2
26	96 ± 6	5 ± 10	500 ± 18	254	50	27	6	4	5	146	70	137	10	2	4
29	129 ± 5	−61 ± 8	563 ± 22	26	70	32	4	2	6	284	60	157	7	5	3
31	93 ± 2	−89 ± 4	839 ± 6	140	85	205	3	2	5	48	65	355	4	5	2
34	103 ± 9	−65 ± 3	566 ± 12	311	88	207	7	2	2	220	63	358	8	2	3
35	106 ± 7	−53 ± 5	567 ± 8	320	75	196	3	2	3	226	75	345	5	2	3
36	114 ± 11	−93 ± 6	795 ± 7	286	79	185	3	5	2	195	85	349	4	2	5
38	114 ± 2	−47 ± 5	554 ± 7	80	82	36	5	2	5	344	55	170	8	4	3
40	122 ± 1	−167 ± 7	621 ± 10	29	68	11	4	1	10	295	80	158	7	9	2

41	84 ± 2	−15 ± 1	566 ± 5	250	90	330	4	2	6	340	60	180	4	6	3
42	45 ± 5	−90 ± 3	804 ± 9	360	90	348	2	2	4	90	78	180	3	4	2
46	75 ± 1	10 ± 2	492 ± 6	342	86	198	3	1	3	251	72	355	5	3	2
48	119 ± 14	−74 ± 12	913 ± 16	165	75	202	7	4	4	69	69	344	6	2	4
51	78 ± 14	20 ± 8	294 ± 12	82	43	62	5	2	10	298	53	114	11	2	10
56	55 ± 5	−29 ± 4	847 ± 9	168	82	217	3	2	3	72	53	350	5	3	3
64	93 ± 8	−19 ± 7	530 ± 3	345	84	188	5	2	3	254	82	354	6	3	2
65	72 ± 3	8 ± 4	501 ± 23	268	76	24	3	2	5	172	67	165	5	4	3
67	76 ± 3	−19 ± 2	806 ± 10	296	68	185	4	5	1	204	85	338	6	1	5
71	93 ± 6	−75 ± 4	548 ± 6	356	78	201	6	1	7	262	70	347	7	6	2
76	84 ± 2	−17 ± 2	485 ± 8	336	80	200	4	2	3	242	70	349	7	3	2
78	104 ± 12	−56 ± 3	568 ± 9	332	84	212	5	2	5	238	58	353	7	5	4
80	105 ± 9	−57 ± 2	831 ± 4	314	80	210	6	3	4	218	60	348	8	4	4
83	77 ± 4	−12 ± 2	483 ± 8	334	86	202	3	2	3	242	68	356	4	3	3
88	123 ± 8	−83 ± 2	369 ± 15	133	90	57	5	4	3	43	33	180	5	3	7
90	97 ± 2	−59 ± 11	568 ± 10	336	85	194	7	2	3	245	76	355	8	2	3
92	30 ± 2	−77 ± 4	401 ± 4	33	64	205	5	2	7	292	68	332	9	6	4
93	96 ± 8	−53 ± 1	564 ± 2	121	75	182	5	2	3	31	88	345	5	2	2
94	82 ± 3	−32 ± 5	939 ± 6	264	75	180	5	5	1	174	90	345	5	1	5
95	129 ± 6	−100 ± 4	801 ± 4	18	64	202	8	4	7	278	70	332	8	5	5
96	81 ± 5	−64 ± 3	853 ± 25	290	75	188	5	5	3	198	82	344	5	2	5
97	103 ± 9	4 ± 4	870 ± 3	304	84	204	4	1	5	211	66	353	5	5	2
98	98 ± 3	−72 ± 7	528 ± 8	236	42	8	7	5	6	140	85	132	6	2	5
102	101 ± 5	−62 ± 4	558 ± 9	298	86	201	4	2	3	207	69	356	5	3	3
105	103 ± 11	−64 ± 4	568 ± 7	298	85	202	4	1	3	206	68	355	5	3	2

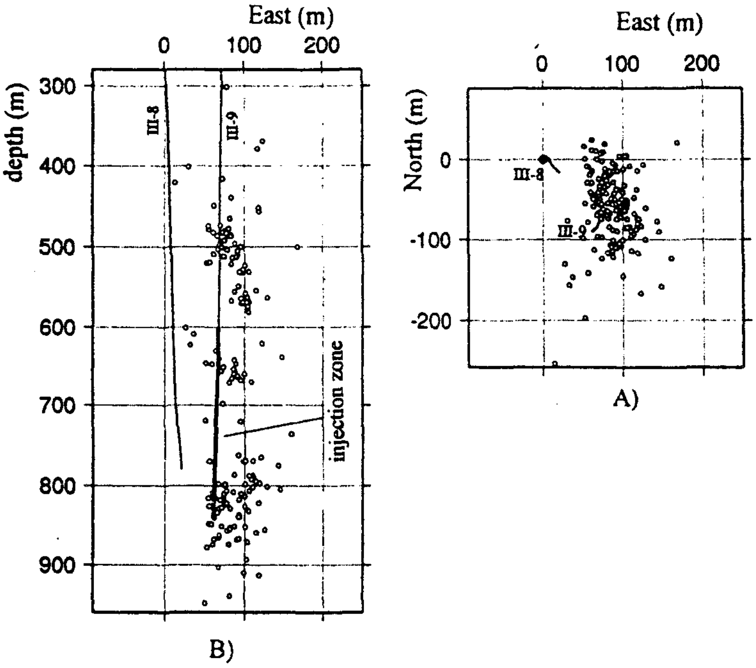

Figure 1
Location of all events recorded while injection was proceeding through the well INAG III-9. A) Projection on a horizontal plane, B) Projection on a vertical plane oriented in the east-west direction. Injection was conducted between 598 m and 840 m.

Scotti (1993) identified by a least-squares technique the best fitting planes passing through the upper and lower planar structures. The upper seismic zone fits with a plane oriented N 04°E and dipping 61° to the east. It intersects the well INAG III-9 in the 481–521 m depth range. The lower planar structure has been fitted with a plane oriented N 174°E and dipping 36° to the east. It intersects the well INAG III-9 in the depth range 630–654 m. Within both these depth intervals sonic logs outline zones of alterations, confirmed by the analysis of the cuttings produced during drilling operations.

Interestingly, none of these orientations could be identified from a statistical analysis of the fractures identified by borehole imaging within these depth intervals. Yet it is one of the dominant fault orientations mapped on site. This demonstrates that the small-scale morphology of a fractured (fault) zone does not always reflect its large-scale geometry and that fault zones may involve small-scale fractures of very diverse orientations. Also, while both zones are clearly visible on the geophysical logs and in the cuttings, only those around 650 m exhibit a significant hydraulic conductivity: The zone intersected around 500 m does not appear on the initial flow logs and therefore is not connected to the large-scale hydraulically significant fracture network (CORNET and SCOTTI, 1993).

3. Determination of the Regional Stress Field

The regional stress field has been determined by three different methods: The Hydraulic Tests on Pre-existing Fractures (HTPF) method, the inversion of focal mechanisms of induced seismicity, the simultaneous inversion of HTPF data and focal plane solutions. These results have already been published (CORNET and JULIEN, 1989; CORNET *et al.*, 1992; YIN and CORNET, 1994). They are briefly recalled here for later discussions.

3.1 The HTPF Stress Determination

The HTPF method consists of conducting hydraulic tests on pre-existing fractures of known orientation (characterized by the normal **n** to the fracture plane) for determining the normal stress σ_n supported by the fracture plane. The problem is to determine the six components of the stress σ such that $\sigma \mathbf{n} \cdot \mathbf{n} = \sigma_n$. The regional stress field σ is presumed to vary linearly with the spatial coordinates (x_1, x_2, x_3; x_1 horizontal, positive to the north, x_2 horizontal, positive to the east, x_3 vertical, positive downward):

$$\sigma = \mathrm{S} + x_1\alpha^1 + x_2\alpha^2 + x_3\alpha^3 \tag{1}$$

where S, α^1, α^2, α^3 are symmetrical tensors. α^1, α^2, α^3 are the stress gradients respectively in the x_1, x_2, x_3 directions. Equilibrium conditions show that, in the absence of topography or lateral heterogeneities ($\alpha^1 = \alpha^2 = 0$), one of the principal directions of α^3 is vertical (CORNET, 1992). This result is very similar to that proposed by MCGARR (1980) except that, here, no assumption is made regarding the constitutive equation of the rock mass. It is only assumed that, within the domain of interest, the stress field varies fairly smoothly around some central point so that its components can be approximated by linear functions. From now on the tensor α^3 will be simply denoted by α. The stress determination consists of determining S and α derived from N HTPF data. A HTPF datum includes both the normal stress measurement and the fracture orientation determination.

At Le Mayet de Montagne, eighteen HTPF measurements have been conducted between 60 m and 730 m, prior to the water circulation experiments. For this stress determination the regional stress field and its first derivative are assumed continuous up to ground surface. The solution is defined by the principal values of S($S_1 = 5.1$ MPa, $S_2 = 0.2$ MPa; $S_3 = 0$; S_1 is horizontal and oriented N 24°E.) and α($\alpha_1 = 0.0226$ MPa/m; $\alpha_2 = 0.0084$ MPa/m; $\alpha_3 = 0.0264$ MPa/m; α_1 is oriented 104°

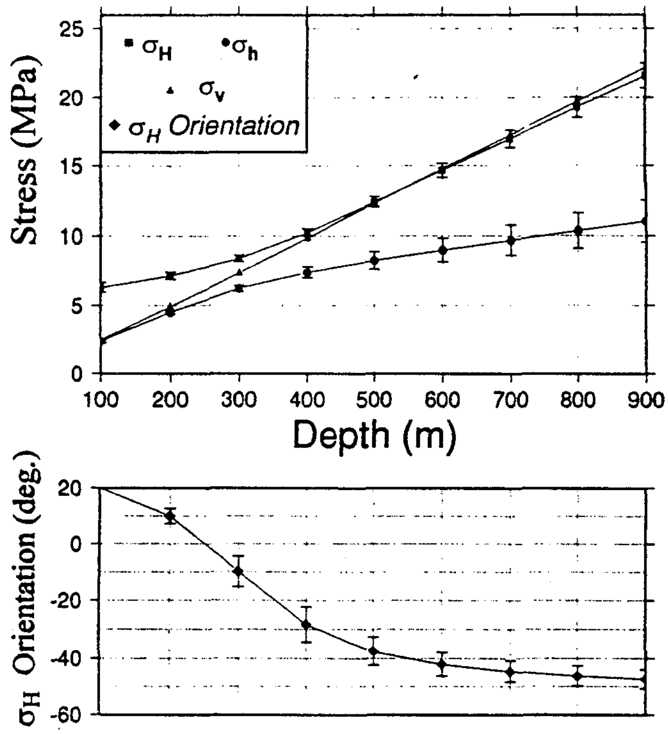

Figure 2
Stress profiles derived from the HTPF measurements conducted prior to the injection tests. σ_H orientation is measured from the north and positive eastward.

to the north of S_1). Values for the horizontal principal stress magnitudes σ_H and $\sigma_h(\sigma_H > \sigma_h)$ and for the orientation of σ_H with respect to north (positive eastward) are indicated for various depths in Figure 2.

Two and a half years after the main water circulation experiment was completed, another 13 HTPF measurements have been carried out in well INAG III-9. These measurements demonstrate that no permanent large-scale stress perturbation has been induced by the various water injections (CORNET 1992). It has been observed, however, that two of these HTPF measurements (at 780 m and 773 m) are heterogeneous with respect to the original regional stress field and that, according to a spinner log, these heterogeneous data are located close to one of the most hydraulically significant zones of the borehole.

3.2 Integration of Focal Solutions in the Stress Determination

A few authors (e.g., VASSEUR *et al.*, 1983; GEPHART and FORSYTH, 1984; JULIEN and CORNET, 1987; RIVEIRA and CISTERNAS, 1990) have proposed determining the regional stress field from an inversion of the focal plane solutions of seismic events. These determinations asssume that the stress field is uniform throughout the volume in which the seismic events occurred and that the slip vector is parallel to the resolved shear stress supported by the slipping planes (WALLACE, 1951; BOTT, 1959). Because only the direction of the shear component is constrained (and not its magnitude), these stress determinations yield only the principal stress directions (defined by the Euler angles ϕ, ψ and θ where ϕ and ψ are respectively the azimuth and dip of σ_1 and θ is the angle between the σ_2 direction and the horizontal plane) and a factor R characteristic of the ellipticity of the tensor: $R = (\sigma_2 - \sigma_1)/(\sigma_3 - \sigma_1)$; $(\sigma_1 > \sigma_2 > \sigma_3)$.

CORNET and JULIEN (1989) attempted a first stress determination with the focal mechanisms of the microseismic events observed during the preliminary reservoir development (injection of 2200 m^3). In order to satisfy the hypothesis of stress uniformity, they considered three different depth ranges: an upper one (above 550 m), an intermediate one (between 750 m and 550 m) and a lower one (below 750 m). For the two upper systems no satisfactory solution could be identified (too many inconsistent data). For the deeper system, 14 well-defined focal mechanisms were available for the inversion. Results establish that the maximum principal stress is vertical, but the maximum horizontal principal stress is oriented 70° to the east of the HTPF solution ($\varphi = 329°$, $\psi = 79°$, $\theta = 24°$, $R = 0.55$; Figure 3). This solution is consistent with 12 of the 14 mechanisms.

Another stress determination (YIN, 1994) has been undertaken with the complete set of focal mechanisms (seismicity induced by the large-scale injections combined with that of the early reservoir development). Here again the data has been separated into three different depth ranges in order to satisfy the stress homogeneity hypothesis. Although the resolution is not very good, results are far more satisfactory than Cornet and Julien's solution. For the deeper seismic system (Fig. 4), the solution yields $\varphi = 354°$, $\psi = 46°$, $\theta = 92°$, $R = 0.32$. For all depth

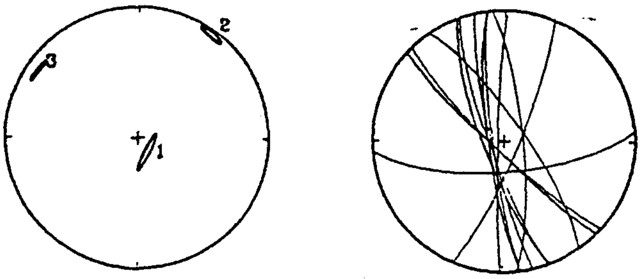

Figure 3
Stress determination derived from the inversion of focal mechanisms of the microseismic events observed during the preliminary reservoir development (total injected volume of 2200 m^3). Only the deepest seismic domain (see Fig. 1B) is considered. The stereographic projection of the principal directions is shown on the left. The orientation of selected planes is shown on the right.

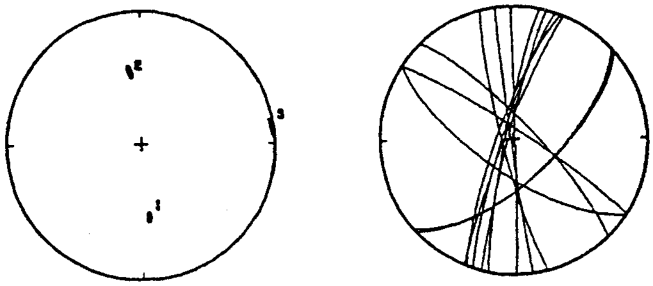

Figure 4
Same as Figure 3 but the seismic events considered are those induced by the large-scale reservoir development (injected volumes of 14 790 m^3 and 16 310 m^3).

ranges, a systematic 20 to 30 degrees discrepancy is observed for the maximum horizontal principal stress orientation, as determined on the one hand with this focal plane inversion and on the other hand with the HTPF method.

While the HTPF solution remains stable when new data are introduced, the focal plane solution varies, depending on the set of data considered for the inversion. As mentioned above, the post-circulation HTPF measurements outlined zones of local stress heterogeneity associated with some of the main flowing zones. Thus it has been concluded that some of the focal mechanisms are very likely "polluted" by local stress heterogeneities, and these, in turn, influence the stress determination.

However, the HTPF measurements involve only subvertical fractures, resulting in very poor resolution on the vertical stress component. Further, the HTPF stress determination assumes that the stress field is continuous up to the surface and that the vertical direction is principal at all depths. In order to alleviate these limitations and take advantage of those focal mechanisms which are not influenced by local stress heterogeneities, a joint inversion method integrating the HTPF data and the focal mechanisms has been developed (YIN and CORNET 1994). In this inversion scheme the stress field is represented by ten parameters. In equation (1), the tensor S represents the stress at a given depth; none of its six components (the three principal values S_1, S_2 and S_3 and the three Euler angles λ_1, λ_2 and λ_3) is assumed *a priori* to be null. The tensor α is the vertical stress gradient around this depth and lateral stress variations are presumed to be negligible within the domain of interest. Equilibrium conditions impose that α exhibits a vertical principal direction so that it is described by 4 parameters. The inversion scheme uses a genetic algorithm to identify the optimal solution and a Monte Carlo method to estimate the uncertainty of the determination.

This integrated stress determination has been conducted with all the focal mechanisms available for the site (including those found to be heterogeneous with HTPF stress determination) and with HTPF data obtained within the same depth interval as that of the focal mechanisms (all data obtained above 250 m have not been included). Further, the two deep HTPF measurements conducted close to a fracture zone which had been identified as being heterogeneous, have also been disregarded. This provides 87 focal mechanisms and 22 HTPF measurements.

Results of the joint inversion yields for S (defined at 750 m): $S_1 = 20$ MPa, $S_2 = 19.4$ MPa and $S_3 = 11.8$ MPa, $\lambda_1 = -34°$, $\lambda_2 = 86°$ and $\lambda_3 = 88°$. The principal values for the vertical gradient are $\alpha_1 = 0.0226$ MPa/m, $\alpha_2 = 0.0084$ MPa/m; $\alpha_3 = 0.0264$ MPa/m (in the vertical direction); the orientation of α_1 with respect to the north is $\eta = \text{N}162°\text{E}$.

The stress field and its uncertainty are shown on Figure 5 for various depths. The maximum principal stress was found to be vertical below 700 m and is equal to the weight of overburden as determined from the rock density (0.026 MPa/m). Also, the orientation of the maximum horizontal principal stress is very close to that determined with the sole HTPF measurements.

The misfit between a given fault plane and a given stress tensor is characterized by the rotation which must be applied to the fault plane in order to bring the resolved shear stress supported by the fault parallel to the slip vector observed for this plane. A focal plane is considered inconsistent with a given tensor when its misfit is larger than three times the standard deviation associated with the plane orientation determination. The results obtained from the joint inversion are consistent with 21 of the HTPF measurements and 70% of the focal plane solutions. This clearly shows that a few microseismic events occur in zones of stress heterogeneity.

Given the observation mentioned earlier that fault zones involve small-scale fractures of very diverse orientation, it may be anticipated that locally, along the fault plane, the stress is very heterogeneous with respect to the regional stress field. Spectral analysis of the *P* waves for the microseismic signals reveals corner frequencies in the 200–500 Hz range (TALEBI and CORNET, 1987). Thus, the mean size of these events is estimated to stand somewhere between 0.5 and 5 m. This suggests that the rock volume affected by the stress heterogeneities causing the discrepancy between the observed slip plane and the estimated resolved shear stress, is of the same order of magnitude.

4. *Identification of Stress Heterogeneities near Fault Zones*

In order to easily conduct stress determination with the HTPF technique, MOSNIER and CORNET (1989) have developed a tool (the HTPF tool) combining an electrical imaging function with a wireline straddle packer. The electrical imaging function is used first to identify pre-existing fractures of various dip and azimuth in the borehole. Next, the straddle packer is placed precisely at the required depth, by means of real time imaging of the borehole wall, and hydraulic tests are run in order to measure the normal stress supported by these pre-existing

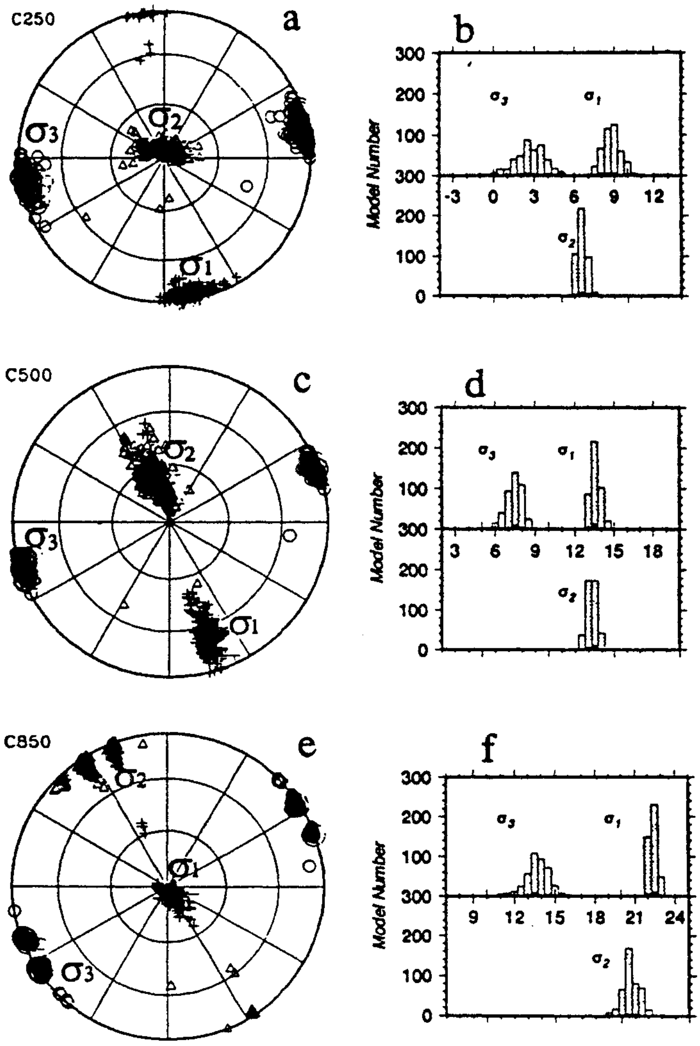

Figure 5
Stress determination obtained after integrating 22 HTPF measurements and 87 focal mechanisms. The stress field is presumed to vary linearly with depth. Results are shown at three different depths (250 m, 500 m, 850 m). a), c) and e) refer to the principal stress directions while the magnitudes (in MPa) are shown on b) d) and f). These results correspond to 430 models which are included within 95% confidence level.

fractures. This provides a unique opportunity to thoroughly investigate stress heterogeneities associated with local faults or altered zones.

As mentioned above, Cornet (1992) successfully used this technique to identify a stress perturbation in the vicinity of one of the most significant flowing zones in the well INAG III-9. Scotti and Cornet (1994a) analyzed two different mechanisms for modelling this observed heterogeneity. The first one assumes that the fault zone can be assimilated with a soft inclusion in an otherwise stiff rock; the second one supposes that the shear stress supported by the fault plane was partially released through creep or friction. Only the second mechanism (shear stress relief) was found to be consistent with observations. Further, this mechanism was also shown to be consistent with heterogeneities identified with the focal plane solutions of induced seismicity. Thus, a new set of HTPF measurements has been undertaken in order to determine whether the stress field near the two upper planar seismic zones is also heterogeneous with the regional stress field and consistent with a local shear stress relief. Results are shown in Table 3.

In Table 3, the measured values of normal stress are compared to the values computed with the regional stress field identified by the integrated method. Given the uncertainty on the orientation of the fracture planes (about 5°), many of these results are found to be consistent with the computed regional stress. Locally, within the depth interval at which the upper planar seismic zone intersects the well, some data are found to be heterogeneous while some nearby data (less than 6 meters away) are found to be consistent. This supports the proposition that very locally the stress field near and within fault zones is heterogeneous so that focal plane solutions of induced seismicity may not be representative of the regional stress field.

However, the most striking result is the observation that between 550 m and 611 m the measured normal stress is larger than the regional maximum principal stress, in some places by as much as 10 MPa. Clearly this observation does not fit the uniform shear stress relief process proposed by SCOTTI and CORNET (1994a), but requires some locally heterogeneous slip motion. It is not clear at this point whether this heterogeneity of slip motion is associated with the spatial extension of the fault zones or if it is associated with heterogeneous slip within the faults. The quality of the data does not provide means for precisely constraining the geometry of the fault zones. Nonetheless these results do demonstrate that faults are associated locally with very heterogeneous stress distributions so that focal plane solutions may not be representative of the regional stress field.

It is concluded that, when only focal mechanisms are used to determine the regional stress field, those which are clearly inconsistent with this regional stress are easily identified by the inversion technique, but those which are only slightly inconsistent influence the solution and induce some systematic error. Hence the different results obtained with the different sets of focal mechanisms, and the systematic error observed between fault plane inversions and HTPF measurements.

It could be argued that this conclusion is only valid for focal mechanisms of induced seismicity because of the small size of the events considered for this analysis. Although this will not be further discussed here, it will be mentioned that SCOTTI and CORNET (1994b) have reached conclusions similar to those presented here above, after comparing results from various HTPF stress determinations with the focal mechanisms of natural seismic events with magnitude ranging from 3 to

Table 3

HTPF data obtained in 1994 in order to explore the stress field in the vicinity of the upper and lower planar seismic zones. x_3, ϕ, θ, σ_n are respectively the values measured for the depth, the azimuth and the dip of the normal to the fracture plane and the normal stress supported by the fracture plane. ϕ_c, θ_c, σ_{nc} are the a posteriori values for ϕ, θ, σ_n as determined by the least squares inversion procedure. ε_ϕ, ε_θ, $\varepsilon_{\sigma n}$ are the standard deviations on the measurements. $\Delta\sigma_n$ is the difference between the measured value and that expected from the integrated stress determination. When $\Delta\sigma_n$ is larger than 1 MPa, the measurement is considered heterogeneous with the regional stress field; it is not considered for the stress determination. Note the strong heterogeneity around 600 m, i.e., in between the two planar seismic zones. Since these seismic zones exhibit very strong dip, they remain fairly close to the borehole for long depth intervals.

x_3 m	ϕ	ε_ϕ	ϕ_c	θ	ε_θ	θ_c	σ_n MPa	ε_{σ_n} MPa	σ_{n_c} MPa	$\Delta\sigma_n$ MPa
401	114,0	4	105,0	85,9	2	86,0	8,5	0,2	8,9	−0,4
482	115,0	4	117,0	80,1	2	80,0	12,3	0,5	11,6	0,7
501	68,7	4	73,0	89,0	2	88,9	9,6	0,2	9,3	0,3
554	132,0	4	132,6	89,1	2	89,1	14,3	0,3	14,2	0,1
558	103,2	5	118,8	88,5	2	88,4	15,3	0,4	13,7	1,6
665	196,0	4	193,0	85,5	2	85,43	12,8	0,3	12,6	0,2
678	187,0	4	179,4	85,5	2	85,3	14,8	0,3	14,4	0,4
686	180,0	4	188,6	73,3	2	74,1	13,3	0,3	13,7	−0,4
762	262,9	4	263,0	7,3	2	7,0	20,0	0,3	19,6	0,4
446	192,0			81,1			12,8	0,3	10,3	2,5
530	182,0			81,1			15,0	0,5	12,0	3,0
597	95,0			85,8			17,3	0,4	12,7	4,6
605	43,5			84,3			20,6	0,4	10,2	10,4
611	276,0			80,0			23,4	0,4	13,2	10,2
698	134,5			86,0			13,8	0,3	17,8	−5,0

4.5. Given the proposition that slip motion along faults is very heterogeneous (HERERO and PASCAL, 1994; COCHARD and MADARIAGA, 1994), it seems reasonable to anticipate that the stress field in the vicinity of fault zones is also very heterogeneous. This implies that some aftershocks of major seismic events are also very likely affected by local stress heterogeneities so that inversion of focal mechanisms of aftershocks may lead to biased stress determinations.

Further, considering the Le Mayet de Montagne results, one may wonder if the source of the heterogeneities are to be found in the morphology of the fault or simply in the heterogeneity of the slip motion along the fault. Answering this question will require some modelling which has not yet been done. Given the fact that many of the microseismic events are located a short distance from the main fault zone identified with the least-squares technique, and that most of the slip planes observed for these events are not parallel to this main fault plane, it seems very likely that morphology plays a significant role in developing the stress heterogeneities. This may in turn induce a heterogeneous slip motion along the main fault which may further enhance these stress heterogeneities. Only modelling, in close connection with detailed mapping of the stress heterogeneities, will help resolve this question. This modelling requires an accurate description of the local pore pressure within the fault. This is discussed now.

5. Analysis of the Consistent Focal Mechanisms for Pore Pressure Mapping

In addition to the regional stress determination, the joint inversion of HTPF data and focal plane solutions yields two results. First it identifies those focal mechanisms which are homogeneous with the regional stress field; then for these mechanisms it selects which of the two nodal planes is the slipping plane. This can be beneficial in obtaining some estimate of the friction coefficient for this rock mass. It can also be used to map the pore pressure perturbations induced by the fluid injections.

It is often assumed that the shear strength of pre-existing fractures obeys the effective stress principle (TERZAGHI, 1945), namely that the resistance to shear depends on the difference between the total normal stress (σ_n) supported by the fractures and the fluid pressure (p_p) assumed to act on the totality of the fracture area undergoing failure ($\sigma'_n = \sigma_n - p_p$). However, it also has been proposed (ROBINSON and HOLLAND, 1970) to consider that, since the pore space corresponds to a fraction of the total fracture area, only a fraction (β) of the pore pressure is to be considered for the effective normal stress ($\sigma'_n = \sigma_n - \beta p_p$). In the present paper we have considered both possibilities ($\beta = 1$ or $\beta = 0.9$) and assumed that the shear strength of pre-existing fractures follows Coulomb's friction law, with the assumption of zero cohesion

$$|\tau| = \mu(\sigma_n - \beta p_p) = \mu\sigma'_n. \tag{2}$$

The pore pressure at the location of a microseismic event can be written $p_p = p_0 + dp$, where p_0 is the original hydrostatic pressure and dp is the increment of pressure induced by the fluid injection. This yields

$$dp = \{(\sigma_n - \beta p_0)/\beta[1 - |\tau|/\mu(\sigma_n - \beta p_0)]\}. \tag{3}$$

The value of dp can be normalized with respect to p_i, where p_i is the increment of pressure with respect to hydrostatic pressure in the injection well at the depth of injection (i.e., the well-head pressure corrected for pressure losses caused by flow through the tubing in the injection well). In the rock mass, the ratio dp/p_i varies between 1, in the vicinity of the injection hole where pre-existing fractures are opened, and 0 near the production well or near the far field boundary, where the interstitial pressure is hydrostatic. On Figure 6, β is assumed to be equal to one (standard effective stress law) and the values for dp/p_i have been plotted versus the values of $|\tau|/\mu(\sigma_n - \beta p_0)$, first with μ equal to 1 (Fig. 6a), second with μ equal to 0.6 (Fig. 6b). It may be observed that if the friction coefficient μ becomes slightly larger than 1, then the local pore pressure increment required to induce shear would have to be larger than the injection pressure. Also, if the friction coefficient is equal to 0.6, the pressure required to induce slip for some events is about equal to hydrostatic pressure. Thus the friction coefficient is found to stand somewhere between 0.95 and 0.65, i.e., values which are fairly common for most rocks. Results shown on Figure 7 are similar to those of Figure 6 (for a friction coefficient of 0.5) except that β has been taken equal to 0.9 (the pore pressure is not acting throughout the complete area of the fracture). These results suggest that, with such an effective stress law, the pressure required to induce slip for some of the events is larger than the injection pressure. Yet for other planes, equilibrium is barely reached with hydrostatic pressure conditions. This demonstrates that for this rock mass Terzaghi's effective stress concept is satisfactory, so that the coefficient β in the effective stress law applied to friction, is equal to 1.

Now, given the stress field determined with the integrated method and given the selection of the nodal planes which results from this stress determination, the selected friction law as expressed by equation (3) may be used to map the pore pressure distribution within the rock mass. The normalized pressure increment dp/p_i has been plotted as a function of the distance between the hypocenter of the corresponding seismic event and the closest point in the injection well where water penetrates the rock formation (Figure 8). It can be seen, that for some events in the upper planar seismic zone, the pore pressure increment required to induce shear some 100 m away from the injection point is nearly equal to the injection pressure increment. This implies that either only slight flow occurs through this fracture or that its hydraulic conductivity is extremely high. As mentioned above, preliminary flow logs conducted in the well before the circulation tests, revealed that the fracture zone intersected by INAG III-9 around 500 m was taking no fluid during injection, contrary to the fault zone intersected around 650 m. Thus the large pore pressure identified by the seismic activity analysis is consistent with the flow logs conducted in the borehole: the upper planar seismic zone, although hydraulically conductive, is not connected to the main fracture network of the rock mass, but is connected to the injection well.

This mapping of the interstitial pressure in the upper seismic zone raises an intriguing question regarding the hydraulic behavior of this system. Indeed, at some places the local pore pressure is nearly equal to the injection pressure (the well-head injection pressure varies between 8.3 MPa at 8.5 l/s to 12.5 MPa at 20.8 l/s), and therefore is larger than the regional minimum principal stress magnitude in this depth interval ($\sigma_h = 7.5$ MPa at 500 m). Since stress heterogeneities are only localized, according to the good fit observed for many microseismic events, this should have resulted in the development of hydraulic fracturing. But none has been identified. Indeed, during all the injection tests a network of six tiltmeters continu-

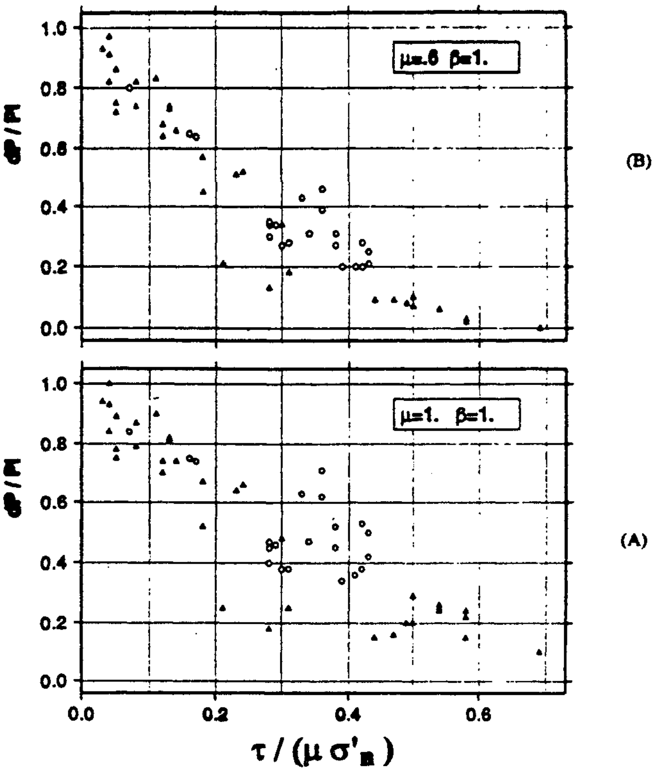

Figure 6
Calibration of the friction law controlling slippage along pre-existing fractures. On abscissa are plotted the values of the ratio between the tangential stress supported by the slip planes and the effective normal stress. On ordinate are plotted the ratio between the pressure increment required to induce slip and the injection pressure at the well head. A) The friction coefficient has been chosen equal to 1; B) The friction coefficient has been chosen equal to 0.6. In both cases the classical effective stress concept ($\beta = 1$) is assumed to be valid. Black triangles correspond to events in the upper planar seismic zone, open circles correspond to events in the lower planar seismic zone.

ously monitored the ground deformation (DESROCHES and CORNET, 1990). The absence of significant tilt during all the injection tests indicates that if any hydraulic fracture did propagate, it remained smaller than 15 to 20 m. Thus this analysis suggests that, within fault zones, the pore pressure may be significantly larger than the minimum principal stress without significant hydraulic fracturing, and this for time periods exceeding fifteen days.

The lateral extension of the lower planar seismic zone is considerably smaller than that of the upper seismic zone. Also, the pore pressure determined from the analysis of the induced seismicity is found to be substantially lower than within the upper seismic zone, and the values are decreasing regularly as the events occur

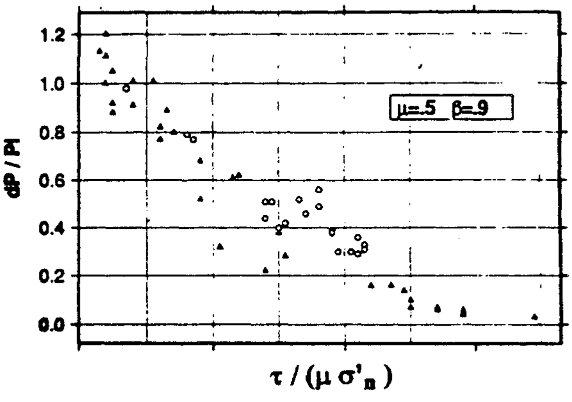

Figure 7
Same as Figure 6 but, in the effective stress law, β has been chosen equal to 0.9. Further, the friction coefficient has been chosen equal to 0.5.

further away from the well. This is consistent with the result from the flow logs which shows that this fault zone is well connected to the hydraulically significant fracture network of the rock mass.

This emphasizes the fact that induced seismicity is only representative of large pore pressure and not of large flow rate. In fact, the further away the microseismic events are from the injection well, the less likely they are to be associated with main flowing zones. Indeed, the interstitial pressure within the distant flowing zones is controlled by the far field pressure conditions and therefore, in opened systems, is too low to induce any seismicity. This is confirmed by the horizontal projection of the location of induced seismicity observed at Le Mayet de Montagne. It is observed on Figure 1 that, during injections in INAG III-9, no seismic event occured near INAG III-8 (the production well) even though the well was producing somewhere between 45% and 80% of the injection flow rate (depending on the injection flow rate). This absence of seismicity near INAG III-8 is simply linked to the low pore pressure in the vicinity of the production well.

It may be observed that none of the planar seismic zones is parallel to a principal stress direction. Thus, at least at the scale of these tests, for this granite, forced fluid flow does not occur along planes normal to the minimum principal stress but rather is controlled by a few pre-existing faults. Further, these results outline the difficulty in characterizing the hydraulic behavior of this rock mass and the shortcomings of the equivalent continuum approach: only three of four main fractures are absorbing more than 80% of the flow (Bruel and Cornet, 1992) and these can be identified only through large-scale testing. Indeed, had straddle packer tests been conducted on the various fractures intersected by the wells, these tests would have shown that the zone around 500 m is locally hydraulically conductive

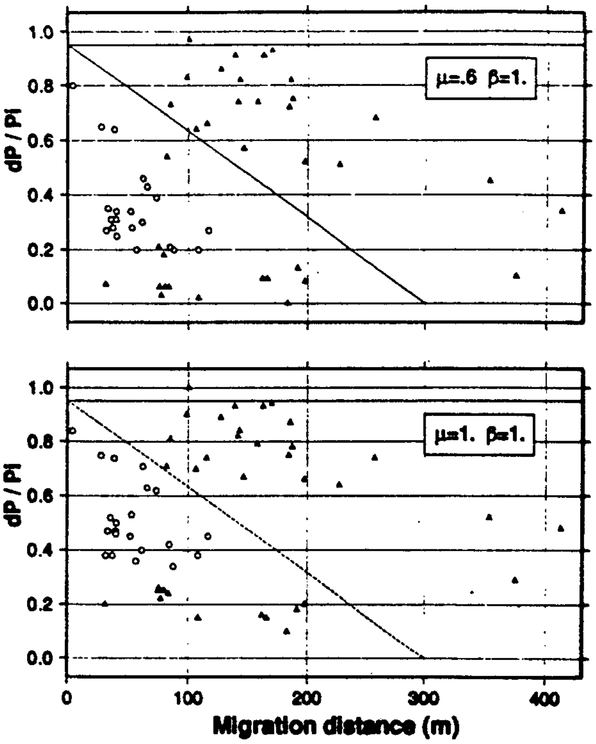

Figure 8
Mapping of the pore pressure in the rock mass during the various injections. For all focal mechanisms consistent with the integrated stress determination, the pressure increment (normalized with respect to the well-head injection pressure) required to induce slip is plotted versus the distance between the event and the closest injection point in the well (plotted in abscissa). Black triangles corrrespond to the upper planar seismic zone, the open circles refer to the lower planar seismic zone. μ is the friction coefficient, β is the corrective factor for the pore pressure in the effective stress law.

and they would have failed to identify the lack of connection at the 200 m scale. This dominance of a very limited amount of fractures on the hydraulic response of the system clearly illustrates that the concept of permeability of an equivalent continuum fails for this granite. This then raises the question of characterizing the large-scale hydraulic response of this rock mass to forced fluid flow. As shown here above, the detailed analysis of the focal plane solutions of induced seismicity, together with a sound regional stress determination, may yield part of the answer.

6. *Conclusion*

The mapping of seismic events induced by various water injections in this granite has shown that flow only occurs through a very limited number of fractured zones. Some of these zones, although locally hydraulically conductive, are not hydraulically significant because they are not properly connected to the regional hydraulically significant system. All these fault structures exhibit a fairly intricate morphology so that locally the stress may be somewhat heterogeneous with respect to the regional stress field. This precludes identifying the regional stress field from the sole inversion of such locally induced focal mechanisms.

However, when combined with HTPF normal stress measurements, focal mechanisms of induced seismicity can be beneficial in efficiently constraining the regional stress field. The fact that this integrated stress determination has yielded for the Le Mayet de Montagne site a principal stress component in the vertical direction, when this was not imposed *a priori* in the inversion, is taken as a proof of the effciency of the method.

This precise regional stress determination shows that the stress heterogeneities observed along the fault zones are fairly localized and leave many portions of the fault unperturbed as demonstrated by the many consistent focal mechanisms identified within the fault zones. These numerously consistent focal mechanisms have been advantageously utilized to map the interstitial pressure. This mapping has shown that locally the pore pressure may be considerably larger than the regional minimum principal stress magnitude. Yet, no large-scale hydraulic fracture has been identified, either from the surface tilts or from the flow characteristics (a hydraulic fracture should be associated with large fluid flow, when very little has been observed in practice). The cause of this metastable situation is probably to be found in the morphology of the fault zone. This suggests that, in natural faults, the pore pressure may reach values extensively larger than the regional minimum principal stress, without inducing hydraulic fracturing, and this for a reasonably long duration (more than fifteen days in the case of Le Mayet de Montagne).

Acknowledgements

This research was supported by the European Economic Communities Directorate General XII (contract EN3G-0051-F), by Programme Interdisciplinaire de Recherche Sur l'Ênergie et les Matières premières (PIRSEM) from Centre National de la Reserche Scientifique and by Agence Française pour la Maitrise de l'énergie. This work benefited greatly from the assistance of B. Bert for his technical contribution in all field work. Y. Willeveau, O. Scotti and G. Rozières assisted in some of the HTPF stress determinations.

REFERENCES

BOTT, B. (1959), *The Mechanics of Oblique Slip Faulting*, Geol. Mag. *96* (2), 109–117.

BRUEL, D., and CORNET F. H., *Force fluid through fractured reservoirs modelling*. In *Fractured and Jointed Rock Masses* (eds. N. G. W. Cook and L. Myer) (Lawrence Berkeley Lab. Report LBL-32379, 3, 1992) pp. 519–526.

Cochard, A., and Madariaga, R. (1994), *Dynamic Faulting under Rate-dependent Friction*, Pure and Appl. Geophys *142* (3/4), 419–445.

Cornet, F. H., *Experimental investigation on forced fluid flow through a granite rock mass.* In *Fourth European Geothermal Update* (eds. K. Louwrier, E. Staroste, and J. Garnish) (Kluwer Academic Pub. Dordrecht, Holland 1989) pp. 189–204.

Cornet, F. H., *In situ stress heterogeneity identification with the HTPF tool. In Rock Mechanics, Proc. 33 rd US Symposium on Rock Mechanics* (eds. Tillerson and Wawersik) (Balkema, Rotterdam 1992) pp. 39–48.

Cornet, F. H., Hosanski, J. M., Bernaudat, F., and Ledoux, E., *Shallow depth experimentation on the concept of energy extraction from deep hot dry rocks.* In *Hydraulic Fracturing and Geothermal Energy* (eds. S. Nemat-Nasser, H. Abe, and S. Hirakawa) (Martinus Nijhoff, The Hague 1982) pp. 385–403.

Cornet, F. H., and Julien, Ph. (1989), *Stress Determination from Hydraulic Test Data and Focal Mechanisms of Induced Seismicity*, Int. J. Rock Mechanics Min. Sci. and Geomech. Abs. *26* (3/4), 235–248.

Cornet, F. H., Yin J., and Martel L., *Stress heterogeneity and flow path in a granite rock mass.* In *Fractured and Jointed Rock Masses* (eds. N. G. W. Cook, and L. Myer) (Lawrence Berkeley Lab. Report LBL-32379, vol. 1, 1992) pp. 80–87.

Cornet, F. H., and Scotti, O. (1993), *Analysis of Induced Seismicity for Fault Zone Identification*, Int. J. Rock Mech. Min. Sci. and Geomech. Abs. *30* (7), 789–795.

Desroches, J., and Cornet, F. H., *Channelling stiffness effects on fluid percolation in jointed rocks.* In *Rock Joints* (eds. N. Barton, and O. Stephanson) (Balkema, Rotterdam 1990) pp. 527–534.

Fehler, M. C. (1989), *Stress Control of Seismicity Patterns Observed during Hydraulic Fracturing Experiments at the Fenton Hill Hot Dry Rock Geothermal Energy Site, New Mexico*, Int. J. Rock Mech. Min. Sci. and Geomech Abs. *26*, (3/4) pp. 211–219.

Gephart, J. W., and Forsyth, D. W. (1984), *An Improved Method for Determining the Regional Stress Tensor Using Earthquake Focal Mechanism Data: Application to San Fernando Earthquake Sequence*, J. Geophys. Res. *89* (B11), 9305–9320.

Herero, A., and Bernard, P. (1994), *A Kinematic Self-similar Rupture Process for Earthquakes*, Bull. Seismol. Soc. Am. *84* (4), pp. 1216–1228.

House, L. (1987), *Locating Microearthquakes Induced by Hydraulic Fracturing in Crystalline Rock*, Geophys. Res. Lett. *14*, 919–921.

Julien, Ph., and Cornet, F. H. (1987), *Stress Determination from Aftershocks of the Campania-Lucania Earthquake of November 23, 1980*, Ann. Geophys. *5B* (3), pp. 289–300.

McGarr, A. (1980), *Some Constraint on Levels of Shear Stress in the Crust from Observations and Theory*, J. Geophys. Res. *85* (B11), pp. 6231–6238.

Mosnier, J., and Cornet, F. H., *Apparatus to provide an image of the wall of a borehole during a hydraulic fracturing experiment.* In *Fouth European Geothermal Update* (eds. K. Louwrier, E. Staroste, and J. Garnish) (Kluwer Academic Pub., Dordrecht 1989) pp. 205–212.

Niitsuma, H., Nakatsuka, K., Takahashi, H., Abe, M., Chubachi, N., Yokoyama, H., and Sato, R., *In situ AE measurements of hydraulic fracturing at geothermal fields.* In *Hydraulic Fracturing and Geothermal Energy* (eds. S. Nemat-Nasser, H. Abe, and S. Hirakawa) (Martinus Niijhoff, The Hague 1982) pp. 227–241.

Pearson, C. (1981), *The Relationship between Microseismicity and High Pore Pressure during Hydraulic Stimulation Experiments in Low Permeability Granite Rocks*, J. Geophys. Res. *86*, 7855–7864.

Pine, R. J., and Batchelor, A. S. (1984), *Downward Migration of Shearing in Jointed Rock during Hydraulic Fracturing*, Int. J. Rock Mechanics Min. Sci. and Geomech. Abs. *21*, 249–263.

Rice, J. (1993), *Spatio-temporal Complexity of Slip on a Fault*, J. Geophys. Res. *98* (B6), 9885–9907.

Riveira, L., and Cisternas, A. (1990), *Stress Tensor and Fault Plane Solutions for a Population of Earthquakes*, Bull. Seismol. Soc. Am. *80* (3), 600–614.

Robinson, L. H., and Holland, W. E., *Some Interpretation of pore fluid effects in rock failure.* In *Rock Mechanics—Theory and Practice, Proc. 11th Symp. on Rock Mech.* (ed. W. H. Somerton) (Soc. Min. Eng., Am. Ins. Min. Met. Pet. Eng., New York 1970) pp. 585–597.

SCOTTI, O., and CORNET, F. H. (1994a), *In situ Evidence for Fluid Induced Aseismic Slip Events Along Fault Zones*, Int. J. Rock Mech. Min. Sci. and Geomech. Abs. *31* (4), 347–358.

SCOTTI, O., and CORNET, F. H. (1994b), *In situ Stress Fields and Focal Mechanism Solutions in Central France*, Geophys. Res. Lett. *21* (22), 2345–2348.

TALEBI, S., and CORNET, F. H. (1987), *Analysis of the Microseismicity Induced by a Fluid Injection in a Granite Rock Mass*, Geophys. Res. Letts. *14* (3), 227–230.

TERZAGHI, K. (1945), *Stress Conditions for the Failure of Saturated Concrete and Rock*, Proc. Am. Soc. Test Mat. *45*, 777–801.

VASSEUR, G., ETCHECOPAR, A., and PHILIP, H. (1983), *Stress State Inferred from Multiple Focal Mechanisms*, Ann. Geophys. *1*, 291–297.

WALLACE, R. E. (1951), *Geometry of Shearing Stress and Relation to Faulting*, J. Geology *59*, 118–130.

YIN, J., *Détermination du Champ de Contrainte Régional à Partir de Mesures Hydrauliques et de Mécanismes au Foyer de Microséismes Induits*, Thèse de Doctorat de l'Univ. Paris VII et de l'Inst. Phys. Globe de Paris 1994.

YIN, J., and CORNET, F. H. (1994), *Integrated Stress Determination by Joint Inversion of Hydraulic Tests and Focal Mechanisms*, Geophys. Res. Lett. 29 (24) 2645–2648.

Received November 18, 1994, revised March 31, 1995, accepted April 10, 1995.

How close to failure is a natural granite rock mass at a 5 km depth ?

F.H. Cornet, Th. Berard and S. Bourouis.
Institut de Physique du Globe de Paris

Abstract

Linear variations with depth for principal stress magnitudes have been described often in crystalline rocks. This is taken as a support to the hypothesis that the earth crust is just at equilibrium through frictional resistance of optimally oriented faults and fractures. Large scale injection experiments, conducted in the 5 000 m deep experimental geothermal reservoir at Soultz (France), provide unique data to test this proposition. Results from hydraulic tests together with analysis of borehole images and induced seismicity are integrated to provide a well constrained characterization of the complete stress field down to 5 km. The vertical stress component is shown to be principal and the maximum horizontal principal stress orientation is N 170±15°E, i.e. parallel to the direction observed at similar depth, at Urach some 120 km to the South East of Soultz, as well as at the KTB site some 300 km East of Soultz. A large scale injection experiment was undertaken in 1993 within this virgin rock mass, at progressively increasing flow rates (25 000 m^3 total injected volume), between 2850 m and 3400 m. When the wellhead pressure reached 4 MPa induced seismicty was observed but the rock mass remained in its elastic domain. Only when the well head pressure reached 8 MPa, were large failure processes initiated. Detailed relocation of microseismic events together with borehole images taken before and after the experiment demonstrate that fresh shear zones have been formed by the coalescence of multiple smaller scale fractures. It is concluded that, at Soultz, the linear variations with depth of stress magnitudes depend at least partly on the long term rheology of the rock mass and should not be used to evaluate the frictional characteristics of the main faults. It is also shown that pore pressure increments larger than 8 % of the natural minimum principal stress magnitude are required to induce large scale shear failure, in this granite.

1 Introduction

As stated by Charles Fairhurst [1] : “the distribution of forces in rock masses is a central concern of rock mechanics, both with respect to understanding basic geological processes such as plate tectonics and earthquakes, and the design of engineered structures in and on rock masses”. Charles has much contributed to this topic since his first review for the U.S. Corps of Engineers in 1968 [2], review that was used as text book by the first author of the present paper during his Minnesota years. The objective of the present paper is to explore some applications of the principles developed in Charles's laboratory for estimating rock stresses at great depth. In particular it is shown how an integration of complementary data is necessary to assessing the stress field at great depth as well as the factors controlling its vertical variations.

Because stresses in the crust must satisfy the stability of optimally oriented preexisting fractures and faults, Brace and Kohlstedt [3] have proposed upper limits to maximum differential effective stresses that may exist in the crust. Many an investigator [e.g. 4, 5, 6] has analyzed results from deep stress measurements and has noted a linear variation of stress magnitudes with depth. This linear variation is consistent with the hypothesis that stresses fit equilibrium conditions according to the so-called Byerlee's law [7] on rock friction, i.e. a Coulomb friction law with no cohesion and friction coefficients ranging from 0.6 to 1.

In practice, an important question is to determine how far the crust is from equilibrium, depending on the regional tectonic conditions. Following the rock engineer, it is obvious that very often a rock mass can sustain significant stress perturbation and yet remain stable. But following recent results from the Earth Science literature [e.g. 8], it is clear that locally stresses may be close to equilibrium condition, i.e. close to the onset of failure.

This consideration is of particular import when it comes to the stability of long term underground storage facilities, whether it involves the temporary storage of oil or gas, or the permanent disposal of waste (e.g. CO2, nuclear waste, etc..). For example, a 1 MPa difference in acceptable changes in interstitial pressure for gas storage implies drastic variations in the storage capacity of a repository. Given that the onset of microseismicty is often taken as a demonstration of the onset of failure, providing a better understanding of the onset of microsismicity and its relation to rock mass stability becomes an important issue to rock engineering.

We discuss in this paper results from large scale injection experiments that have been undertaken in the context of the development of an artificial geothermal field. Since 1987, an experimental geothermal program is on-going at Soultz-sous-Forêts, in the upper Rhine graben, close to the Franco-German border (figure 1). The objective is to investigate the possibility of developing a heat exchanger in the local granite basement, at depths of the order of 5 km, so as to produce economically electricity [9, 10].

A first borehole, GPK1, was initially drilled down to 2000 m and then deepened to 3600 m in 1992. This well was used for massive hydraulic testing in 1993. A nearby well, EPS1, reached 2200 m in 1990 and was used for small-scale hydraulic tests, some 500 m away from GPK1. Another well, GPK2, was drilled in 1995 down to 3800 m, close to EPS1. After massive hydraulic stimulation in 1997, it was deepened to 5 km in 1999, with yet another massive hydraulic stimulation in 2000 [11]. Since 2001, reservoir development is on-going in the 5-km depth range, including the drilling of two additional 5 km deep boreholes GPK3 and GPK4 and their stimulation [12, 13].

This has provided a diversity of data that has been used by various groups to estimate the local stress field. Numerous papers have been published with this respect. Principal stress directions determination range from N125°E to N185°E and a large variety of principal stress magnitude estimates have been proposed, some of them leading to instability above 2000 m (the minimum principal stress becomes smaller than the hydrostatic pressure).

In this paper we review first the various results that have been published with respect to the regional stress field determination and we discuss possible sources of error. Then we present a vertical stress profile that integrates complementary data deemed reliable and obtained during the early phase of the project, before any large scale perturbation altered the regional stress field. Results are compared to those from the latest large scale hydraulic stimulation run in GPK3, around the depth of 5 km [13], i.e. about 2 km deeper than the domain in which the stress profile has been established. This validated stress profile is taken to advantage for discussing the growth of zones of microseismic activity generated during the initial 1993 massive hydraulic injections, i.e. in the virgin rock mass. Finally a criterion of failure for the whole rock mass is proposed and discussed with respect to the onset of microseismicity.

2 Results from hydraulic testing

Various hydraulic tests have been conducted on this site, from straddle packer tests for stress measurements to tests for large-scale hydraulic reconnaissance or for reservoir development.

Injected volumes range from tens of litters up to tens of thousands of cubic meters at flow rates ranging from liters per minute to several tens of liters per second. Only tests relevant to stress determination are reviewed in this section. They correspond to tests in which the water pressure has been large enough to induce the mechanical opening of fractures.

2.1 *Tests specific to stress measurements*

The first tests for stress measurements [14] were run with rubber straddle packers (2.4 m and 3.6 m long pressurized intervals), in well GPK1, following the classical methodology of stress measurements (i.e. low flow rates (9 l/min) with total injected volume in the range of 50 to 100 litters).

Fracture orientations were determined from borehole televiewer logs, and this raised some difficulty. Indeed, discrepancies of several meters between absolute depths readings on logs are common for depths larger than 1000 m, and this raises difficulties for correlations with depth measurements from drill string assembly. Pressures were recorded at ground surface. Results are presented in table 1. They show a large dispersion in fracture orientation, and for two tests two fractures are observed in the tested interval. The last line corresponds to a test run with a single packer set at 1968 m with the interval extending to the bottom of the well (2000 m). The two last tests of table 1 are part of the set of tests run for preliminary hydraulic reconnaissance discussed in the next section. They are given here for they were part of the initial stress determination proposed by Rummel and Baumgartner [14].

Additional stress measurements (Table 2) were run with aluminum straddle packers [15]. For these tests, pressure measurements were obtained downhole. Two tests were run in the inclined well EPS1 around 2200 m (total borehole length) and another two in the vertical well GK1 (3315m and 3506 m). No fracture orientation is reported for these tests. Further, while the borehole length is identical to depth in the vertical well GPK1, this is not the case for well EPS1 which exhibits an increasing deviation with depth, the deviation reaching 25° at its bottom. Further EPS1 well-head is 22 m above that of well GPK1. Hence borehole lengths in well EPS1 do not translate immediately in equivalent depths in well GPK1.

2.2 *Tests for small scale hydraulic reconnaissance*

Another set of data is provided by preliminary hydraulic reconnaissance. In particular, Jung [16] conducts in 1988, a hydrofrac test between 1968 m and the bottom of well GPK1 (i.e. 2000 m at this time). In this test, the 30 m long pressurized interval ends with the bottom of the well and is sealed at its top by a double packer system. After preliminary tests have opened vertical fractures, an injection test is conducted with a 3.5 l/s flow rate and a 3.7 m^3 total injected volume, i.e. about one order of magnitude larger than those used for stress measurements. The well-head pressure measured at shut-in (i.e. when the drill pipe to the surface was filled with fresh water) is 6.5 MPa, so that the bottom-hole pressure is close to 26.0 MPa. Borehole televiewer surveys reveals newly formed vertical fractures oriented N170° to the East as well as two inclined preexisting fractures striking N 150° and dipping 78°.

In 1991, after additional stimulation tests were run in the same GPK1 interval, Jung conducts an injection test with a 15 l/s flow rate. At first the increase in borehole pressure is linear, but becomes non-linear before reaching its peak. The transition from linear increase to non-linear increase in borehole pressure is typically taken as the reopening pressure. Many an experimentalist has shown that this value is generally close to the minimum principal stress magnitude [17,18]. Interestingly, this reopening pressure (figure 2) is found to be equal to 26.5 MPa, i.e. very close to the shut-in value measured 3 years earlier. Hence it is considered that 26.3 MPa is a close estimate of the minimum principal stress magnitude around 1980 m.

2.3 *large scale hydraulic reconnaissance and reservoir stimulation.*

In September 1993, a large scale injection is conducted in the open-hole section of GPK1, extending from 2850 m down to 3400 m [19,20]. The injection starts at a flow rate of 0.25 l/s and is progressively increased to 6 l/s within 60 hours. From then on, the flow rate is kept constant for 48 hr, followed every other day by increments of 6 l/s until the injection flow rate reaches 36 l/s. At this final flow rate, injection lasts 3 days (fig.3). In response, the wellhead pressure initially increases regularly with flow rate but then progressively stabilizes at about 10.5 MPa and becomes nearly independent of flow rate once it reaches 24 l/s. During the whole process, microseismic activity is recorded by three downhole 3D-accelerometers and one hydrophone [21]. Concomitantly with the pressure stabilization, the cloud of microseismic activity is found to migrate upward, a feature that is taken as a proof that the water pressure has reached the magnitude of the minimum principal stress, leading to mechanical opening of fractures oriented close to the maximum horizontal stress direction.

Hence, the value of 39.5 MPa is likely a close estimate of the minimum principal stress magnitude around 2900 m. This is further discussed in section 4.

Somewhat similar large scale injection tests have been undertaken later, for reservoir development [22,11] but in none of these tests was the injection pressure found independent of injection flow rate. However, in 2003, a stimulation test was run around the depth of 4550 m and during this large scale injection the wellhead pressure did become independent of injection flow rate [13]. This is further discussed in section 5.2.

2.4 *Previously published stress evaluations from hydraulic tests*

This set of data has prompted many authors to propose an estimation of the stress field at depth, in the Soultz granite.

In 1990, Rummel and Baumgartner [14], apply the HTPF stress determination technique [17,23] to fit a five parameter stress model to the five successful hydraulic tests that had yielded both the measurement of the normal stress and the orientation of the tested preexisting planes (Table 1). They come up with the following solution:

$$S_h = 15.1 + 0.0179\,(z-1458) \qquad (1a)$$

$$S_H = 24.8 + 0.0198\,(z-1458) \qquad (1b)$$

$$S_v = 0.024\,z \qquad (1c)$$

Direction of S_H N 155 ± 3 , or N 176 ± 6°, depending on the fractures considered for the HTPF inversion.

In (1), S_h, S_H and S_v are respectively the minimum horizontal, the maximum horizontal, and the vertical principal stress components (in MPa) while z is depth (in meters). Rummel and Baumgartner outline that this solution is valid only for depths larger than 1458 m. Indeed, for shallower depths, the solution yields magnitudes of the minimum principal stress smaller than the interstitial pore pressure (given a density for the brine equal to $1.07 g/cm^3$).

In 1990 Jung [16] observes that, while Rummel and Baumgartner solution with S_H in the N 155°E direction does explain his hydraulic results, a N 170°E orientation for the maximum horizontal principal stress direction explains them even better.

In 1993, although no fracture orientation has been identified for the tests shown in table 2, Klee and Rummel [15] observe that the shut-in pressure for these tests align well with the minimum principal stress value given by solution (1). They conclude that the tests with aluminum packer have generated true hydraulic fractures, so that these results can be interpreted according to the classical hydraulic fracturing theory. They assume that, for this granite, both pore pressure and rock tensile strength are to be neglected for the computation of the maximum principal stress magnitude. Because results fit reasonably well with extrapolation from the 1990 results, they conclude that the maximum horizontal principal stress orientation is that already determined and conclude for a NW (N135°E) to NNW (N157.5°E) direction for the maximum horizontal principal stress.

In 1994, upon examination of both electrical and acoustic imaging logs, Heinemann and Kappelmeyer [24] report that Klee and Rummel's hydraulic test at 3315 m, in GPK1, is associated with a clearly identified vertical fracture in the N-S direction but that the test at 3506m is associated with a vertical fracture oriented nearly E-W. Interestingly, this latter test was run within meters of one of the most significant fault intersected by the well GPK1. i.e. within a zone of stress heterogeneity. After detailed analysis of rock density on cores and on cuttings samples, they interpret all data available till July 1993 with the following solution:

$S_h = 15.8 + 0.0149\,(z-1458)$ (2a)
$S_H = 23.7 + 0.0336\,(z-1458)$ (2b)
$S_v = 33.8 + 0.0255\,(z - 1377)$ (2c)
Direction of S_H N 170°. (2d)

These various stress profiles will be discussed after having analyzed the borehole wall images in wells GPK1 and GPK2 and after having discussed results from induced seismicity.

3 Results from electrical and acoustic borehole imaging

Very significant constraints on principal stress orientations are provided by borehole failure processes as observed with both electrical and acoustic borehole imaging tools.

3.1 *Drilling induced, thermal fractures*

In 1988, Mastin and Heinemann [25] conduct an analysis of both four-arm caliper and acoustic borehole televiewer logs run in well GPK1. The caliper log runs from 1420 m to 2000 m and the televiewer log runs from 1415 m to 1999 m. The four-arm caliper tool does not outline any significant borehole cross-section elongation in most of the well, although it is reported to lock in steady orientation between 1734 m and 1690 m. The direction corresponds to that of sub-vertical drilling induced fractures observed in the televiewer log, the mean orientation of which is N 169±21° . They conclude that this direction is that of the maximum horizontal principal stress and propose that the caliper tool locked in steady orientation because of thermal fractures. These authors also notice that, after correction for tool eccentering effects, some slight borehole cross-section elongation is noticed on the televiewer data. They outline their regular elliptical shape as opposed to that of spalled zones normally associated with breakouts caused by failure in compression. This leads them to conclude that these elongations have been generated by tool drag, even though their orientation (N 185 ± 30°) does not coincide with that of the borehole deviation, as normally expected.

In 1999, Brudy and Zoback [26], discuss results from the electrical imaging log run in GPK1, after it had been extended to 3590 m. They report on results by Nagel [27] who obtained a mean orientation for the induced tensile fractures equal to N181 ± 22°, for the 2000-3590 m depth range. Then they concentrate on stress magnitudes required for thermal tensile fractures to appear and conclude on the necessity to assume a zero tensile strength for this granite.

We outline here that these results on the pervasiveness of tensile fractures generated during drilling raises a major question on the possibility of sealing borehole sections with inflatable straddle packers, for stress measurement by hydraulic tests. This is further discussed in section 5.

3.2 *Borehole cross section elongation analysis*

Bérard & Cornet [28] analyze a set of four Ultrasonic Borehole Imager (UBI) logs for wells GPK1 (logs between 2850 and 3465 m and between 2853 and 3516 m) and GPK2 (logs between 1422 and 3807m and between 3479 m and 3866 m). Logs in GPK1 were run 6 months before, and 2 months after, the first large scale injection test reported here above, i.e. more than a year after the deepening of GPK1. The first log in GPK2 was run three days after the end of the first drilling operation while the second log was run during the well deepening operation.

Bérard and Cornet observe, in GPK1, classical compression breakouts below the depth of 3 km, with a N 95 ± 7 ° orientation (fig 4). For the first log in GPK2, that was run three days after the end of drilling, no breakout is observed at depths comparable to those for which breakouts have been observed in GPK1. Some are noticed occasionally, further down. Their mean orientation is N 93± 25°. Interestingly, none is observed in the second log run during the deepening of the well.

But in GPK2, they observe in the 1.6 - 2.9 km depth range, borehole cross-section elongations with a mean orientation N 164° ± 18°. A detailed description of orientations distribution is given in figure 5. It outlines a non-symmetrical distribution with respect to the peak value (N 169°E), with two secondary peaks at respectively 155° and 135°.

These borehole cross-section elongations are very strongly developed around 1600 m and disappear very progressively with depth, concomitantly with drilling induced fractures. They definitely would have been picked with a four-arm caliper tool, in a manner similar to what is described by Mastin and Heineman [25] in the upper part of GPK1. For the drilling induced fractures in GPK2, between 1420 and 3500 m, a N175°±17° mean direction is reported by Genter & Tenzer [29] i.e. about 10° to the North of the mean thermal elongation orientation.

The shape of these borehole cross-section elongations is much more regular than classical compression breakouts. After detailed analysis of their radius of curvature, Bérard and Cornet conclude that these elongations are not caused by tool drag but are associated with intense inter-crystalline thermal microcracking. This is also supported by the very progressive decrease of their amplitude with depth, simultaneously to the decrease of drilling induced thermal perturbation.

In conclusion, compression breakouts are observed below 3 km depths, on logs run after one year has elapsed since the end of drilling. They are not observed on logs run during, or just after drilling. Unless this time dependency is better understood, it precludes an accurate quantitative evaluation of stress magnitude from breakouts width and/or radial extent. Three mechanisms may be considered for explaining this time dependency :

- ✓ the progressive cancellation of thermal stresses,
- ✓ the time dependency of rock failure in compression [30,31,32,33] that may be enhanced by temperature,
- ✓ the diffusion of pore pressure in failing zones.

The magnitude of thermal stresses computed by Bérard & Cornet [28] at depths greater than 3 km shows that thermal stresses are not very significant. Hence, only the two last effects are considered likely candidates for the observed time dependency. But unfortunately no data is available for ascertaining potential stress corrosion effects at this site.

Independently of compressive breakouts, thermal stresses have induced borehole cross-section elongation in the direction of the maximum horizontal principal stress. These thermal elongations are observed only when the tensile stresses are increased very progressively. They reduce the apparent tensile strength of the granite to very small values. When thermal stresses are applied at once, as done during large scale injections, the inter-crystalline micro-cracking has no time to develop and single macroscopic fractures are generated at once. Once formed, these macrofractures relax the tensile stresses near the wellbore wall and concentrate them at the tip of the macroscopic fracture, thus stopping the development of microcracking. Had such borehole cross-section elongations been confused with compression breakouts, this would have lead to erroneous conclusions on principal stress direction. A characteristic feature of thermal elongation is their vanishing together with the decrease in drilling induced thermal perturbation so that, at Soultz, they disappear with depth contrary to compressive breakouts.

4 **Results from seismic monitoring**

During all the various injections tests run at Soultz, induced microsismic activity has been monitored. We concentrate in this section on the first large scale injection experiment, for it corresponds to an experiment in the original unperturbed natural rock mass. Two monitoring networks were available.

The CSMA downhole network includes three 3D-accelerometers and one hydrophone located close to the interface between sedimentary rocks and the granite around 1400 m and was operated by the Camborne School of Mines Associates [21]. In addition, a surface network of 14 stations (8 single vertical (1Hz) component seismometers and 6 three-components (2Hz) seismometers) was deployed on ground surface, thus providing means to identify focal mechanisms [34,35]. It is referred to as the EOPGS network and was operated by Ecole and Observatoire de Physique du Globe de Strasbourg.

4.1 *Structure of the micro-seismic cloud*

About 10 150 events have been recorded with the CSMA network between Sept. 2 and Sept. 15, i.e. the complete duration of the injection. In figure 3 are shown horizontal projections of these micro-seismic events for two different horizontal depths range in the rock mass. Locations are determined from P and S arrivals [21]. An isotropic velocity structure has been established from calibration shots. Station delays of a few milliseconds are introduced at the stations in order to fit results from calibration shots more closely. The 60% confidence level on these locations is 30 m in the East-West direction, 60 m in the North-South direction and 20 m in the vertical direction.

Events with depths ranging from 2900 m to 2700 m indicate a N-S extension of the seismic cloud, while events located below 3000 m are consistent with a NNW-SSE preferential orientation. The well trajectory is subvertical and thus perpendicular to the plane of the projection. It is located within the seismic clouds.

In order to obtain a better understanding of this microseismic cloud, Bourouis [36] has identified and analysed multiplets within the 9 200 events for which proper recording was available. The concept of multiplet was initially introduced by Poupinet et al. [37] and has been applied with success in many instances for accurate relocation purposes [38, 39, 40]. A multiplet is a set of microseismic events in which all events exhibit very similar seismic signals. They are generated by the same seismic source that is reactivated over time for various reasons. Cross correlation between these signals provides means to relocate very accurately these events with respect to one another (relative relocation accuracy of a few meters). A total of 597 doublets (only two event of similar waveform), 236 triplets (3 similar events), and 350 multiplets (four similar events or more) have been identified. Some multiplets involve more than 30 similar events. These multiplets are considered to be associated with repeated slips on the same local feature.

The best plane that fits these relocations has been calculated according to the "three points" method proposed by Fehler et al. [41]. Very schematically, the method identifies the plane that is the most often generated when considering any combination of three events within the set. A normalizing procedure is applied in order to avoid bias induced by the shape of the multiplet.

Once multiplets have been characterized, the best large scale planar structure that fits the volume of multiplets, for a given depth range, is identified. By planar structure we refer to a structure the thickness of which is small as compared to the two other dimensions.

The majority of multiplets exhibit, individually, an azimuth often close to the N 155°E orientation, but the planar structure that is created by the envelope of these multiplets varies and exhibit a remarkable rotation with depth, as shown on table 3. The vertical extent of depth intervals have been chosen so as to include approximately the same number of events.

Hence, while borehole images do not indicate any significant rotation of the principal stress directions within the depth interval of interest, clearly such is not the case for the seismic cloud mean orientation. This rotation is considered to be representative of macroscopic failure processes that vary with depth depending on the relative value of borehole and interstitial pore pressure with respect to the natural stress field, as discussed in section 6.

4.2 *Focal mechanisms of induced sismicity and stress heterogeneity*

While the downhole seismic stations recorded about 10 200 events during this first large scale injection, the surface network helped to locate about 165 events with magnitude larger than 0.5. Unfortunately, for most of these events the uncertainty on location and the amount of clear polarity data does not provide for accurate focal mechanism determination. Helm [34] was able to determine 93 focal mechanisms based only on EOPGS network data, some of them with only six polarity data. By running an inversion of these focal mechanisms, following Rivera and Cisternas algorithm [42], he concluded that the largest principal stress is vertical and that the maximum horizontal principal stress is oriented N125°E, an orientation more than 45° off the results determined from borehole images.

Later, Gaucher et al. [43] reanalyzed a set of 14 focal mechanisms by combining Pwaves polarity from downhole and surface stations with polarity of Swaves from the downhole stations when they were clear. Some of these determinations are more than 30° off Helm's determination, and therefore this certainly explains part of the error in Helm's principal stress direction determination. These focal mechanisms are shown on figure 6.

They correspond to a mixture of normal and strike-slip events, consistent with a sub-equality between the maximum horizontal principal stress component and the vertical component. But Figure 6 also shows that some strike-slip events, although very well resolved (more than 15 polarity data), are not consistent with a North-South direction for the maximum horizontal principal stress. Given the very strong constraints on regional principal stress directions provided by borehole images, it is concluded that some of these shear events have occurred in zones of stress heterogeneity.

Various hypotheses have been formulated for explaining these sources of stress heterogeneity. On figure 6, we explore the possibility that the stress field has been altered by previous slip events, which occurred in the close neighbourhood of the corresponding event. It can be seen that one of the most heterogeneous strike-slip events (event 43128) occurred in a volume that had not been affected by any previous seismic slip. This suggests that the source of heterogeneity existed prior to the injection test, or that some previous aseismic slip has altered locally the stress field. This is discussed further in section 5.1. But it is concluded here that, unless some additional information is available, these 14 focal mechanisms alone may not be used for a local stress determination.

4.3 *Shear wave splitting analysis*

Laboratory work has shown that the Soultz granite is isotropic [44]. Yet, Gaucher et al. [43] were able to detect some shear wave splitting at two of the downhole stations (4550 and 4616). The third downhole station was not investigated for it has been shown to be associated with a local velocity anomaly consistent with the station being located within the sedimentary cover. Station 4550 is about 100 m below the sedimentary cover while station 4616 is only a few meters below the granite-sedimentary rock interface.

Shear wave splitting, namely the arrival of two shear waves, is associated with anisotropic properties of the rock. It is generally accepted that, for an isotropic rock matrix, this anisotropy is induced by the effect of the stress field on the opening of micro-fissures [45, 46]. Schematically, the principle is that micro-fissures oriented perpendicularly to the maximum principal stress are more closed than those which are perpendicular to the principal minimum stress. Hence velocity is faster in the direction of the maximum principal stress than in the direction of the minimum principal stress. When the three principal stress magnitudes are different, the rock mass exhibits three axis of symmetry (9 constants of elasticity) but when two principal stress magnitudes are equal, the material exhibits planar isotropy with only 5 constants of elasticity.

While the anisotropy may be very small (a few %), the picking of shear wave polarization provides means to identify shear wave splitting with good accuracy so that the orientation of the fastest propagation direction is detected fairly easily.

As shown on figure 7, the amount of ray path directions sampled is very satisfactory. Given that it takes a few wave lengths for splitting to occur, and that the typical wave lengths are in the 10 to 20 meters range, these results are consistent with a principal stress direction parallel with the N-S orientation, for a sphere centred on the seismic station, with a radius at least equal to 150 to 200 m. It also suggests sub equality between the maximum horizontal principal stress and the vertical stress (five constants of elasticity for the equivalent model).

5 **Proposed vertical stress profile and comparison with results from other regional deep boreholes**

We review in this section the various solutions that have been proposed to characterize the stress field at Soultz and present our synthetic model.

5.1 *Regional principal stress directions*

5.1.1 *Mean direction of the maximum horizontal principal stress*

Given the observed verticality of most induced tensile fractures in wells GPK1 and GPK2, it is concluded that indeed for most of the investigated volume the vertical direction is a principal direction. However, as pointed out by Brudy and Zoback [26], very locally, these tensile fractures are inclined and form en echelon patterns, thus indicating local variations in principal stress orientation since the boreholes remain vertical (less than 5 ° variations in verticality). Hence only the orientation of the maximum horizontal principal stress direction is to be ascertained.

We summarize in table 4 results from our bibliographical review on this issue. Results vary from N125°E to N185°E. Taking the central value of this interval would lead to conclude to a N155° E orientation, i.e. the direction of the seismic cloud orientation observed below 3000 m, about 30° off that observed around 2900 m. Hence it is essential to take a closer look at these results for a proper interpretation of the microseismic cloud development and its relationship with equilibrium conditions.

A first observation is that all mean values, except for two, fit within the interval N164°E to 185°E. The only values that do not fall into this interval are Helm's results from the focal mechanisms inversion and one of the options of Rummel and Baumgartner's HTPF determination. But it has been shown that Helm's determination of focal mechanisms from EOPGS network may be as much as 30° off results obtained when all available data are considered (CSMA and EOPGS). Further, some focal mechanisms are clearly not consistent with the general results from borehole images and it will be shown in the next section that this may be simply explained by local stress heterogeneity associated with preexisting fractures. Hence, at this point, this result (N125°E) is simply not considered to be reliable. Similarly, the result from HTPF inversion is not considered to be valid for it involves a 5 parameter model for only 5 HTPF data. Clearly, any error on the data will have drastic consequences on the result. Given that Klee and Rummel [15] statement on stress orientation is based on the same results as Rummel and Baumgartner's paper[14] (no new data on stress orientation are provided, only results on stress magnitudes), it is concluded that the two values N125°E and N155°E must be abandoned.

Prior to any further analysis, one is led to observe that all remaining mean values fall within the N 175±10° interval. However all values do not carry the same weight. Further, mean values are associated with domains of uncertainties. When this is taken into consideration, all data on the maximum horizontal principal stress orientation fall into the broader N 175±30° interval. A question arises as to whether this apparent large dispersion is really meaningful when it comes to the analysis of the development of failure in the rock mass. This is further discussed in the next section

5.1.2 *Scale of stress heterogeneity*

A closer look at the borehole cross-section elongation orientation profile provides some insight on the size of zones where stress heterogeneity are observed. On figure 8, an attempt has been made at evaluating the length of borehole for which deviation from the mean direction was observed. The orientation profile has been filtered off its shorter wavelengths, i.e. variations occurring along a depth range smaller than the cut-off wavelength have been rejected. On the lower graph of figure 8, the value of the standard deviation obtained for the various filtered profiles are indicated. The result shows that for events with size as large as 1 meter, the standard deviation is 15°, but as wavelength gets longer and longer, the standard deviation decreases. For depth ranges longer than 100 m; the standard deviation gets smaller than 5 °.

As can be seen on figures 5 and 8, the departure from the mean direction is not evenly distributed with respect to the mean but rather exhibits some secondary extrema, most of which are located to the west of the mean value.

This may partly explain why the solution derived from the inversion of focal mechanisms is biased to the west of the central value estimated from borehole images. Indeed, if errors on focal solutions were evenly distributed, then the result should only be less well constrained, and not strongly biased. It is proposed here that, during injection, water percolates in fracture zones with the largest hydraulic conductivity, i.e. fractures that contain the largest channels. These channels are sources of local stress heterogeneity and therefore microseismic events have a stronger chance to sample zones of stress heterogeneity than zones of uniform stress. If some bias affects these sources of heterogeneity, it will also affect the focal plane inversion. Given the above statistical results, zones of stress heterogeneity are limited in spatial extension so that seismic events with a source radius larger than 20 meters are likely to sample properly the regional stress field. But for the seismicity observed during this first large scale injection, the size of sources fall in the meter range (from 0.5 to 15 m), hence the difficulty to sample the natural stress field with these small events.

5.1.3 *Proposed solution and comparison with other regional deep stress determinations*

Results described here above indicate that the rock mass may be considered grossly homogeneous for volumes larger than a few tens of meters. Yet for such rock volumes, the principal stress directions will still vary by as much as 20°, depending on location (with a Gaussian law and a 5° standard deviation, the 99% confidence level for the solution remains within ± 15°). But if one considers volumes of the order of 800 x 800 x 800 m, results suggest that variations become negligible. However, this lack of variation reflects only the limited length of the profile for which the analysis has been undertaken.

One may observe that the mean value obtained from tensile induced fractures between 1500 and 2600 m is 169° (identical to the peak value of the thermal elongation orientations). The mean directions obtained between 2000 and 3590 m (also from drilling induced tensile fractures) is 181° and that derived from compressive borehole breakouts between 3020 and 3800 is equal to 185°. Hence these results may suggest a progressive rotation of the maximum horizontal principal stress with depth, from N165°E near 1600 m to N185°E near 3800 m.

These orientations may be compared to results obtained at the KTB site in Germany, some 300 km to the East of Soultz [26]. Drilling induced fractures are reported in the direction N 154°±17° from 3000 to 4000 m, while hydraulic fracture tests have yielded a mean orientation of 149±15° down to depth of 3000 m. Then the mean orientation of drilling induced fractures from 3000 to 6000 m is reported to lie in the N166 ± 17°E direction. Finally measurements at 7000 m yield a N 182 ± 21°E direction while those at 7800 yield N 177 ± 11°E. Interestingly, the orientation of compression breakouts are reported to vary from 149 ± 18°N in the upper part of the well to N 171 ± 17°N around 8000m.

Also of interest are results from Bad Urach, some 120 km to the South East of Soultz. Indeed Heinemann et al. [47] and Tenzer et al. [48] report a N 172 ± 7°E mean direction for the mean horizontal principal stress direction as determined from breakouts analysis observed between 1900 m and 3500 m.

It is concluded here that the orientation of the maximum horizontal principal stress measured below 3000 m in crystalline rocks at Soultz, Bad Urach and KTB site is N 170 ±15°, i.e. about 30° north to the mean orientation (N145±26°) proposed for northwestern Europe [49]. However the tendency for a rotation toward the north direction, as depth increases, remains to be ascertained before it is generalized to northwestern Europe.

5.2 *Magnitude of principal stress components*

No direct measurement of the vertical stress component has been obtained. Given that the vertical direction has been shown to be principal over most of the depth of interest and given the large scale rock homogeneity, this component is evaluated from the integrated density value [24]. Given the upper 1377 m of sediments at the GPK2 wellhead, the vertical stress component is estimated according to equation (2c) :

$$Sv = 33.8 + 0.0255\ (z - 1377) \qquad (2c)$$

5.2.1 *Evaluation of the minimum horizontal principal stress component*

Various alternatives may be considered for evaluating the minimum horizontal principal stress at various depths. Two data are considered to be constraining very efficiently the minimum principal stress: the small scale hydraulic reconnaissance test by Jung [16] at 1980 m and the large scale hydraulic test at incremental flow rates run in September 1993.

We have not considered early shut-in measurements obtained for the sake of stress measurement, for most of them have been conducted at depths where later work has shown the existence of pervasive drilling induced fractures. These fractures are likely to have influenced the pressure response of small scale tests and this may explain why systematically low values, close to the hydrostatic pressure, have been measured for such tests.

As already stated, the hydraulic test run by Jung is known to have created a fracture oriented parallel to the minimum principal stress direction as defined here above. Both the shut in pressure and the reopening pressure yield very similar values and the mean, namely 26.3 MPa, is taken as the magnitude of the minimum principal stress around 1980 m.

Given equation (2c), at 1980 m the ratio between the minimum horizontal principal stress magnitude S_h and the vertical component S_v is found to be equal to :

$$\text{Near 1980 m} : S_h / S_v = 0.535. \qquad (3)$$

For the large scale hydraulic test run in the openhole section of GPK1, between 2850 m and 3400 m, the pressure stabilized at 10.5 MPa , independently of flow rate above 24 l/s. Further the location of induced microseismicity between 2800 m and 2900 m is oriented parallel to the minimum principal stress direction. In addition, once the pressure stabilizes, microseismicity is observed to migrate upward, as expected from a true hydraulic fracture when the fluid density is smaller than the vertical gradient of the minimum principal stress.

Also, for this test, flow (spinner) logs run during the injection at the end of testing, when the well head pressure had stabilized at 10.5 MPa, show that 40 % of the flow left the well between 2850 m (the casing shoe) and 2900 m [19, 50]. However, the flow lost within this borehole section had dropped to less than 20 % of total flow rate at the end of the 18 l/sec sequence. Hence the stabilization of injection pressure corresponds with a drastic decrease of flow impedance in this upper section of the well, i.e. where the seismic cloud is N-S oriented. It is considered that this drop in flow impedance is associated with the mechanical opening of fractures and this supports the proposition that the stabilized injection pressure yields a very close estimate of the minimum principal stress magnitude, around 2900 m.

A question may arise as to the possible effect of thermal cooling on this stress magnitude evaluation. However, only if the open-section of the fracture remains within 5 to 10 meters of the wellbore would thermal stresses be significant and induce a decrease of a few MegaPascal for the normal stress to the fracture [28]. This short length is not consistent with the 14 l/s flow rate that was flowing in the formation through this fracture system, nor is it consistent with the NS extension length of the seismic cloud, at this depth. It is concluded that thermal stresses are not influencing the stabilized pressure.

Hence, results from this large scale injection test are consistent with a minimum principal stress magnitude equal to about 39.5 MPa for the 2850 m to 2900 m depth interval, which yields :

$$\text{Near } 2880 \text{ m}, \; Sh/Sv = 0.548 \qquad (4)$$

Given that very few tensile induced fractures have been observed below 2900 m, we may assume that the Klee and Rummel 's aluminium packer test at 3315 m [15] has been representative of the minimum principal stress magnitude given the observed induced vertical fracture parallel to the minimum principal stress. Hence at 3315 m, the minimum principal stress is taken equal to 45 MPa which yields :

$$\text{Near } 3315 \text{ m}, \; Sh/Sv = 0.541 \qquad (5)$$

The other aluminium packer test run in GPK1 at 3506 is not considered for the stress determination since the observed induced fracture is oriented at 90° from the regional maximum horizontal principal stress. This led us [51] to propose to evaluate the minimum principal stress from the vertical component at the same depth by the simple relation :

$$S_h = 0.54\, S_v = 0.54\, [33.8 + 0.0255\, (z - 1377)] \qquad (6)$$

Later, during summer 2003, a stimulation test was run in well GPK3 in the uncased section of the deviated well between 4547 m and the bottom of the well at 5091 m [13]. During this test, the pressure stabilized even though the injection flow rate increased progressively from 50 l/s to 70 l/s, through combined injection in both wells GPK3 and GPK2. Further, once the pressure stabilized, an upward migration of sismicity was observed, consistent with the mechanics of hydraulic fracturing. Let us mention here that at the end of this test, during shut-in, two magnitude 2.9 events were recorded.

The stabilized pressure was observed at 16.2 MPa wellhead pressure, so that the ratio between the minimum principal stress magnitude and the vertical stress around 4550 m is found to be :

$$\text{Near } 4550 \text{ m}, \; Sh/Sv = 0.537 \qquad (7)$$

If indeed the stabilized injection pressure equals the minimum principal stress magnitude, then equation (6) provides an estimate less than 1% off the observed value.... Hence this solution is adopted for the discussion on the failure criterion proposed in the next section.

5.2.2 *Evaluation of the maximum horizontal principal stress component*

Various alternative methods have been considered for evaluating the magnitude of the maximum horizontal principal stress. They either refer to failure processes at the borehole wall (depth at which drilling induced thermal tensile fractures stop appearing, width of compressive borehole breakouts, breakdown pressure observed during straddle packer hydraulic fracturing tests), or to interpretation of slip motions observed for microseismic events.

As discussed in section 4.2, some of the microseismic events have been shown to be associated with zones of stress heterogeneity. Hence, given the absence of a simple criterion for selecting so called homogeneous mechanisms, this data has not been considered individually.

Similarly, the fact that compression breakouts clearly depend on time demonstrates the necessity to take into account time effects on the failure process for evaluating S_H magnitude. But no data with this respect is yet available. And this applies also to tensile fractures. Applying correction factors to standard laboratory tests for taking into account stress corrosion effects, would result in uncertainties equal to or greater than 20 %, given that time effects may alter strength parameters by as much as 100 %, not mentioning the uncertainty associated with a proper accounting for pore pressure effects [28].

This uncertainty range is not smaller than that affecting the evaluation of the relative value of S_H with respect to that of S_V that can be retrieved from simple considerations on both induced and natural focal mechanisms. Indeed, for both sets of data a mixture of normal and strike slip events are observed [34]. This is consistent with sub-equality between the maximum horizontal principal stress and the vertical stress. This sub-equality is also consistent with results from shear wave splitting that support a five constant elastic model, i.e. equality between two principal stress magnitudes so that the equivalent material is transversally isotropic rather than orthotropic (9 constant of elasticity with three axis of symmetry).

Further, as will be discussed in the next section, large scale failure processes have been induced by the September 1993 water injection. The geometry of the fresh fracture zones has been estimated from the location of induced seismicity. As shown in table 3, the seismic cloud is inclined 23° to the vertical direction between 2900 m and 3000 m, but it is vertical within the 3000 m - 3200 m depth range. This is consistent with S_V being the largest principal stress between 2900 m and 3000m, and S_H being the largest principal stress between 3000 and 3200 m. But, the seismic cloud that was generated in 1994 when injecting water around 2000 m is found also to be vertical and parallel to that generated below 3000 m, in 1993. This is consistent with S_H being the maximum principal stress around 2000 m.

Given the characteristics of stress heterogeneity observed from borehole images, we propose bounding the domain of solutions for S_H as follows:

$$\text{Within the 2800 m and 3600 m depth range: } 0.95\ S_V \leq S_H \leq 1.1\ S_V \qquad (8)$$

Given that, at seismogenic depth a slight dominance of strike slip events is observed over normal events, equation (8) is anticipated to remain valid down to 8 to 10 km.

6 Determination of a failure criterion for the granite rock mass and discussion.

In this section we analyze the development of induced seismicity as observed during the September 1993 experiment, taking into consideration the regional stress field as defined here above. First the growth of the microseismic cloud is presented, then a failure criterion is proposed for the 1500 - 3600 m depth range and finally parameters controlling stress variation with depth, at Soultz, are discussed.

6.1 *Growth of the seismic cloud during the September 1993 hydraulic test.*

As shown on figure 3, three phases may be separated during the injection test :

i. Phase 1, when the injection wellhead pressure remains smaller than 4 MPa and does not yield any observable microseismic activity;
ii. Phase 2 when the wellhead pressure varies from 4 MPa to 9 MPa and induces an axisymetrical growth of the seismic cloud;
iii. Phase 3 when wellhead pressure gets larger than 9 MPa and leads to a planar growth of the microseismic cloud.

This result is somehow reminiscent of laboratory triaxial tests in which the acoustic activity is recorded while the axial load is progressively increased [52, 53, 54]. These laboratory tests show that while acoustic emissions are randomly distributed within the specimen as long as the load remains below the elastic limit of the material, they progressively localize within a narrow band that becomes the fault plane when failure is reached.

Following this phenomenology, it is proposed that during Phase 2 the rock remains within the elastic domain while only in Phase 3 does macroscopic failure initiates, i.e induced seismicity localizes within a planar structure. Shapiro et al. [55] have proposed to link the velocity of the growth of the microseismic cloud induced by fluid injection to the hydraulic diffusivity of the rock mass. Clearly this seismic cloud growth velocity is associated with the intact rock mass diffusivity only in Phase 2, before failure localizes [56].

A somewhat similar localization process was observed during laboratory hydrofracture tests in Weber sandstone run by Lockner and Byerlee [57]. Two samples were subjected to 100 MPa confining pressure and 400 MPa axial load. Acoustic emissions were recorded while water was injected at the center of the specimens at different flow rates. When flow rate was very slow, acoustic emission outlined the progressive formation of a shear plane, according to the effective stress principle. But when flow rate was fast, acoustic emission outlined the growth of a tensile fracture. Additional tests showed that either tensile or shear failure would occur depending on the injection rate, i.e. depending on the pore pressure distribution within the sample.

During Phase 3, for the 2800 m to 2900 m depth interval it has already been argued that the microseismic cloud has outlined a hydraulic fracture. But below 2900 m, the localization of induced seismicity within a planar structure is taken as the signature of the formation of a new fault plane out of preexisting, smaller scale, fractures and flaws.

The orientation of these freshly formed fault planes may be taken to advantage for determining the large scale failure criterion for the rock mass, given that the stress field has been completely determined.

6.2 *Determination of a failure criterion*

Let us first assume that the rock mass is just at equilibrium so that the effective stress field satisfies friction equilibrium conditions (Byerlee's law with friction coefficient somewhere between 0.6 and 1.0). Then, the apparent friction coefficient for the rock mass is given by the tangent to the Mohr circle derived from effective stresses, with the assumption of hydrostatic pressure conditions. In the absence of any cohesion, the friction angle is :

$$\varphi = \mathrm{arctg}\ [(1 / (a^2-1)]^{1/2}, \text{ with } a = (\sigma_1+\sigma_3-2P_f)/(\sigma_1-\sigma_3) \qquad (9)$$

where σ_1 and σ_3 are respectively the maximum and the minimum principal stress and P_f is the formation pore pressure. At Soultz, it is given by (Evans, 1996) :

$$P_f = 0.9 + 0.0098\ z \qquad (10)$$

where z is depth in meters and P_f is in Megapascal.

The friction angle is found to be 39° (friction coefficient equal to 0.81) so that the optimally oriented slip plane makes a 25.5° angle with respect to the maximum principal stress orientation.

If indeed, the granite rock mass is just at equilibrium, then the slightest pore pressure perturbation should induce slip along a well identified slip plane. Given the sub-equality between the vertical and the maximum horizontal stress at Soultz, this should result in the following slip directions :

If S_v is the maximum principal stress; the induced slip plane is oriented N170±10° and is inclined 25° with respect to the vertical direction;

If S_H is the maximum principal stress; the induced slip plane is vertical and oriented ± 25° with respect to the N 170±10° S_H direction (i.e. N 135 to 155°, or N190° to N210°).

Interestingly, both of these orientations are amazingly close to the mean microseismic cloud orientations given in table 3, assuming S_v is the maximum principal stress at 2900 m (consistent with the seismic cloud being oriented N 165°, i.e. sub parallel to S_H direction, and inclined 23° with respect to the vertical direction) but that it is S_H that is the maximum principal stress below 3200 m (consistent with the cloud being vertical and oriented 24 ° off the S_H direction taken equal to 170°).

Differences between expected and observed orientation remain well within the domain of uncertainty. However, as shown on figure 3, it is only when the wellhead pressure reaches somewhere from 8 to 9 Mpa that the microseismic cloud becomes planar and corresponds to a failure process.

A detailed analysis of borehole images taken before and after the large scale injection test [35], demonstrates that no large scale pre-existing plane existed prior to the injection, within the depth range where the seismic cloud has intersected the borehole. Instead, as shown by the analysis of multiplets [36], slip has occurred on multiple small scale pre-existing fractures that have linked together into a macroscopic structure. Multiplets are interpreted as the recurrent slip along asperities created by the breaking of "bridges" that linked one pre-existing fracture to another. This leads us to propose that cohesion plays an important role in the stability of this granite. This cohesion may be estimated from an evaluation of the pore pressure required to initiate macroscopic failure.

Following Shapiro et al. [53], the large scale hydraulic diffusivity of the granite rock mass is evaluated from the original velocity of the microseismic cloud growth, when the wellhead pressure remains smaller than 9 MPa (phase 2). This yields a rock mass hydraulic diffusivity equal to 5 10^{-2} m^2/s, so that, after 5 days of fresh water injection and at 22 m from the wellbore, the overpressure is about 0.4 times that applied at the borehole wall.

Hence, after 5 days of pumping, the over pressure is about 3.5 MPa, at some 20 m from the wellbore wall, after correction for buoyancy effects associated with the difference in density between injected fresh water and the brine that fills the pore space. But after 5 days, failure starts developing and the hydraulic diffusivity increases. Given that a 3 to 4 MPa overpressure is required to initiate induced seismicity, it is safe to consider that 3.5 MPa is an underestimate of the pore pressure at failure, i.e. when induced seismicity starts developing within a narrow planar band.

With a 3.5 MPa overpressure and a 0.81 friction coefficient, the cohesion required to keep the rock mass from failing is found to be equal to 3.6 MPa for the failure zone identified between 2900 and 3000 m and 3.4 MPa for that identified below 3200 m.

In June 1994, the well GPK1 was let to produce and the produced brine was re-injected in the open-hole section of well EPS1, between 1990 and 2210 m. A total volume of 6 200 m^3 was injected at flow rates ranging from 5 to 10 l/s. This injection generated some induced seismicity that localized within a planar structure with mean azimuth N147° and a dip equal to 87°. During this test the well head pressure was raised progressively to 5.7 MPa. The development of this rupture process may be confronted to results already obtained.

Given that the slip zone is vertical, i.e. parallel to a principal stress direction, the failing zone is consistent with a fresh planar fracturing process, inclined 23° to the maximum stress direction (S_H direction taken equal to 170°), i.e. the same value as the seismic clouds observed below 2900m. A 23° inclination between the failure plane and the principal stress direction is consistent with a 44° friction angle, or a 0.96 friction coefficient. Then a cohesion of the order of 2.5 MPa is necessary for being consistent with an increase of 3 MPa for the pore pressure value.

In summary, the development of shear failure as outlined by induced seismicity may be explained with two different mechanisms :

> Hypothesis 1 : Increase in pore pressure induces shear on favourably oriented pre-existing weakness planes, the shear resistance of which satisfies the classical Coulomb friction law. At Soultz, it is characterized by a 0.81 friction coefficient (39° friction angle). But it is necessary to introduce a cohesion ranging from 2 to 4 MPa in order to keep the mass at equilibrium, depending on hypothesis on pore pressure diffusion.
>
> Hypothesis 2 : Increase in pore pressure generates fresh fracture surfaces that take advantage of smaller scale pre-existing planes. The orientation of the macroscopic planar structures identified from induced seismicity location fit a Coulomb failure criterion with a 44° intrinsic friction angle (0.96 friction coefficient) and a 2 to 3 MPa cohesion.

Both models are well within the uncertainty on observations. In fact, given that a cohesion must be introduced to fit the pore pressure required to initiate failure, many such models may be proposed. But phenomenological arguments are quite in support of the fresh fracture hypothesis.

First, and most importantly, pre-injection borehole imaging logs outline the absence of a clear pre-existing fracture zone around 2900 m. The localized shear zone identified by the relocation of multiplets fits observations on the post injection borehole imaging log. These show a multiplicity of fractures that have sustained some shear motion, as determined from changes in borehole geometry outlined by the Ultra Sonic Imager (UBI) arrival time data [35].

Second, all seismically active shear zones are found to be parallel to the intermediate principal stress direction and inclined 23 to 24° with respect to the maximum principal stress direction, provided Sv is indeed the maximum principal stress around 2900 m.

Hence, within the 1500-3500 m depth interval, the onset of shear failure process may be characterized by a simple Coulomb failure criterion defined as:

$$\tau = (\sigma_n - P_f)\, tg\,(44°) + (3\pm1) \qquad (11)$$

More significantly, whatever the mechanisms at failure, a 3 to 4 MPa increase in pore pressure was necessary to induce failure. It is concluded that, before water injection, the regional stress field was below the equilibrium conditions so that it is not clear why its variation with depth should satisfy a friction law.

This deep field experiment is quite similar to the Rangely (Colorado) experiment [58] that analysed conditions in which pore pressure increments may induce seismicity. Interestingly, in Rangely, a nearly 50 % increase in pore pressure was required to induce seismicity (from 17. MPa in the original conditions to 27.5 MPa when induced microseismic activity was the strongest). It is concluded that, for this site, the natural stress and pore pressure conditions are such that the Weber sandstone formation is not close presently to equilibrium conditions. However, in Rangely, microseismic events occurred along a well identified pre-exiting fault zone as opposed to the Soultz Granite in which new fault zones were created. Hence, while the loading conditions of pre-existing faults within the Weber sandstone formation are closer to failure conditions than is the intact rock mass, the opposite is observed for the Soultz granite.

6.3 *Discussion*

Before extensive stress measurements have become available, variations of stress magnitude with depth were often evaluated from the elastic solution of the deformation of an infinite half-space submitted only to gravity. With a Poisson's ratio ν for the rocks mass, it was shown that the two horizontal principal stress components were equal to $(\nu / (1-\nu) * S_{v.}$ Let us observe that had ν been taken equal to 0.38, the ratio between the minimum horizontal principal stresses and the vertical component would have been equal to 0.61. Interestingly, for a rock mass with a density of 2.6 g/cm3, a 0.61 ratio between the horizontal to the vertical stress magnitudes could be interpreted as well as a rock mass under frictional equilibrium with a 0.7 friction coefficient, i.e. precisely the value generally considered as characteristic of faults. Hence, we may propose mechanisms other than frictional equilibrium that may lead to linear stress variation with depth consistent with most observations.

The present results have demonstrated that the Soultz granite is not just at equilibrium. It takes 2 to 3 MPa pore pressure variations to induce microseismic activity and slightly larger values to reach the macroscopic failure of the rock mass. Further, it has been shown that, in both wells GPK1 and GPK2, some important fractures or faults are associated with local stress heterogeneity. But, more importantly, outside these zones of stress heterogeneity the principal stress directions remain stable. This is quite consistent with a continuum in which some limited slip motion occurs on a few isolated fractures, so that faults are associated with local stress heterogeneity out of which monotonic stress variations are observed.

Similar results have been published before, in particular for the 3.5 km deep Cajon pass borehole in granite, near the San Andreas Fault [59, 60], where multiple stress heterogeneities associated with local slip events have been reported but where a global steady trend is clearly identified outside the zones of stress heterogeneity. This has also been observed in the stable Le Mayet de Montagne granite formation in France down to 800 m [61, 62] where local stress heterogeneities have been shown to be consistent with the local, near complete, shear stress relief computed from an elastic solution.

All these results show that indeed faults and fractures do disturb locally the stress field, but that, at a larger scale, the rock mass behaves as a continuum rather than as a block assembly. In fact, block assembly models based on the geometry of major faults have been proposed for the Rhine graben [63]. These models show strong changes in principal stress directions from one bloc to the other, rotations that are not supported by observations.

Hence, it is proposed here that below a certain depth, the value of which depends on local site conditions, the variation of stress with depth is not related only to friction along pre-existing fractures but also, and possibly more importantly, to the rheological properties of the solid bridges that exist between the many fractures that have not completely healed. The modelling of observed linear variation with depth are likely to require much softer equivalent material than those derived from laboratory experiments or from seismic waves velocity. It is proposed that the observed "softness" results from a viscous relaxation mechanism, possibly associated with pressure solution.

The fact that rheological properties other than friction are controlling stress variation with depth is well established for sedimentary formation [e.g. 64, 65]. Present results demonstrate that this is also true for deep crystalline rocks.

7 Conclusions

Determining the complete stress field and its variations below 3000 m in the Soultz granite is a challenging endeavor, in particular because of temperature and stress corrosion effects. However, it has been shown that a combination of techniques may lead to fairly accurate constraints on the various components. Large hydraulic tests provide satisfactory evaluation of the minimum principal stress magnitude at specific depths (accuracy much better than 10%, given the fit obtained between observed and projected value at 4550 m) while borehole images yield information on the continuity and homogeneity of the principal stress orientation over much larger volumes (resolution of a few degrees). However borehole images analysis applies only in boreholes sections in which failure processes develop. With this respect tensile failure process (both micro and macro) induced by rock cooling has revealed very efficient.

The major challenge remains the determination of the maximum horizontal principal stress magnitude. When time, temperature and stress corrosion effects are better understood, analysis of observed failure processes could provide satisfactory constraints. Presently, it has been found that focal mechanisms, considered globally, together with results from shear wave splitting, provide also a strong constraint on the relative maximum horizontal principal stress magnitude with respect to the vertical stress component magnitude. Further, when focal mechanisms of larger events (with slip zones larger than 40 to 50 m) become available, they may help, statistically, to constrain more precisely this parameter.

It is concluded that, at Soultz, the vertical direction is a principal direction over most of the borehole length and that the maximum horizontal principal stress is oriented N 170 ± 15°, although possibly a rotation from 170° to 185° may occur between the upper part of the well (above 2500 m) and its lower sections (around 4 000 m). The minimum principal stress magnitude is found to vary linearly with depth, proportionately to the weight of overburden (Sh = 0.54 Sv). Finally, a sub-equality between the vertical and the maximum horizontal principal stress components is necessary to be consistent with the sub-equal number of strike slip and normal faulting events, with the observed shear wave splitting phenomenon, and with the orientation of freshly induced shear zones.

Injection of water in this medium involves three different processes. No induced seismicty has been observed as long as the increase in borehole pressure has remained smaller than 10% of the natural minimum principal stress magnitude (39.5 MPa at 2900 m). Axisymerical growth of the microseismic cloud has been observed as long as the borehole pressure increment has remained smaller than 20% of the natural minimum principal stress magnitude. Localized induced seismicity has been noted when the borehole pressure increment has become larger than 20% of the natural minimum principal stress magnitude, i.e. when the pore pressure increment away from the wellbore got larger than 8 % of the natural minimum principal stress magnitude.

Two geometries for failure localization have been observed : tensile fractures perpendicular to the minimum principal stress direction when the interstitial fluid pressure has reached the minimum principal stress magnitude. Shear failure when the pore pressure has remained smaller than the minimum principal stress magnitude.

This demonstrates that the rock mass was not close to failure prior to the fluid injections so that the observed linear variation with depth of the horizontal stress magnitudes is not linked to the sole frictional properties of pre-existing fractures. It involves in addition the rheological characteristics of the solid material. Hence, preexisting fractures are not viewed as a dense network leading to isolation of well defined blocks, but rather as local sources of stress heterogeneity embedded in an elastic, or more likely a visco-elastic material.

Acknowledgements

We would like to thank very sincerely S. Crouch and E. Detournay for organizing this special issue in honour of C. Fairhurst and for giving us the opportunity to present these results. Charles has always been most supportive in developing efficient and applying field-proof stress determination methods. We also thank A. Gérard, R. Baria and S. Michelet from the Soultz geothermal project, as well as R. Jones, formerly from CSMA, and R. Jung from NLBH for providing some of the data used in this work. However we are sole responsible for the ideas presented here.

References

[1] Fairhurst C., Stress estimation in rock : a brief history and review; Int. Jou. Rock Mech. Min. Sc.; 2003, 40 (7-8), 957-74.

[2] Fairhurst C. Methods of determining in situ rock stresses at great depth. Technical Report I-68 Missouri River Division, U.S. army corps of engineers; 1968

[3] Brace W.F. and D.L. Kohlstedt, Limits on Lithospheric Stress imposed by Laboratory Experiment; j. Geophys. Res. 85(B11) 6248-6252; 1980

[4] McGarr A. and N.C. Gay; State of stress in the Earth's crust, Ann. Rev. Earth Planet Sci., , 405-436; 1978

[5] Zoback M.D. and J.H. Healy; In situ Stress Measurements to 3.5 km Depth in the Cajon Pass Scientific research Borehole: Implications for the Mechanics of Crustal Faulting; j. Geophys. Res., 97(B4) 5039-5058; 1992

[6] Brudy M., M.D. Zoback, K. Fuchs, F. Rummel and J. Baumgärtner; Estimation of the complete stress tensor to 8 km depth in the KTB scientific drill holes: Implications for crustal strength, j.Geophys. res. 102(B8) 18453-18476, 1997

[7] Byerlee, J.D., Friction of Rocks; Pure and App. Geophys., 116, 615-626, 1978

[8] Toda S and R.S. Stein, Response of the San Andreas fault to the 1983 Coalinga-Nunez earthquahes: An application of interaction-based probabilities for Parkfield; J. Geophys. Res. 107(B6), ESE6, 2002.

[9] Kappelmayer, O., Gérard, A. , Schloemer, W. , Ferrandes, R., Rummel, F. & Y. Benderitter. 1991. European HDR project at Soultz-sous-Forêts: Genral presentation, *Geotherm. Sc. Tech.,* 2: 263-289

[10] Baria, R., J. Baumgärtner, A. Gérard and J. Garnish. 2000. The European HDR Programme : Main targets and results of the deepening of the well GPK2 to 5000 m; in *Proc. World geothermal Congr. 2000*: 3643-3652; Int. Geothermal Association

[11] Weidler R., A. Gérard, R. Baria, J. Baumgartner, R. Jung; Hydraulic and Macro-seismic results of a massive stimulation tests at 5 km depth at the European Hot Dry Rock test site Soultz, France; Proc. 27th workshop on Geothermal Reservoir Engineering, Stanford Univ., 2002

[12] Hetkamp T., J. Baumgartner, R. Baria, A. Gerard, T. Gandy, S. Michelet and D. Teza; Eletricity production from Hot Rocks; 29th workshop on Geothermal reservoir Engineering, Stanford Univ (http://geothermal.stanford.edu)., 2004.

[13] Michelet S., R. Baria, J. Baumgartner, A. Gerard, A. Oates, T. Hettkamp and D.Tezza; Seismic source parameter evaluation and its importance in the development of an HDR/EGS system, 29th workshop on Geothermal Reservoir Engineering, Stanford Univ (http://geothermal.stanford.edu)., 2004

[14] Rummel, F. & Baumgartner; J. 1991. Hydraulic fracturing stress measurements in the GPK-1 borehole, Soultz-sous-forêts; *Geotherm. Sc. &Tech.*, 3: 119-148.

[15] Klee G. & Rummel, F. ; 1993. Hydrofrac stress data for the European HDR research project test site Soultz-sous-forêts; *Int. J. Rock Mech. Min. Sc.*, 30: 973-976

[16] Jung, R. 1991. Hydraulic fracturing and hydraulic testing in the granitic section of borehole GPK1, Soultz-sous-Forêts *Geotherm. Sci.& Tech.*, 3:149-198

[17] Cornet, F.H. & Valette, B. 1984. In situ stress determination from hydraulic injection tests data, *J; Geophys. Res.* 89, 11 527-11 537.

[18] Rutqvist, J., Tsang, C.F. & Stephansson, O. 2000. Uncertainty in the maximum principal stress estimated from hydraulic fracturing measurements due to the presence of the induced fracture, *Int. J; Rock Mech. Min. Sc.*, 37, 107-120

[19] Cornet, F.H. & Jones, R. 1994. Field Evidence on the orientation of forced water flow with respect to the regional principal stress directions; in Nelson and Laubach (eds.), *Rock Mechanics - Models and Measurements:* 61-71, Rotterdam: Balkema.

[20] Jung, R., Willis-Richard, J., Nicholls, J., Bertozzi, A. and Heinemann, B. 1995. Evaluation of hydraulic tests at Soultz-sous-Forêts, European HDR sitz, in *Proceedings of the world geothermal congress 1995*, vol 4, 2671-2676, Int. Geothermal Ass.

[21] Jones, R.H., Beauce, A. , Jupe A., Fabriol, H. & Dyer; C. 1995 Imaging induced seismicity during the 1993 injection test at Soultz-sous-Forets; in Barbier (ed.) *World Geothermal Congress,* 2665-2669; Int. Geothermal Association;

[22] Baumgartner, J., Jung, R. Gérard, A., Baria, R. & Garnish, J. 1996. The European HDR project at Soultz-sous-Forêts : Stimulation of the second deep well and first circulation experiments; in *Proceedings 21st workshop Geothermal Reservoir Engineering, Stanford U.*, SGP-TR-151, pp 267-274.

[23] Baumgartner J and F. Rummel; Eperience with „Fracture Pressurisation tests" as a stress measuring technique in a jointed rock mass; Int.. Jou. Rock Mech. Min. Sc. & Geomechanics abst. 26(6), 661-672 1989

[24] Heinedman B.; Results of Scientific investigations at the HDR test site Soultz-sous-Forêts, Alsace (1987-1992); SOCOMINE report, 126 p, 1994

[25] Mastin, LG. & Heinemannn, B. 1988. Evaluation of the caliper and televiewer data from the Soultz well between 1400 m and 2000 m; *Internal report* to Geophysics Institute, univ. Karlsruhe.

[26] Brudy, M & Zoback, M.D. 1999. Drilling-induced tensile wall-fractures : Implications for determination of in situ stress orientation and magnitude; *Int. J. Rock Mech. Min. Sc.*, 36: 191-215

[27] Nagel R., Das Spannungsfeld in der Geothermiebohrung Soultz-sous-forêts abgeleitet aus vertikalen Strukturen in einer Tiefe von 1.9 bis 3.6 km ; Diploma thesis, Universität Karlsruhe; 1994

[28] Bérard, Th. & Cornet, F.H. 2003. Evidence of thermally-induced borehole cross-section elongation: a case study at Soultz, France; *Int. J. Rock Mech. Min. Sc.*, vol. 40, nb 7/8, pp 1121-1140.

[29] Genter, A. & Tenzer,H. 1995. Geological monitoring of GPK2-HDR borehole, 1420-3880 5Soultz-sous-Forêts, France), BRGM report R 38 629, Orléans, France.

[30] Hudson JA, Brown ET. Studying time dependent effects in failed rocks. In: 14th Symposium on Rock Mechanics, American Society of Civil Engineers, Pennsylvania State University, 1973. p. 25

[31] Kranz RL, Scholz Ch. Critical dilatant volume of rocks at the onset of tertiary creep. J Geophys Res 1977;82(30):4893–8.

[32] Houpert R. Le comportement à la rupture des roches. In: Proceedings of the 4th Congress of the International Society of Rock Mechanics, vol. 3, Montreux, 1979.pp. 115-121.

[33] Sano O., I. Ito and M. Terada; 1981; Influence of strain rate on dilatancy and strength of Oshima Granite under Uniaxial Compression; J. Geophys. Res., vol. 86, nb B10, pp 9299-9311

[34] Helm, J. A. 1996. Aléa sismique naturel et sismicité induite du projet géothermique européen RCS de Soultz-sous-Forêts ; Doctoral thesis, Univ. Louis Pasteur-EOPGS, Strasbourg

[35] Cornet, F.H., Helm,J., Poitrenaud, H. & Etchecopar, A. 1997. Seismic and aseismic slips induced by large scale fluid injections ; *Pure App. Geophys.*, 150, 563-543

[36] Bourouis S., Seismicité induite et comportement mécanique d'un massif granitique fracturé par injection d'eau ; application au site géothermique de Soultz-sous-forêts ; Thèse de doctorat ; Institut de Physique du Globe de Paris, 186p ; 2004

[37] Poupinet, G., W. L. Ellsworth, and J. Frechet, Monitoring velocity variations in the crust using earthquake doublets: An application to the Calaveras Fault, California, *J. Geophys. Res.,* **89,** 5719-5713, 1984.

[38] Nadeau, R., M. Antolik, P. A. Johnson, W. Foxall, and T.V. McEvilly, Seismological studies at Parkfield III: microearthquake clusters in the study of fault-zone dynamics, *Bull. Seism. Soc. Am.,* **84,** 247-163, 1994

[39] Philips W.S., L.S. House and M.C. Fehler; 1997, Detailed joint structure in a geothermal reservoir from studies of induced micro-earthquakes clusters, Jou. Geophys. Res., vol. 102, pp 11 745 - 11 763.

[40] Got J.L., J. Frechet and F.W. Klein; 1994; Deep fault plane geometry inferred from multiplet relative relocation beneath the south flank of Kilauea; J; Geophys. Res. Vol. 99, pp 15375-15386.

[41] Fehler M., L. House and H. Kaieda; 1987; Determining planes along which earthquakes occur : method and application to earthquakes accompanying hydraulic fracturing; Jou. Geophys. Res., vol. 92, pp 9407-9414.

[42] Rivera, L. & Cisternas, A. 1990. Stress tensor and fault population of earthquakes, *Bull. Seis. Soc. Am.* 80, 600-611.

[43] Gaucher E., Cornet, F.H & Bernard; P. 1998. Induced seismicity for fracture identification and stress determination; *EUROCK 98 – Rock Mechanics in Petroleum Engineering*; vol. 1: 545-554, SPE paper 47324.

[44] Rummel, F. 1991. Physical properties of borehole GPK1, *Geotherm. Sci.& Tech.* 3 199-216

[45] Crampin S., 1985, Evaluation of anisotropy by shear wave splitting, Geophysics,. 50, 142-152.

[46] Crampin, S. and Lowell, J.H. 1991. A decade of shear wave splitting in the earth crust : what does it mean ? *Geophys. J. Int.* 107, 387-407

[47] Heineman, B.B., Troschke, B. & Tenzer; H. 1992 Hydraulic investigation and stress evaluations at the HDR test site Urach III, Germany; *Geothermal Resources Council, Transactions,.* 16 : 425-431;

[48] Tenzer H., Budeus P.& Schellschmidt; R. 1992 Fracture analyses in Hot dry Rock drillholes at Soultz and Urach by Borehole Televiewer measurements; *Geothermal Resources Council, Transactions 16*: 317-321

[49] Müller B., M.L. Zoback, K. Fuchs, L. Mastin, S. Gregersen, N. Pavoni, O. Stephansson and C. Ljunggren; Regional Patterns of Tectonic Stress in Europe; J. Geophys. Res., 97(B8) 11783-11804, 1992

[50] Evans K.F.T., R.J. Kohl, and L. Rybach; Analysis of the hydraulic behaviour of the 3.5 km deep reservoir during the 1995-1997 test series, and other contributions to the European Hot Dry Rock project, Soultz-sous-forêts, France, Final report to the Swiss Department of Education and science, BBW 95.0673-2, Swiss Federal Institute of Technology, July 1998.

[51] Cornet F.H. and Th. Berard; A case example of integrated stress profile evaluation; in Rock Stress (Sugawara, Obara and Sato ed.) 23-34; Balkema; 2003

[52] Scholtz C. H., Microfracturing and the Elastic Deformation of Rock in Compression, J. Geophys. Res. 73(4) 1417-1432; 1968

[53] Hallbauer D.K., H. Wagner and N.G.W. Cook., Some observations concerning the microscopic and mechnicazl behaviour of quartzite specimens in stiff, triaxial compression tests; Int. J. Rock Mech. Min. Sc. & Geomech. Abs., 10, 713-26; 1973

[54] Lockner D.A., J.D. Byerlee, V. Kuksenko, A. Ponomarev, A. Sidorin; Quasi-static Fault Growth and Shear Fracture Energy in Granite; Nature, 1991

[55] Shapiro S.A., E. Huenges and G. Borm;, Estimating the crust permeability from fluid injection induced seismic emission at the KTB site; *Geophys. J. Int.*, **131**, F15-F18; 1997

[56] Cornet, F H. Comments on “Large-scale *in situ* permeability tensor of rocks from induced microseismicity” by Shapiro, Audigane and Royer (1999); *Geophys. J. Int.;* 140, nb2: 465-469; 2000.

[57] Lockner D. and J.D. Byerlee; Hydrafracture in Weber Sandstone at High Confining Pressure and Differential Stress; J. Geophys. Res. 82(14), 2018-2026; 1977

[58] Raleigh C.B., J.H. Healy and J.D. Bredehoeft; Faulting and crustal stress at Rangely Colrazdo; in Floow and Fractue of rocks (Heard, Borg, Carter and Raleigh ed.), Geophysical monograph, 16, 275-284, Am. Geophys. Un., 1972

[59] Shamir G. and M.D. Zoback, Stress Orientation profile to 3.5 km depth Near the san Andreas Fault at Cajon Pass, California, J. Geophys. Res. 97(B4) 5059-5080; 1992

[60] Barton, C.A. and M.D. Zoback Stress perturbations associated with active faults penetrated by boreholes : possible evidence for near-complete stress drop and a new technique for stress magnitude measurement; J. Geophys. Res., 99(B5) 9373-9390, 1994.

[61] Scotti O. and F.H. Cornet; In situ evidence for fluid induced aseismic slip events along fault zones; Int. Jou. Rock Mech. Min. vol. 31., nb. 4, pp 347-358. 1994;

[62] Cornet F.H. and Jianmin Yin; Analysis of induced seismicity for stress field determination and pore pressure mapping; Pageoph, vol. 145, nb 3/4, pp 677-700; 1995

[63] Hosni A.; Modelisation par la méthode des Eléments distincts du champ de contraintes à l’échelle du Fossé Rhénan et de Soultz-sous-forêts ; Doctorat de l’Institut Polytechnique de Lorraine, Ecole des Mines, 1997

[64] Evans K.F., T. Engelder and R.A. Plumb ; Appalachian stress study 1. A detailed description of in situ stress variations in Devonian shales of the Appalachian Plateau; J. Geophys. Res. 94(B6), 7129-54; 1989

[65] Cornet F.H. and D. Burlet; Stress field determinations in France by hydraulic tests in boreholes; J; Geophys. Res., 97(B8), 11829-50; 1992

Table 1 . First Results from hydraulic tests for stress measurements [14]. Φ and θ are respectively the strike and the inclination to the vertical direction for the normal to the fracture planes. P_{si} is the shut-in pressure and P_r is the reopening pressure. Uncertainties are noted ε.

Depth (m)	Injected Vol. (l)	φ	ε_φ	θ	ε_θ	P_{si} MPa	ε_{Psi} MPa	P_r MPa
1 458	70	144	5	77	5	24.3/23.2	0.5	25.3
		166		90				
1 495	100	212	5	64	5	20.6	0.5	20.9
		162		70				
1 501	50	278	5	72	5	19.5	0.5	?
1 946	4000	226	5	63	5	29.4	0.7	?
1989	42000	165		90		25.3		
		150		78				

Table 2. Results from hydraulic tests with aluminum straddle packers [15]

Borehole Length (m)	P_{si} MPa	ε_{Psi} MPa	P_r MPa
EPS1-2195	26.6	0.5	29.6
EPS1-2205	27.0	0.5	24.3-28.1
GPK1-3315	45.0	0.5	49.0
GPK1-3506	44.5	0.7	46.0

Table 3 . Variation with depth of the main micro-seismic cloud orientations

Depth interval (m)l	Mean azimuth	Mean dip	Number of events
2800 - 2900	N179°E	87°	329
2900 – 3000	N165°E	67°	402
3000 - 3200	N146°E	86°	416

Table 4. Summary of the maximum horizontal stress orientation determinations that have been obtained at Soultz

Source of information	Well and Depth interval (m)	Mean direction	Uncertainty
Rummel and Baumgartner [14] HTPF method	GPK1; 1376 – 2000	N 155° Or N 176°	± 3° ± 6°
Klee and Rummel [15] from HF and HTPF data	GPK1 and EPS1; 1376-3500	NW-NNW (N135°-N157.5°)	
Jung, [16] Hydraulic fracture	GPK1; 1968-2000	N 170°	
Mastin and Heinemann [25] Drilling induced tensile fractures	GPK1; 1420 - 2000	N 169°	± 21°
Tenzer (1991), as reported by [26] Drilling indued tensile fractures	GPK1; 1450-2000	N 169°	± 11°
Heinemann [24] Hydraulic and drilling induced fractures	GPK1; 1420-2000	N 170°	
Nagel [27]) as reported by [26] Drilling induced tensile fractures	GPK1; 2000-3590	N 181°	± 22°
Cornet and Jones [19] Hydraulic fractures, thermal fractures induced by large scale injection, orientation of microseismic cloud	GPK1; 1900 - 3500	N 175°	
Genter and Tenzer [29]) Drilling induced tensile fractures	GPK2; 1420-3880	N175°	±17
Helm [34] focal mechanisms inversion	2300-3500	N125°	± 20
Gaucher et al. [43] Shear wave splitting	1350-1450	N180°	
Berard and Cornet [28] Thermal borehole cross-section elongation	GPK2; 1422 - 2700	N 164°	± 18
Berard and Cornet [28] compressive borehole breakouts	GPK1 and GPK2; 3020-3650	N 185°	± 7 from 3020 m to 3600m (GPK1); ± 25° from 3400 to 3650 (GPK2)

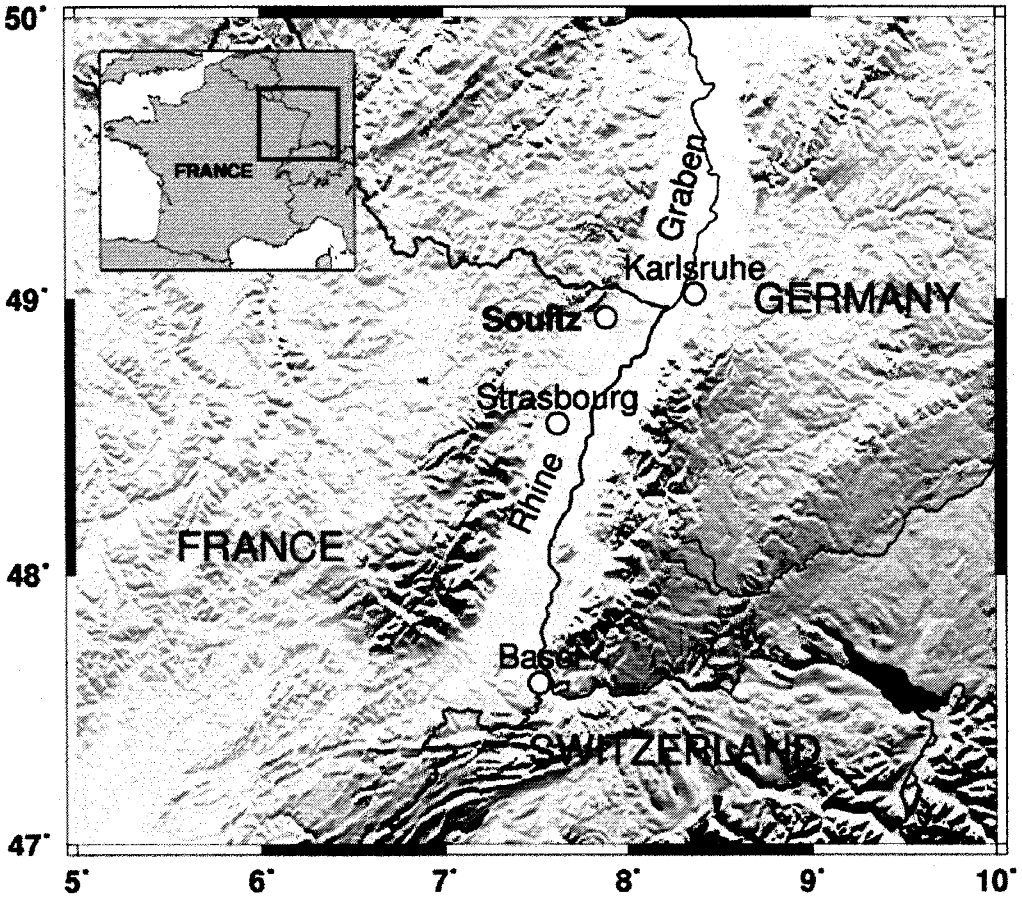

Figure 1 : Location of Soultz experimental Geothermal site.

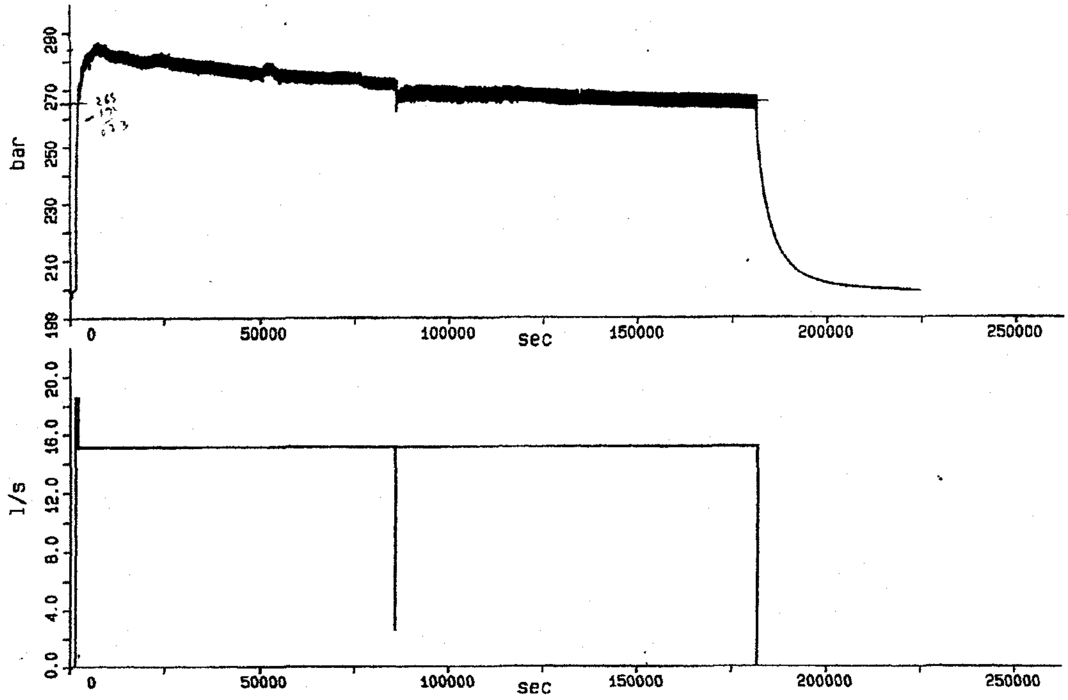

Figure 2 Hydraulic test (15 l/s injection rate) conducted in 1991, between 1972 m and 2000 m, in GPK1, after preliminary injections had already created vertical fractures (from Jung, [16]). The reopening pressure is considered to yield the minimum horizontal principal stress magnitude around 1980 m.

Figure 3: First large scale injection experiment in GPK1 [19, 20 and 21].The upper plot of the figure indicates the depth of microseismic events observed during injection. The lower plot shows horizontal projections of events observed above and below 3000 m, for flow rates smaller than 18 l/s and flow rates larger than 18 l/s. Location of well is indicated by a white dot.

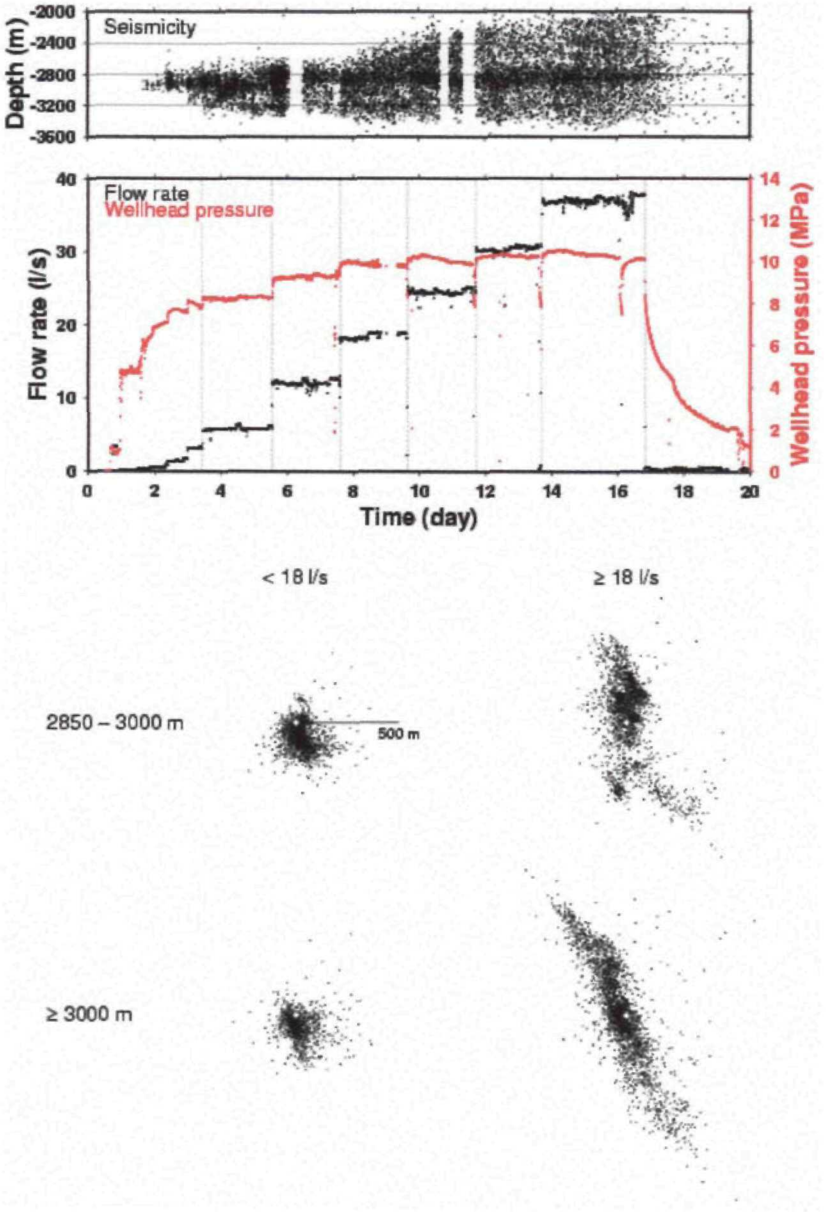

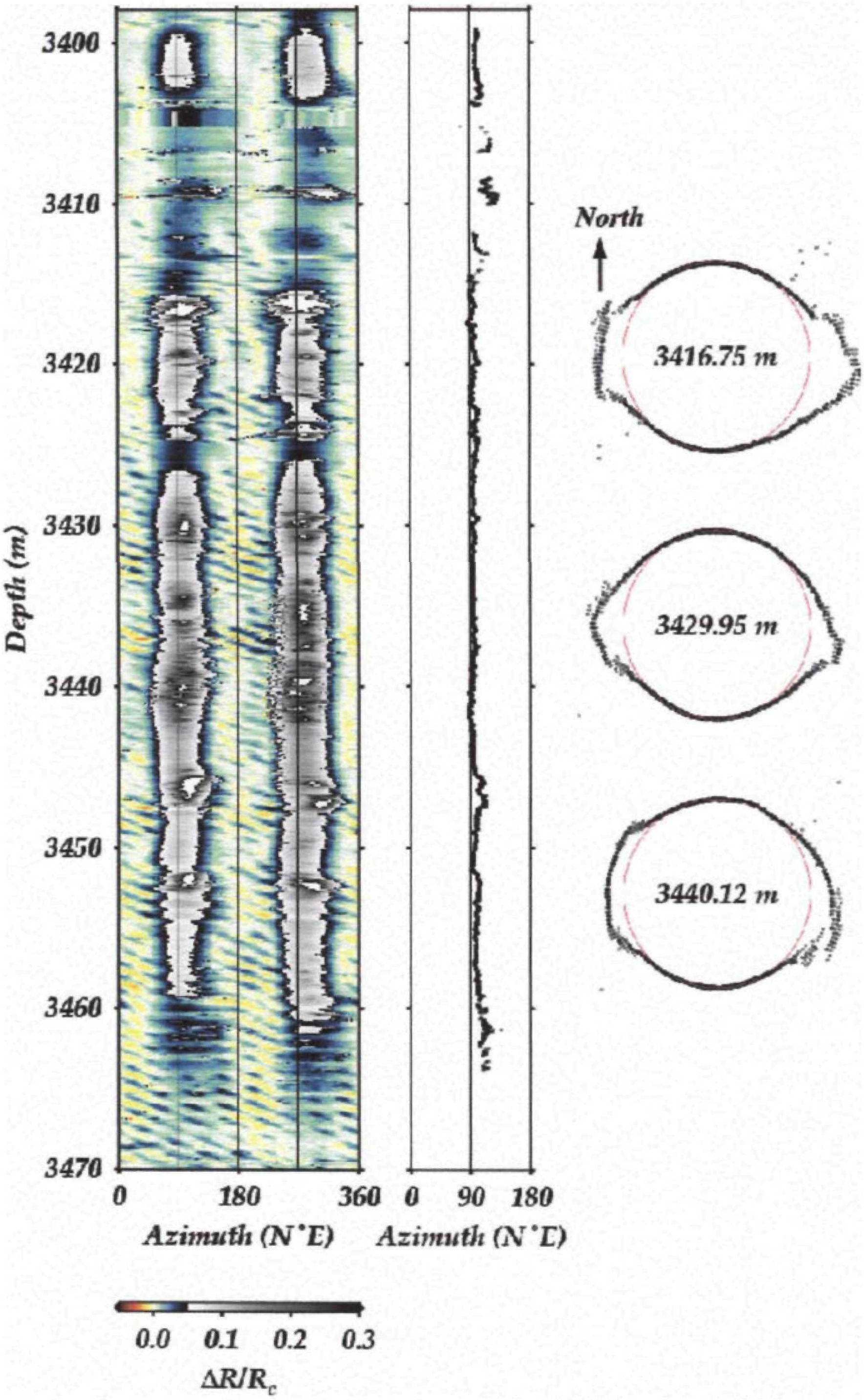

Figure 4. Example of compression breakouts observed in GPK1, around 3450 m.

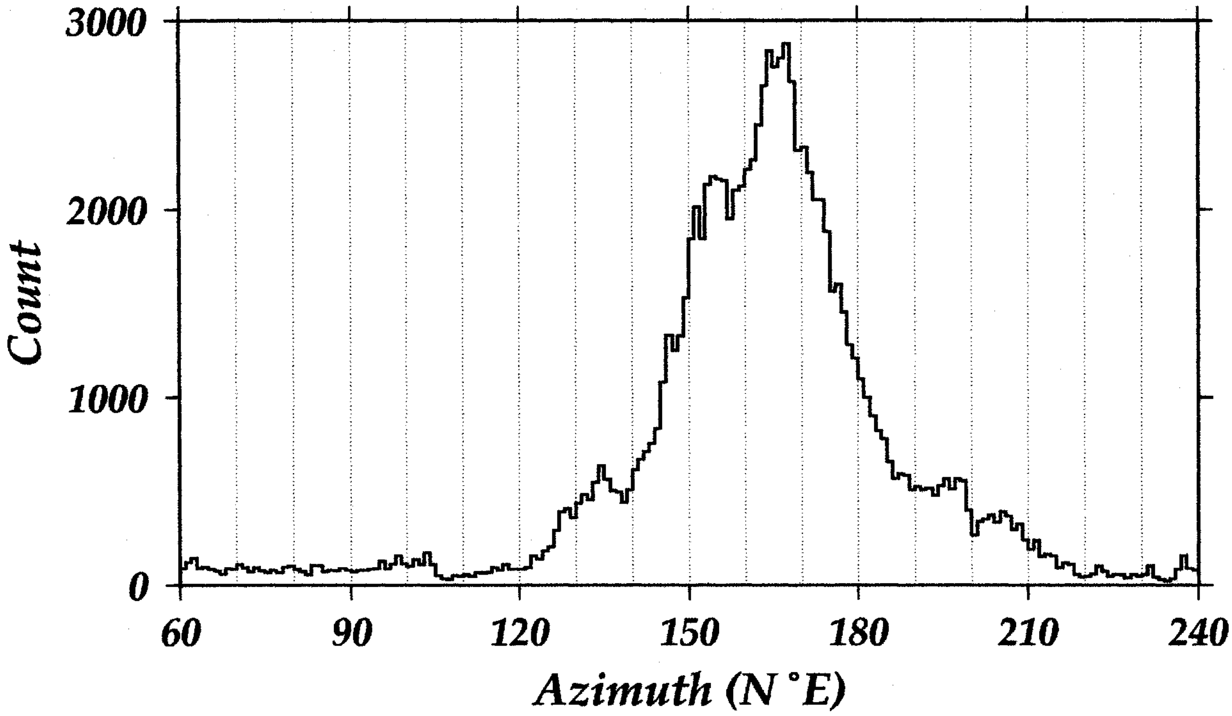

Figure 5 . Distribution of borehole cross-section elongations orientation for well GPK2, between 1.6 and 2.9 km.

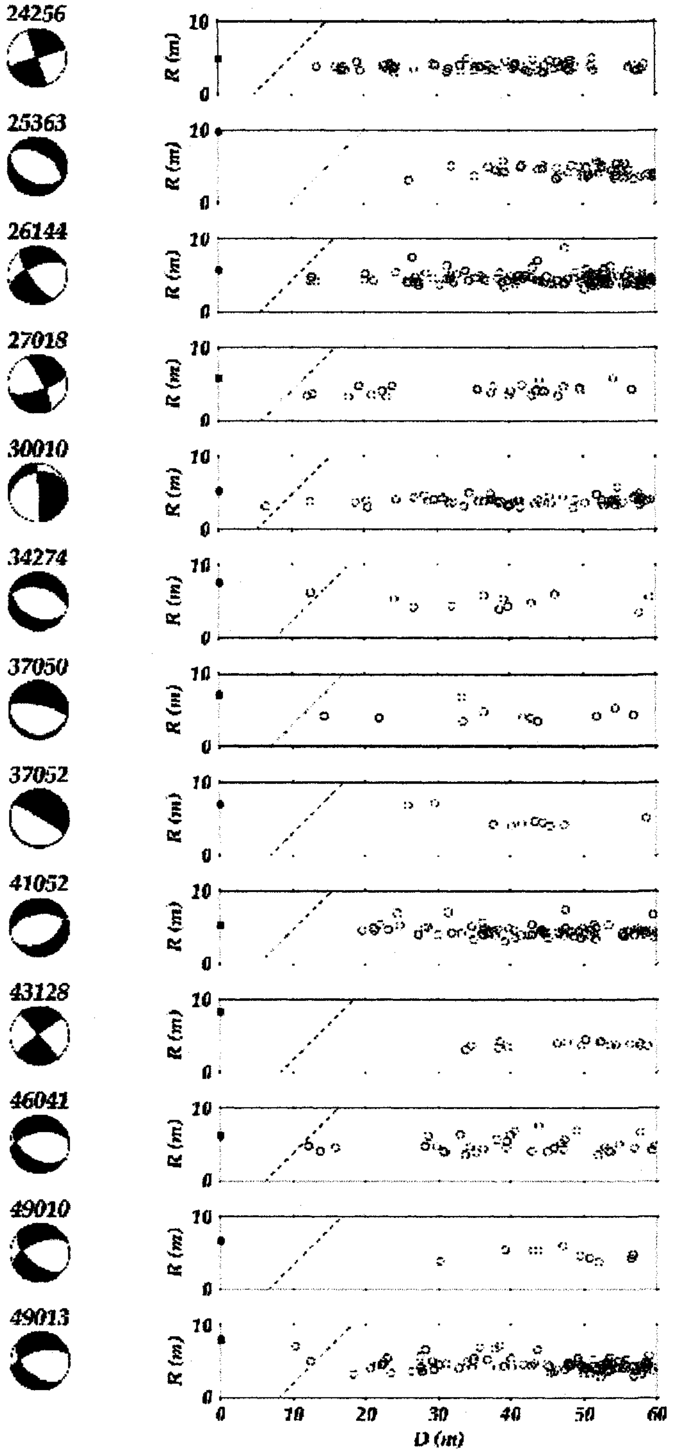

Figure 6 Focal mechanisms of events recorded on both the downhole and surface network. Also shown are distances to closest events that have occurred prior to the corresponding event.

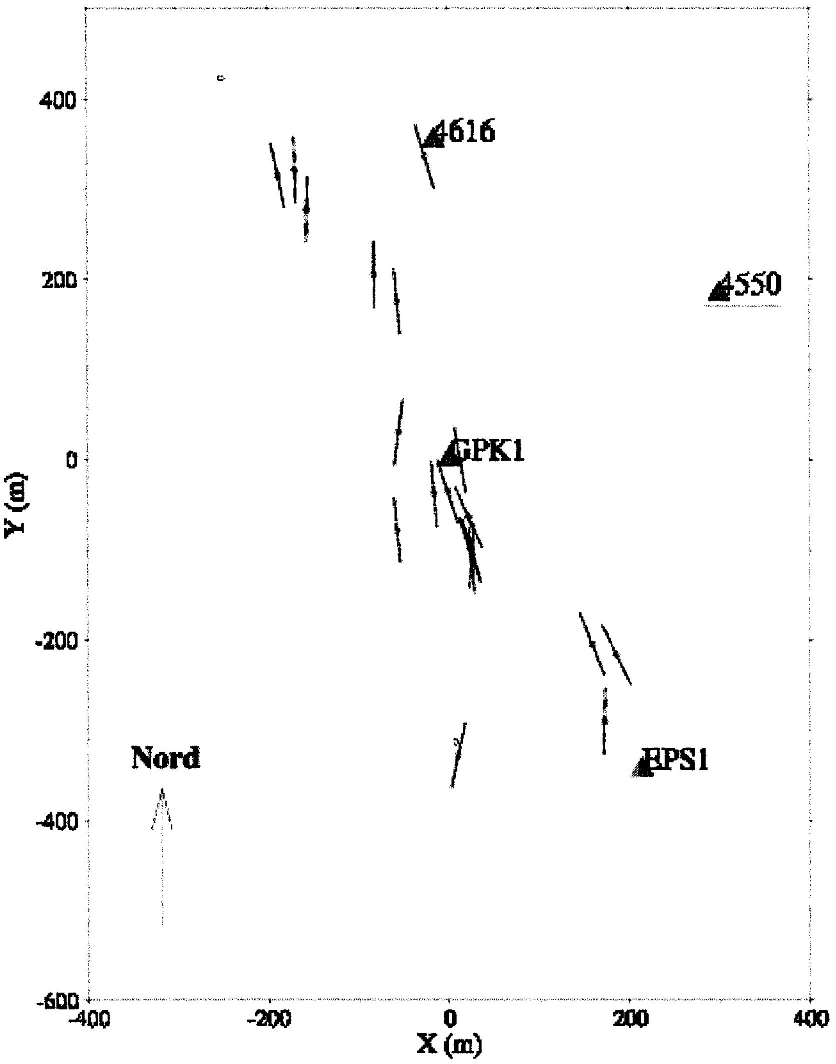

Figure 7 : Direction of fast shear wave propagation as detected on station 4550. X axis is oriented W-E while y axis is S-N. Station 4550 is the furthest to the East on the figure. The direction of polarization is shown at the source so as to illustrate the diversity of orientation for the ray paths [43]

Figure 8. Variation of the maximum horizontal stress orientation with depth. From left to right, the profiles have been filtered at longer and longer wave lengths (0.1 m to the extreme left and 100 m to the extreme right). The variation of standard deviation with the cut-off wave length is shown in the lower graph.

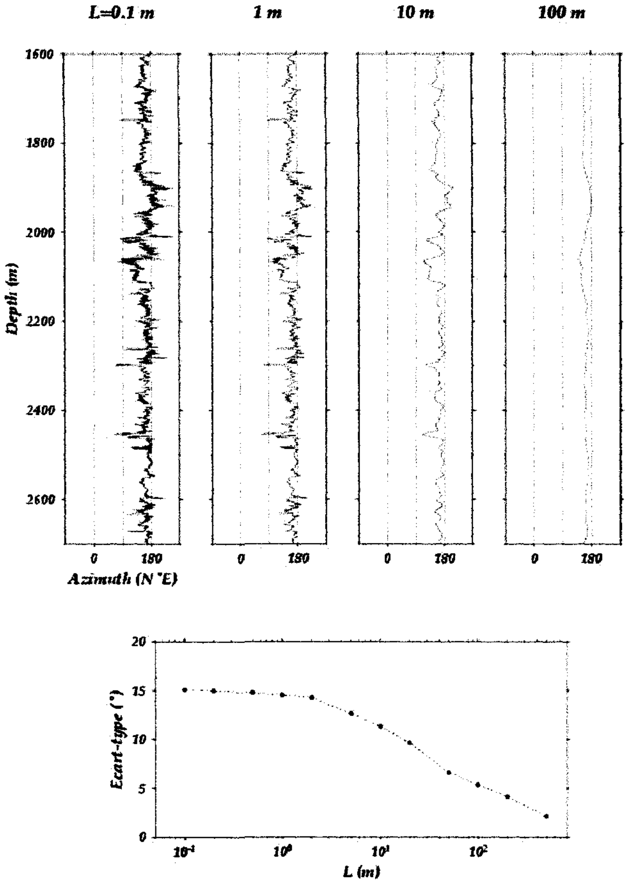

4. Induced seismicity along the Philippine Faults on the Island of Leyte:

The work presented in this section has been partly published :

Prioul R., F.H. Cornet, C. Dorbath, L. Dorbath, M. Ogena & E. Ramos, 2000, An induced seismicity experiment across a creeping segment of the Philippine Fault, Jou. Geophys. Res. , vol. 105, (June), p 13 595.

The material on anisotropy and focal mechanism inversion can partly be found in R Prioul Ph. D. Thesis (Sept. 2000, IPGP) : Apport de la sismicite induite a l'etude du comportement d'un segment d'un grand decrochement actif – La Faille Philippine. A publication is in preparation.

The Philippine fault is an active senestral strike slip fault, about 1200 km long, which has given rise to numerous earthquakes with magnitude larger than 7. However, in it central part, in Masbate and Leyte Islands, GPS measurements have shown displacements up to 3.5 cm per year, with only a very limited seismic activity. At the Tongonan geothermal site, on Leyte Island, the fault separates in two segments, with relative displacement of about 2.5 cm/y.

A large geothermal field located to the East of the fault has resulted in many wells being drilled, some for production, some for reinjection of brines produced at the plants. Many wells have been drilled for reinjecting the brines, either in between the two fault segments or through the faults themselves. These wells have revealed to be very impervious. They have also demonstrated that temperature west of the central fault segment drops rapidly from the 300 ° C value observed within the reservoir, about 1500m below ground level.

A large injection experiment, comparable to that conducted at Soultz, has been performed in well MG2RD which crosses the central fault segment around 1600 m below ground level. The well is cased down to 700 m and then lined with a slotted liner. A total volume of 36 000 m^3 has been injected at incremental flow rates, while induced microseismicity was monitored with a surface network.

For a period 18 months (February 1996, July 1997) the background microseismicity associated with the geothermal exploitation has been monitored with a 7 one-component (vertical) stations network. An additional 7 one-component network as well as four 3-componenets stations was installed for two two-month periods (October-November 1996 and June-July 1997). The injection experiment in MG2RD was conducted in June-July 1997 but injections linked to the reservoir exploitation occurred routinely during the duration of the recording.

Philippine Fault

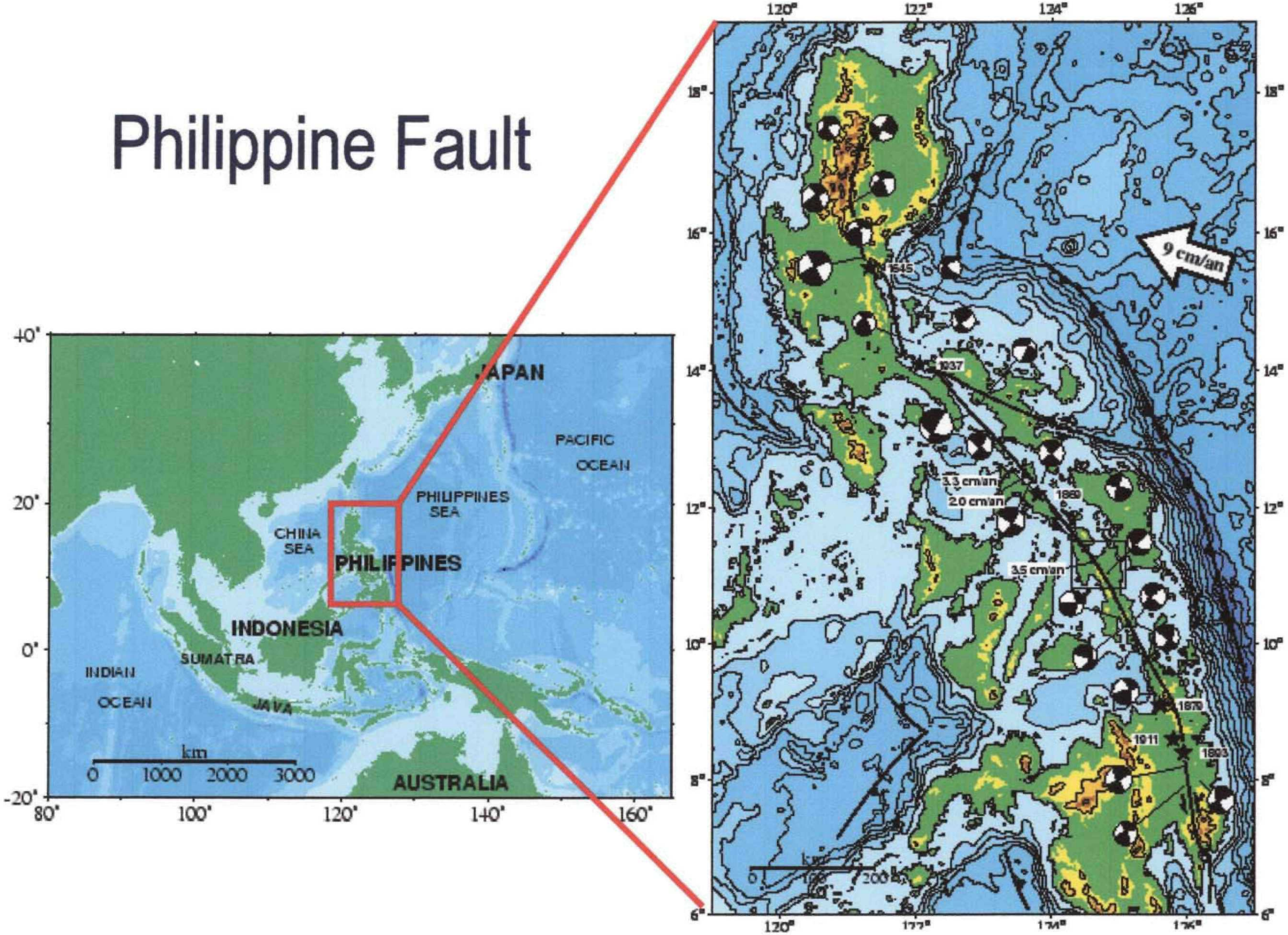

Philippine Fault on Leyte island

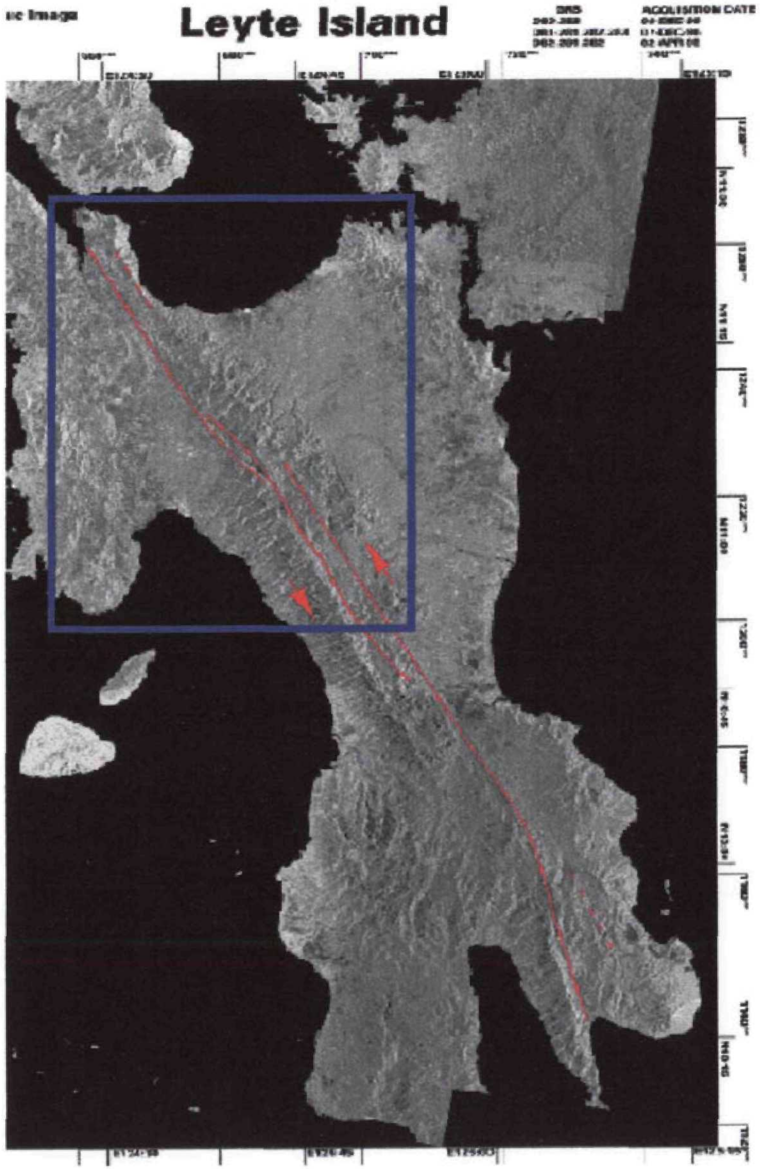

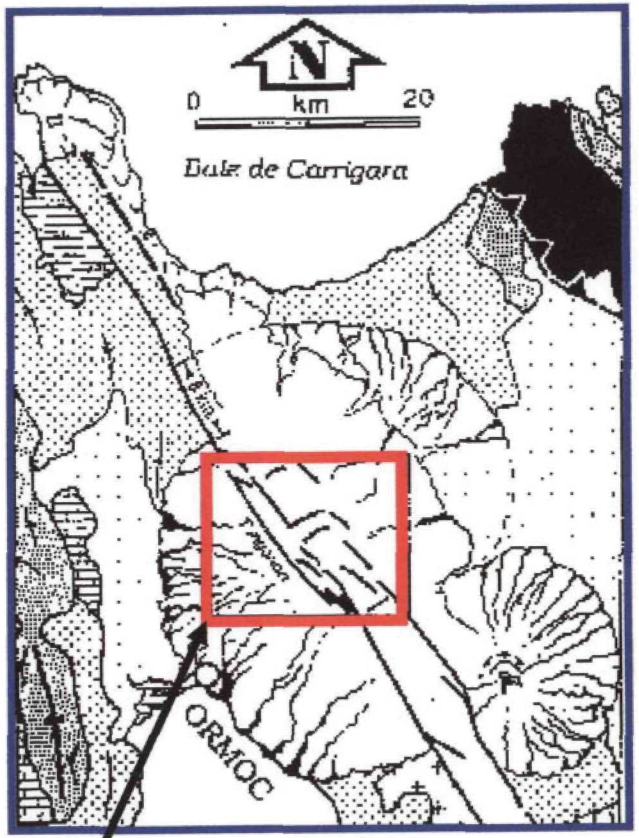

(Aurelio, 1992)

Tongonan geothermal field

Displacement field in the vicinity of the fault

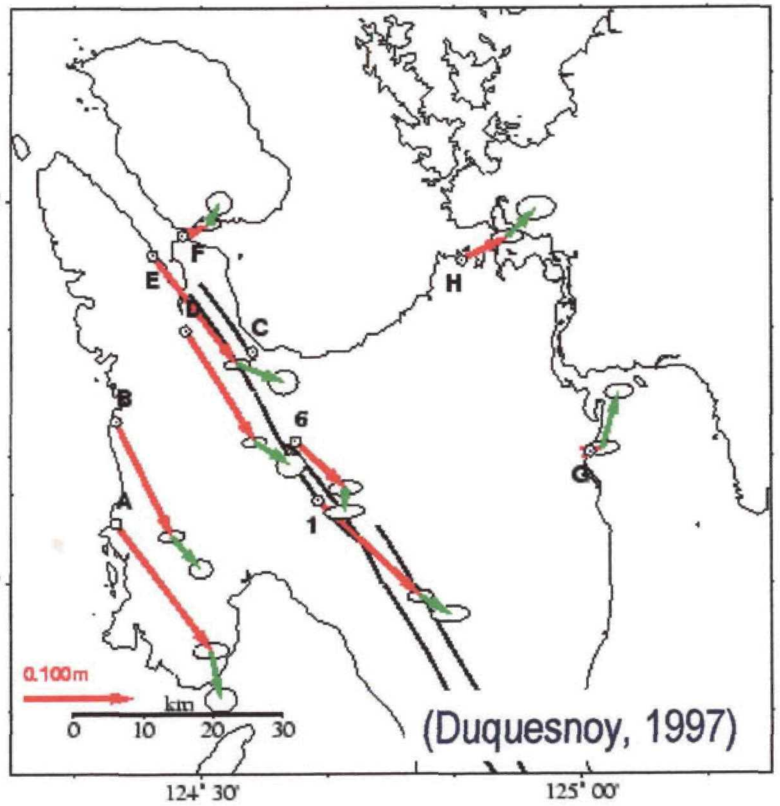

(Duquesnoy, 1997)

- GPS measurement 91-94-95
- 3.5 cm/y of creeping displacement

Seismicity

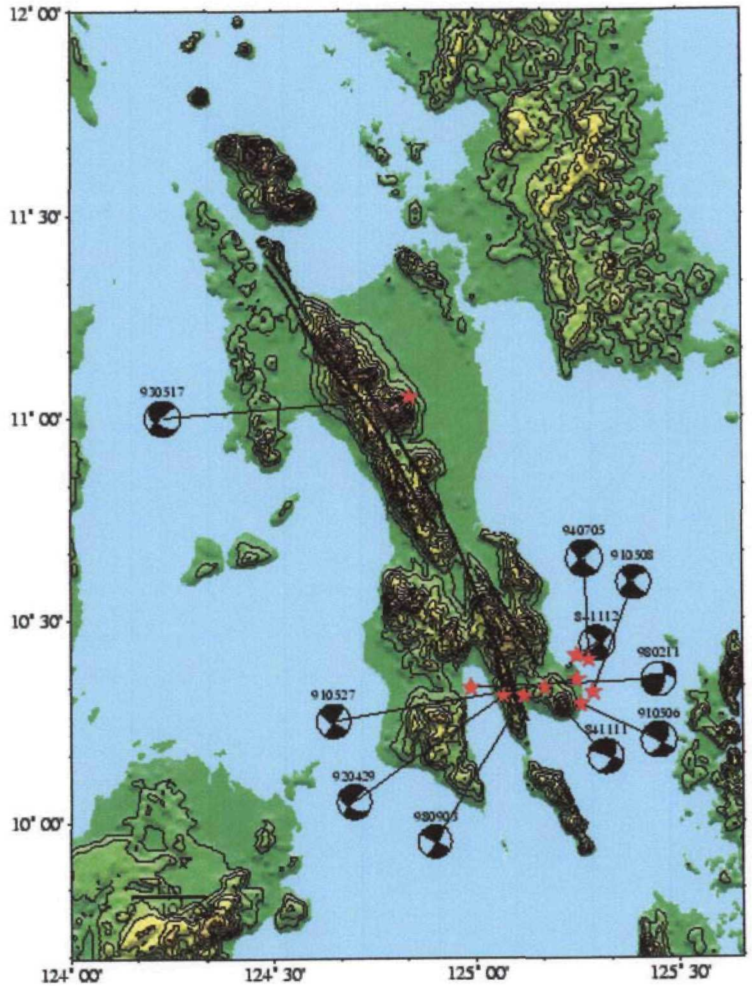

Displacement along the fault at Tongonan

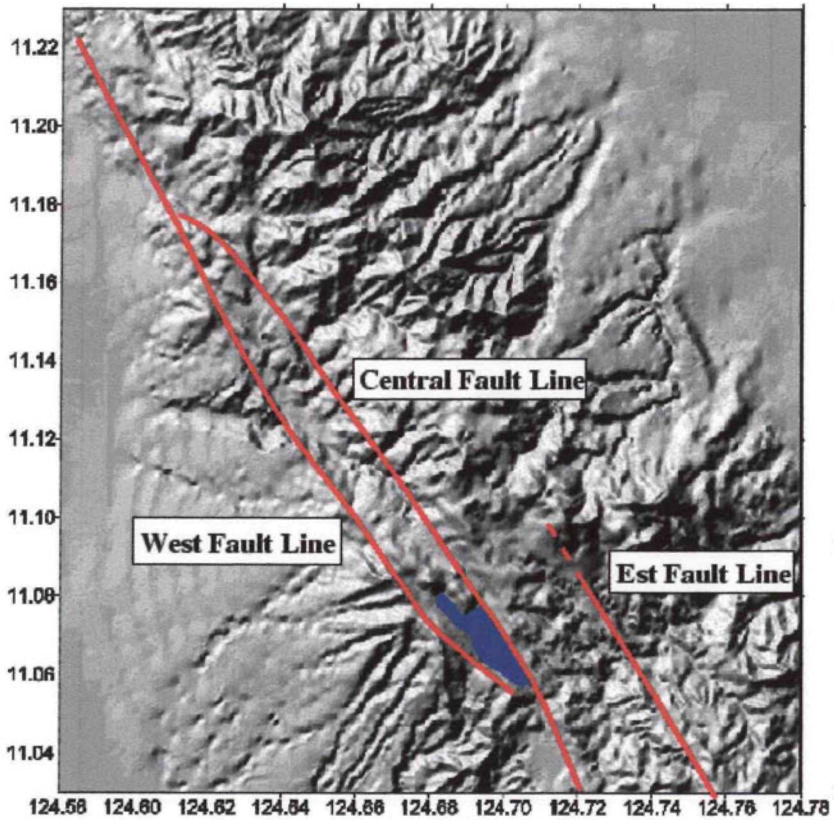

- Branches of Philippine Fault

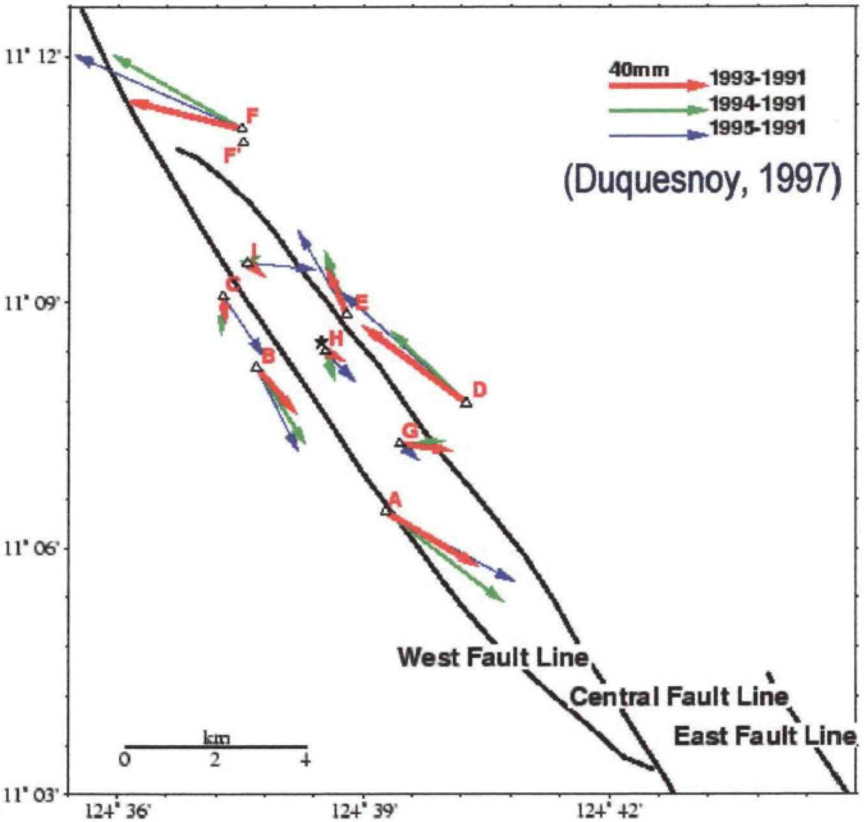

(Duquesnoy, 1997)

- 2.4 cm/y of creep displacement

Injection experiment (1)

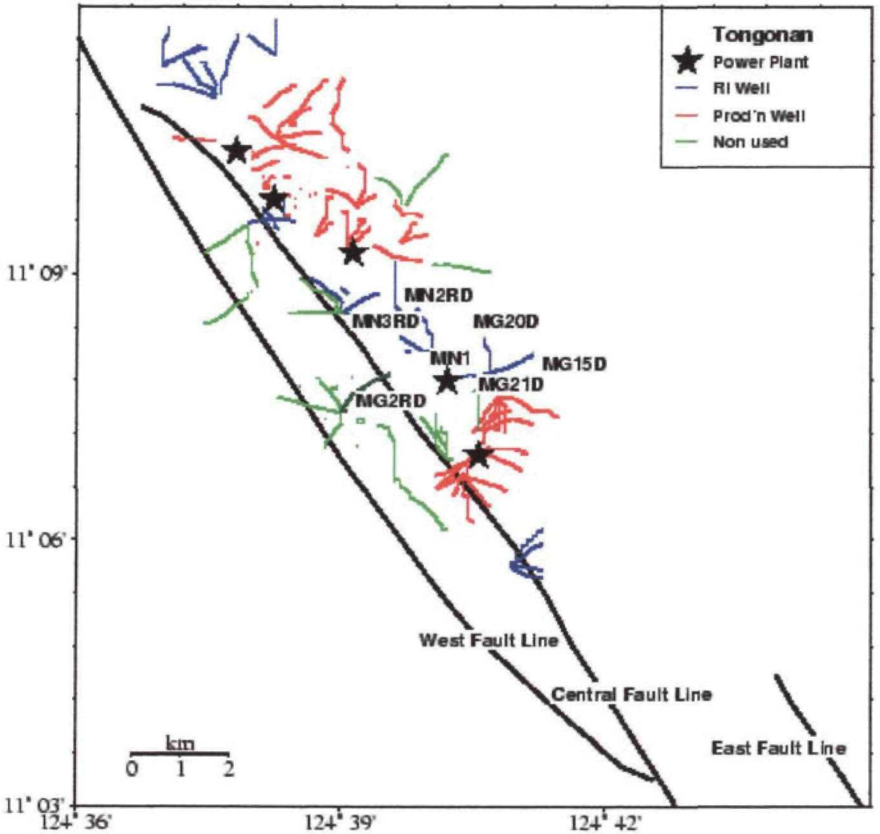

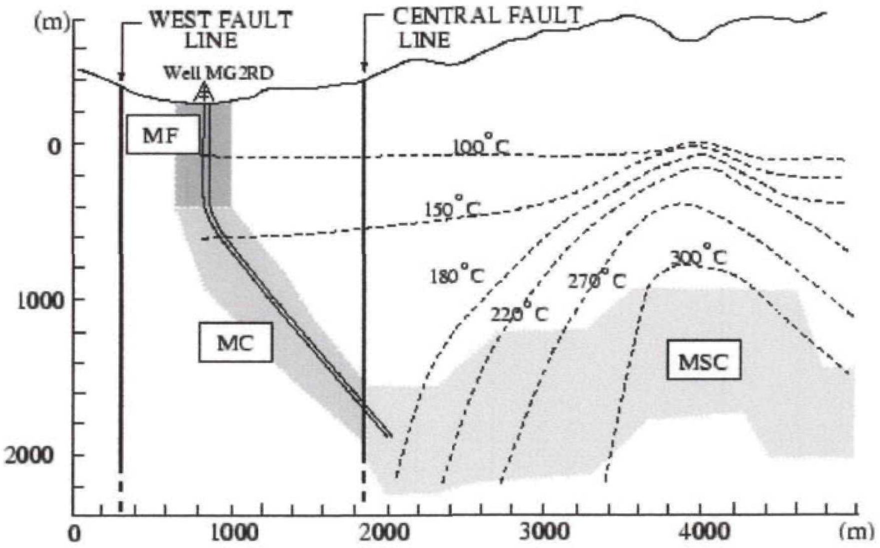

Injection experiment (2)

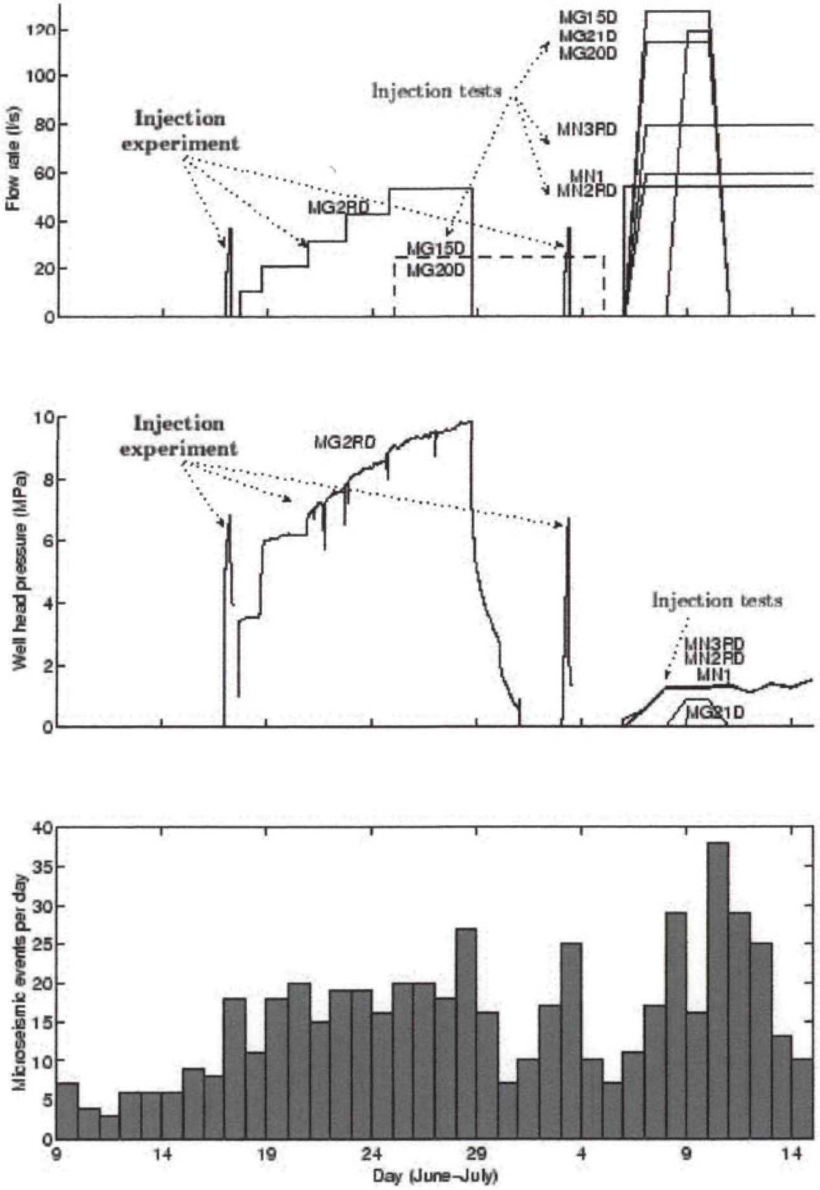

Injection experiment (3)

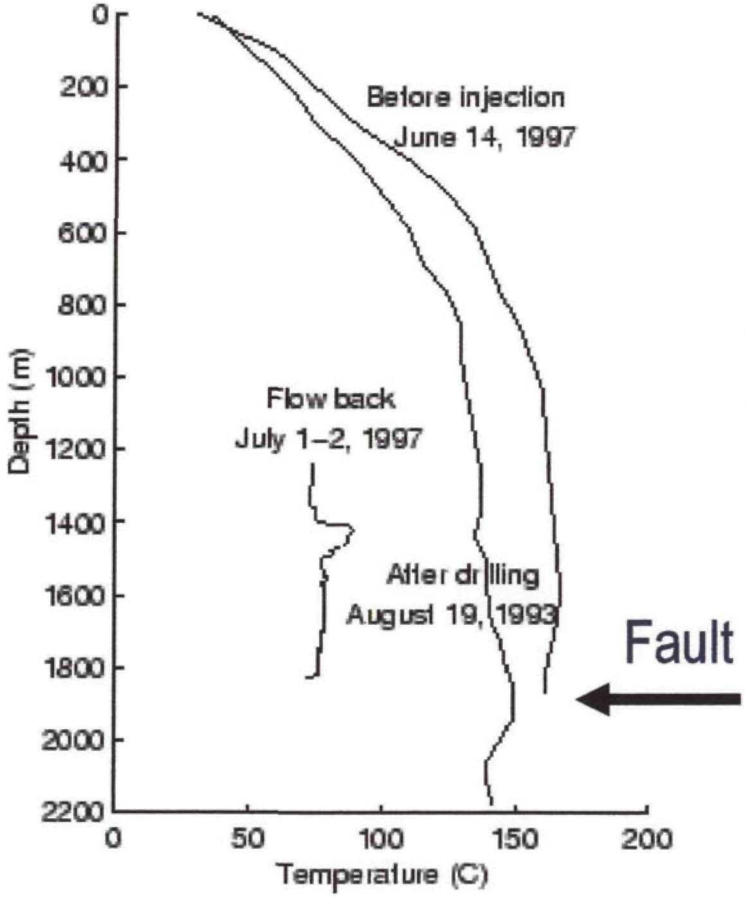

Summary of the observations:

- Water injected at the bottom of the well
- Well head pressure: up to 9 MPa
- Increase of microseismicity
- Injected volume: 36 000 m3
  (Other wells: 327 000 m3)

Seismicity acquisition

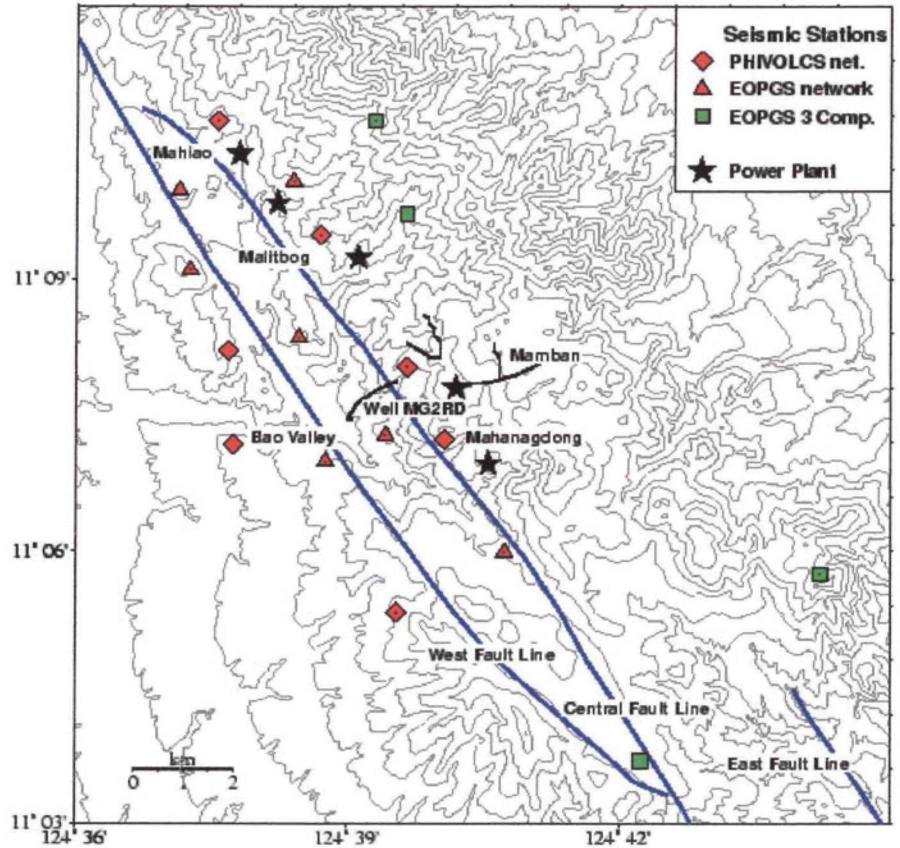

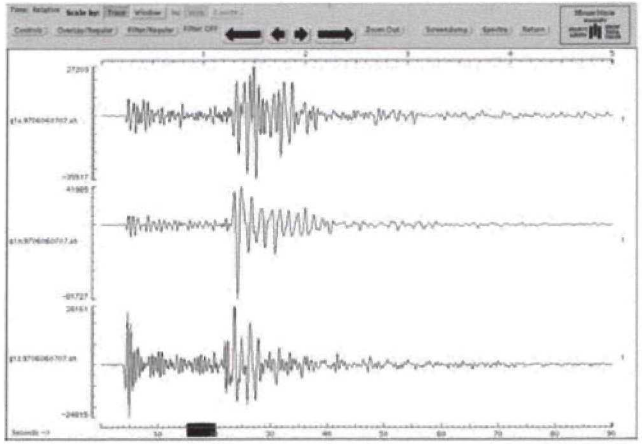

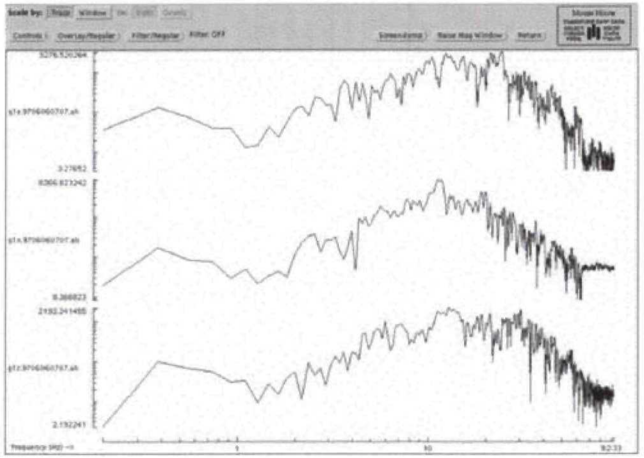

- Surface network (1-30 Hz)
- Feb. – Aug. 96 (Period 1) and Nov. – May 97 (Period 3): 7 stations
- Oct. – Nov. 96 (Period 2) and Jun. – Jul. 97 (Period 4): 18 stations (Four 3-C)

Tomographic inversion (1)

- Simultaneous determination of relocation and velocity model (Thurber, 1983)
- P and S traveltimes, 3-D grid with linear interpolation
- Iterative least squares inversion

Period 2: 141 ev. (1743 P, 1394 S) Period 4: 292 ev. (3939 P, 1352 S)

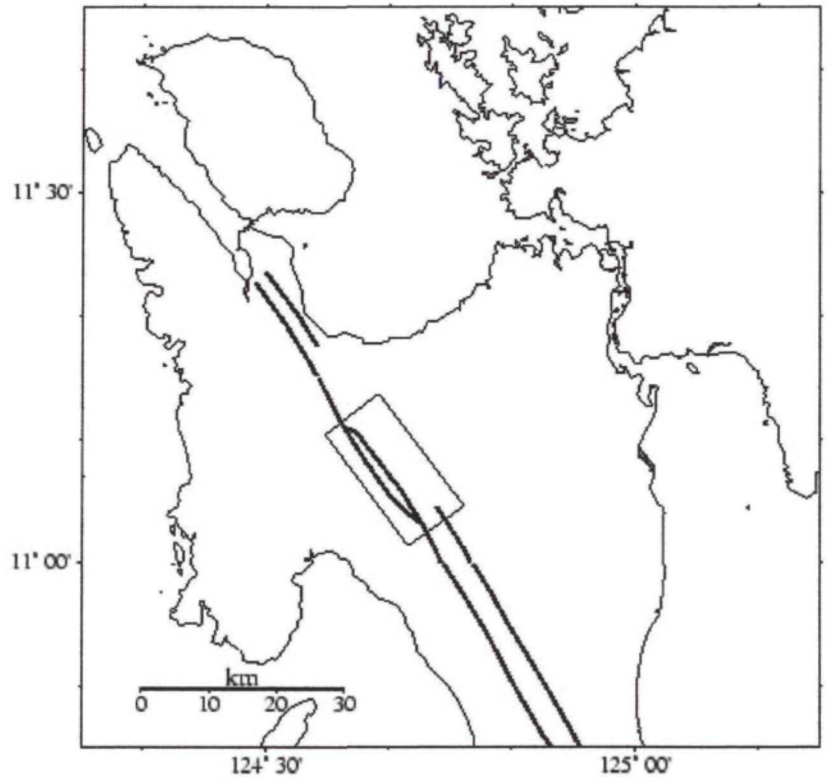

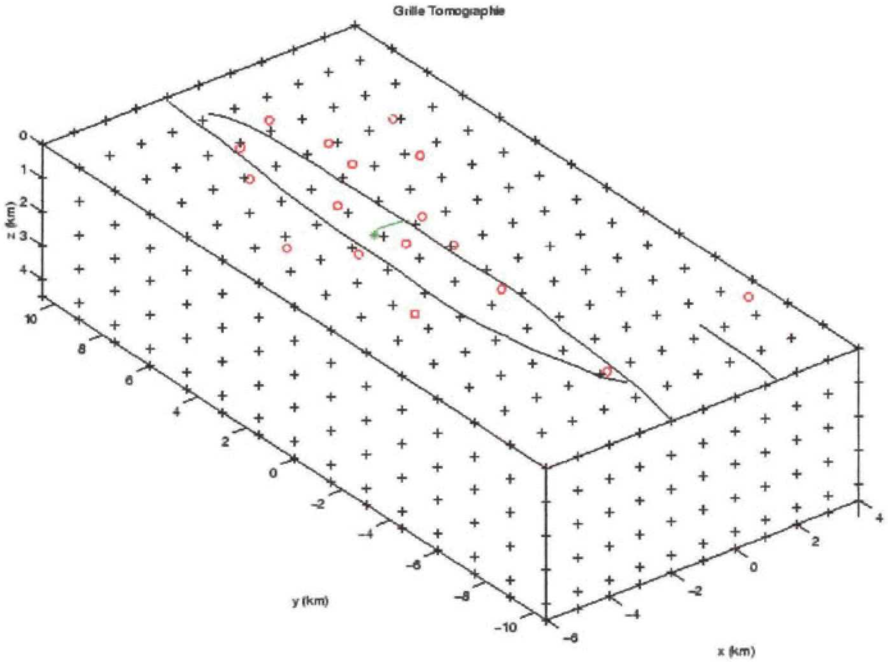

Induced microseismicity locations

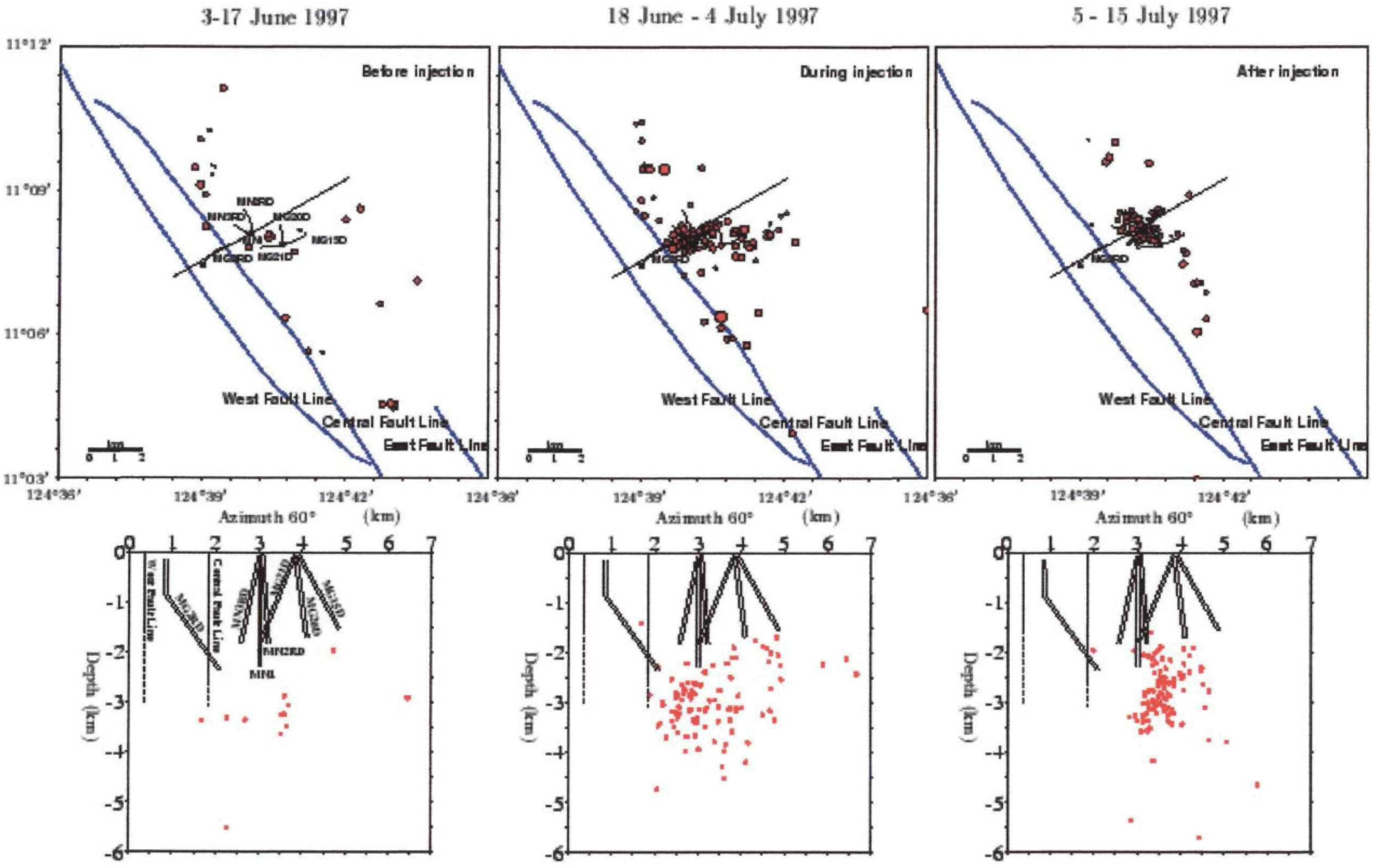

Seismicity relocations

Period 1+3 and 2

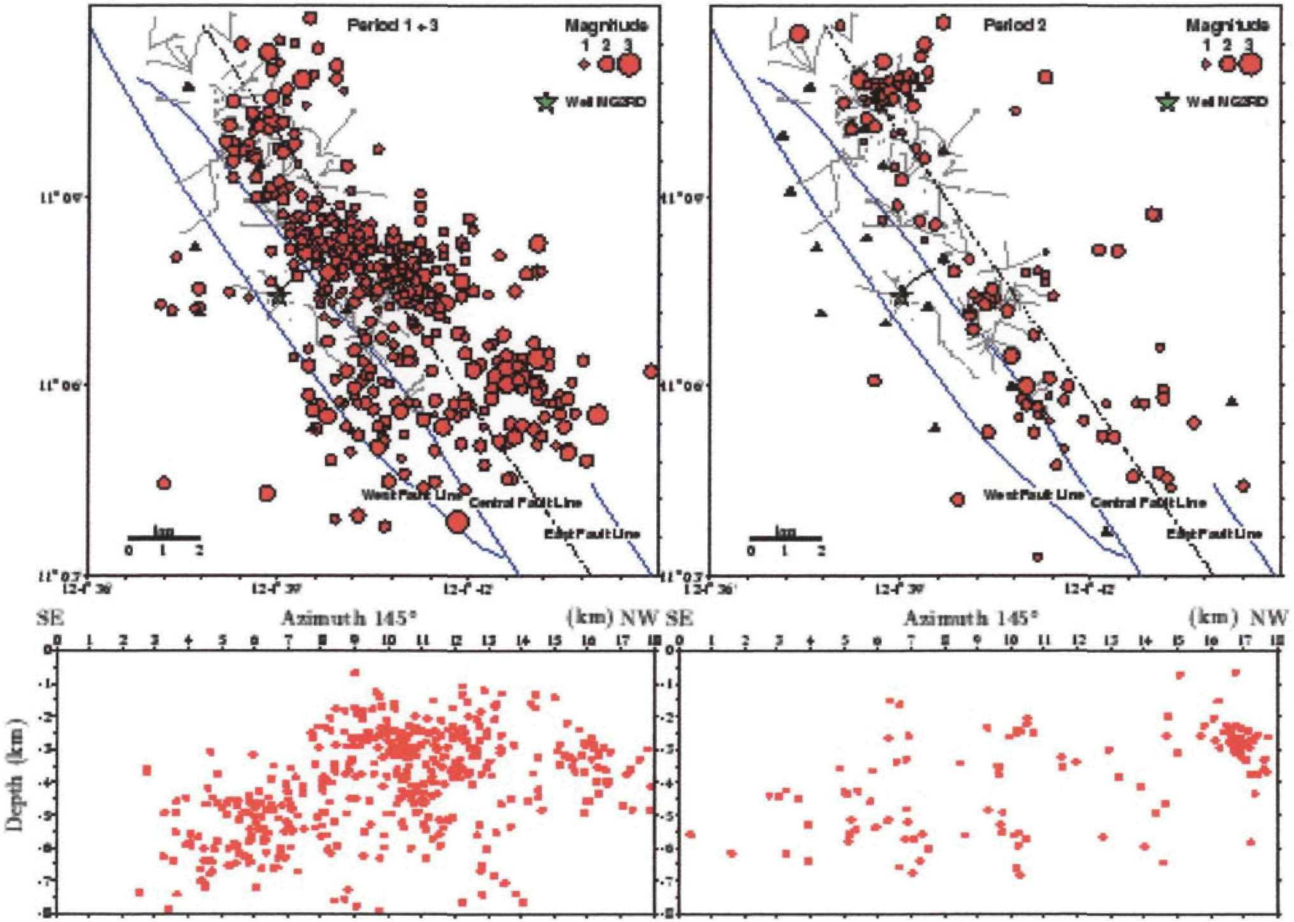

Vp velocity model (1)

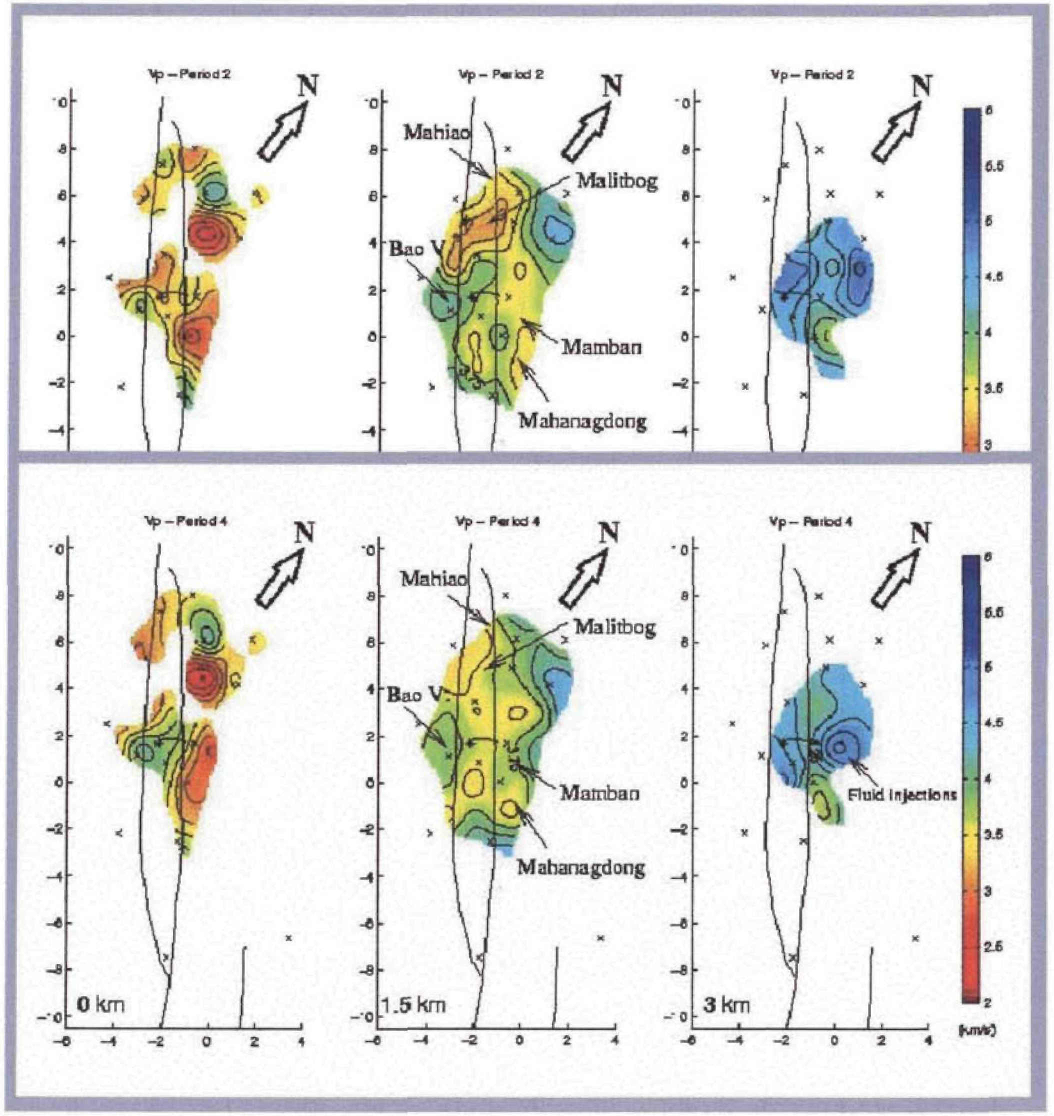

Before injection

After injection

Vp velocity model (2)

-before and during injection-

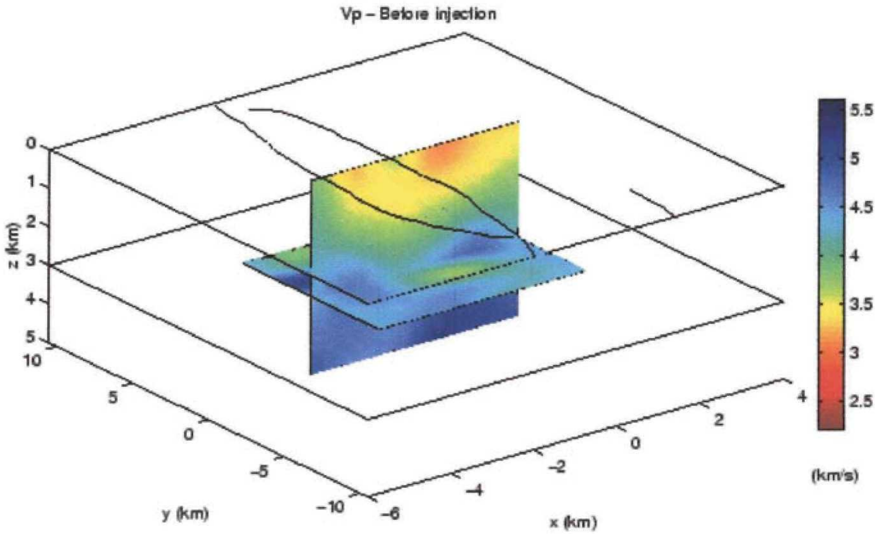

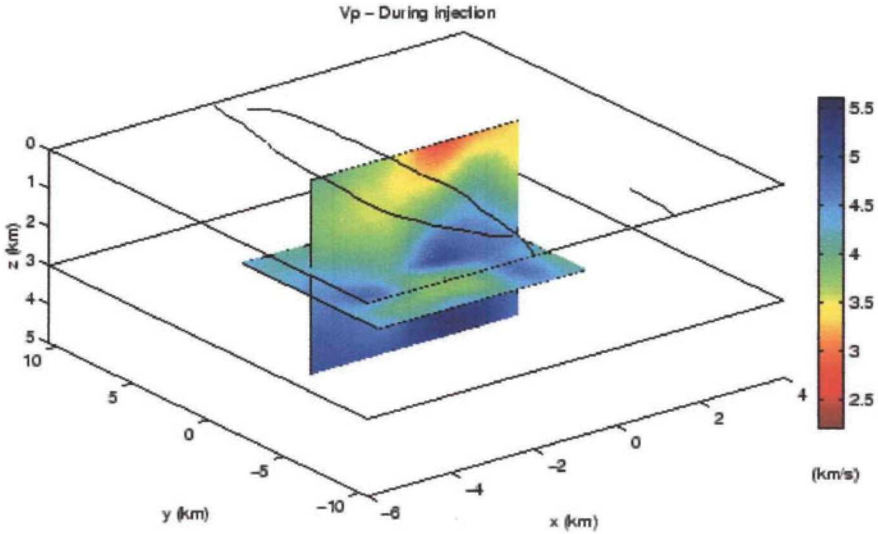

Focal mechanisms

Period 2

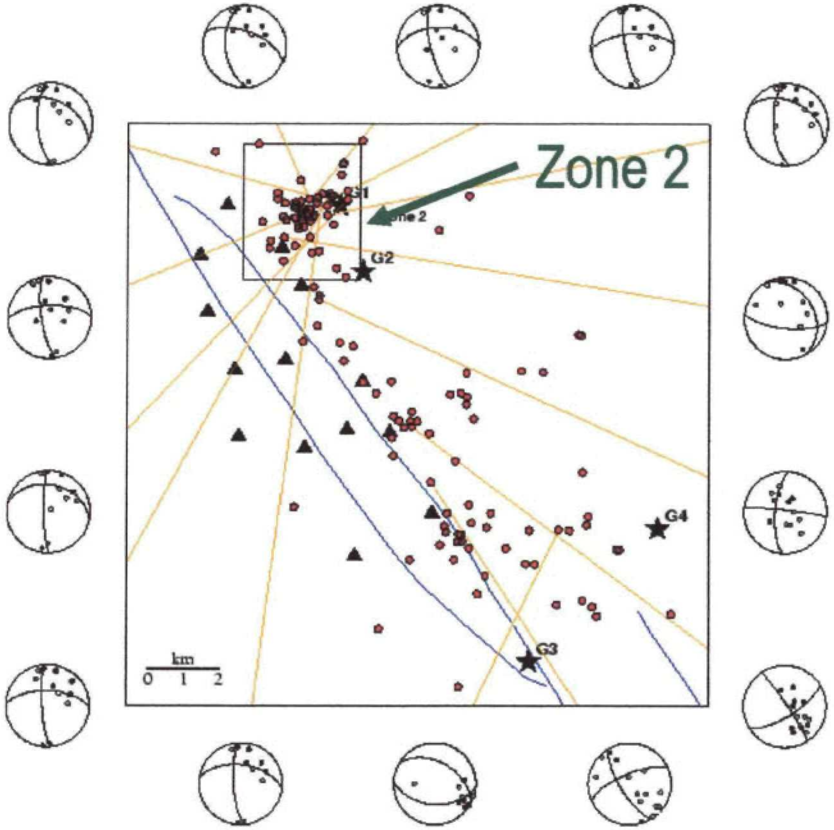

32 solutions

Period 4

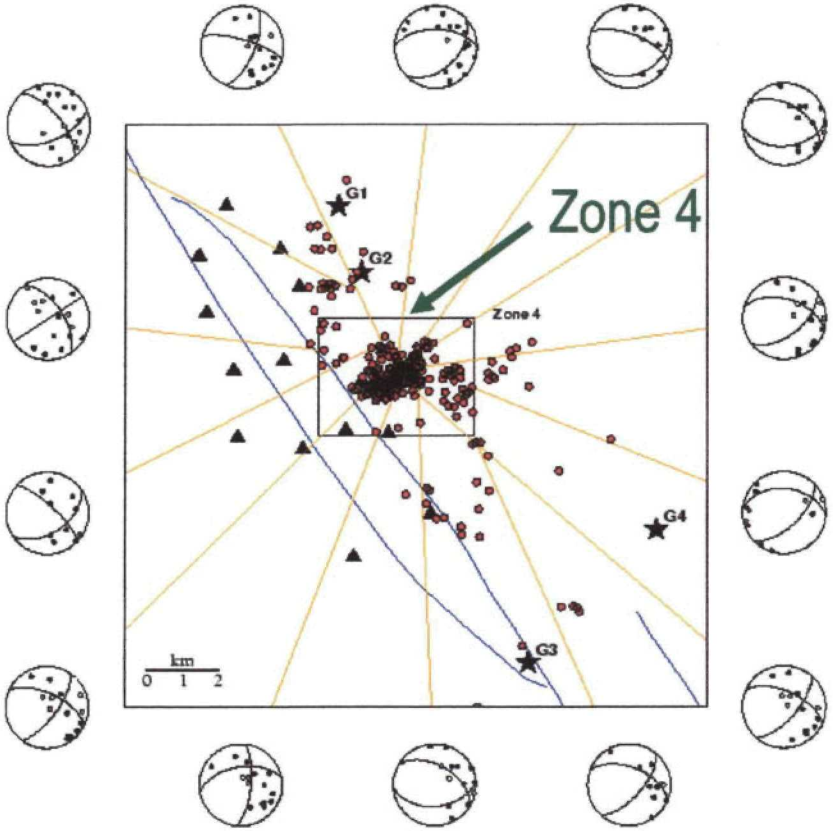

40 solutions

Focal mechanisms inversion

-first trial by zones-

Zone 2

23 focal mechanisms

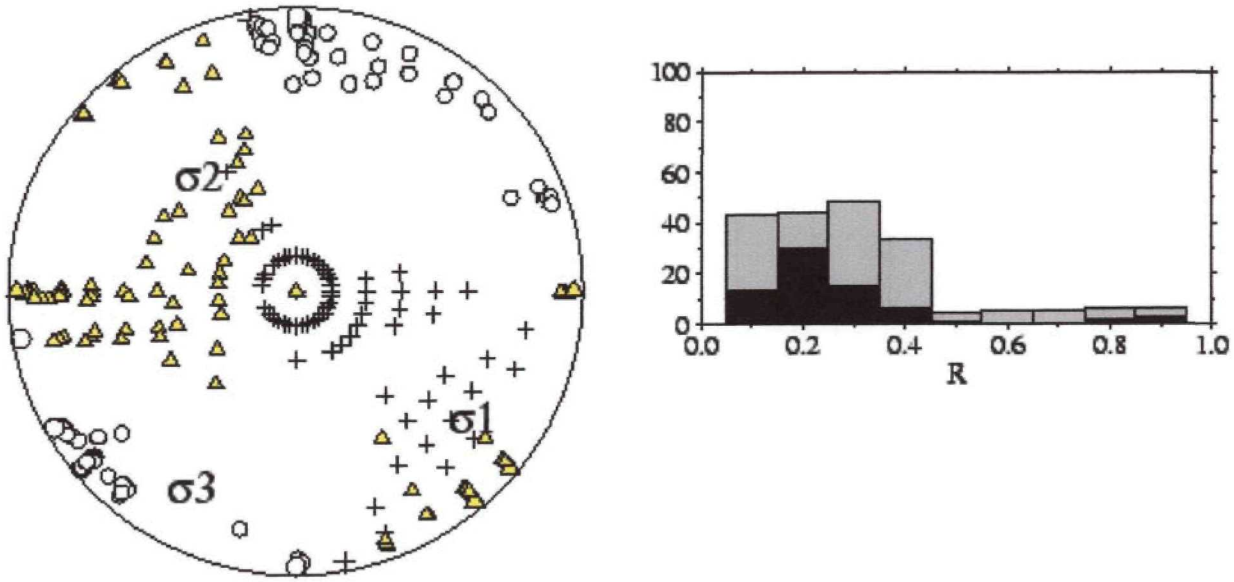

Solutions in 90 % confidence domain
Best solution compatible with 83 % of the data

Zone 4: no solution

Fast S- wave polarisations

-Period 2 and 4 -

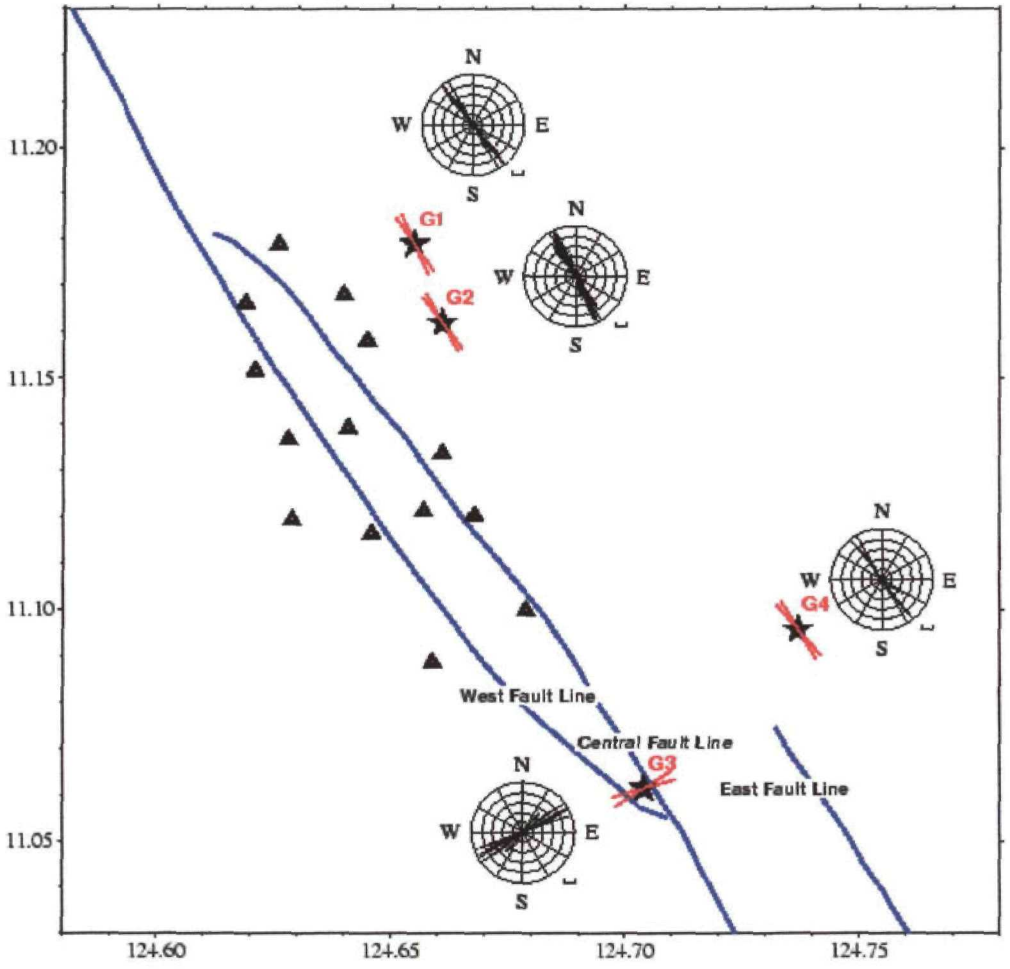

- Shear wave splitting
- G1, G2, G4: parallel to fault
- G3: orthogonal to fault

Stress heterogeneity in the seismicity cloud?

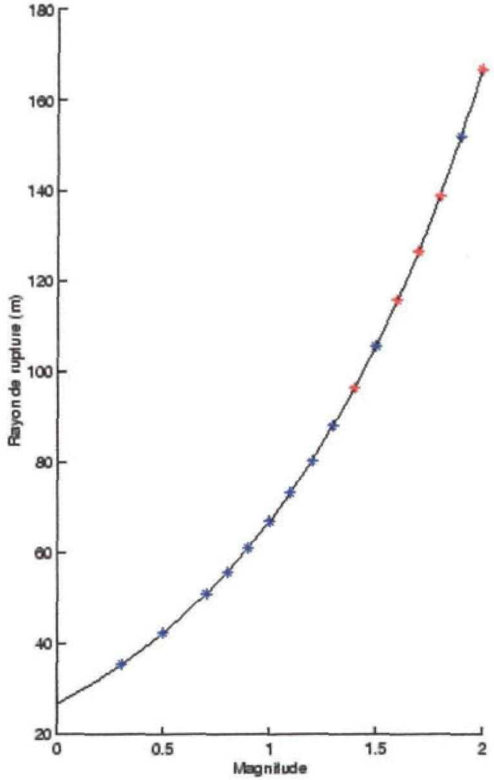

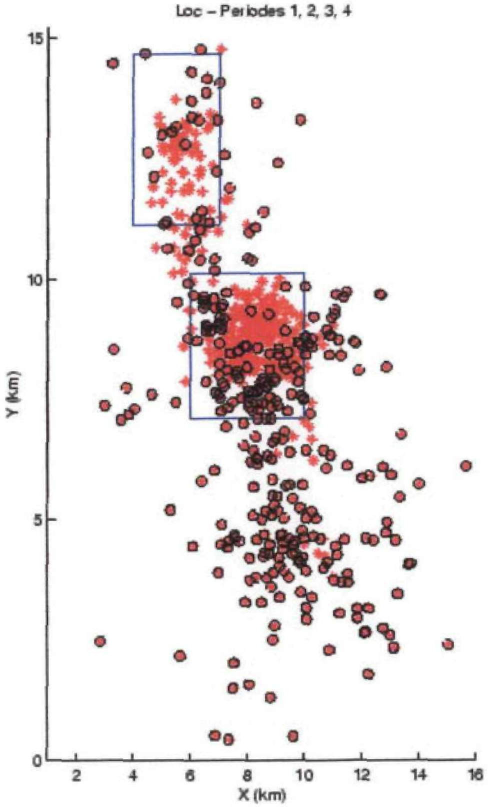

New data selection:

- Definition of a sphere for each event with radius~rupture dimension
- Successive events with intersecting spheres are excluded

Focal mechanisms inversion

-new data selection-

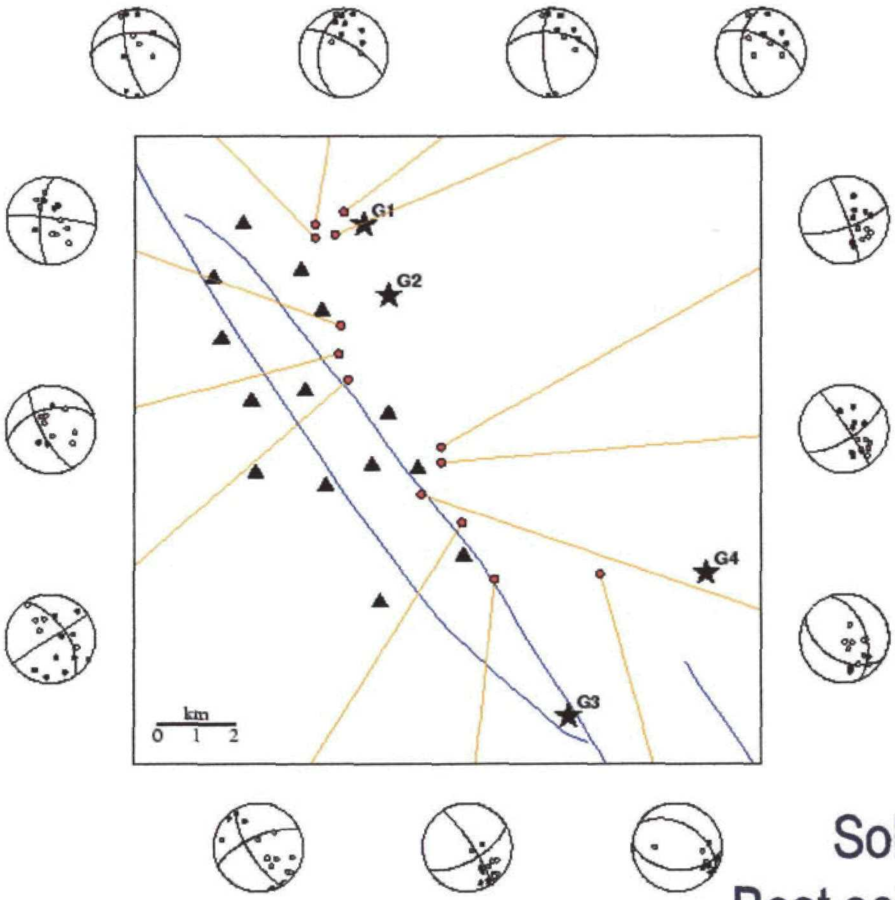

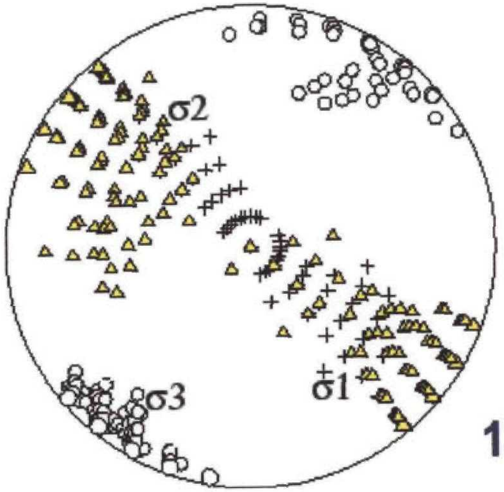

13 foc. Mech.

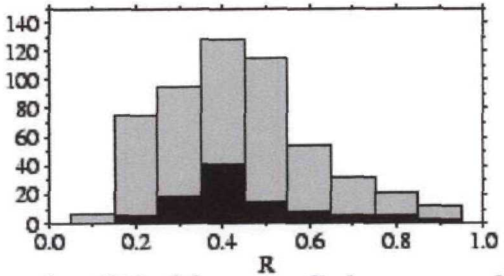

Solutions in 90 % confidence domain

Best solution compatible with 91 % of the data

Fast S- wave polarisations

-east of the Central Fault (G1, G2, G4) -

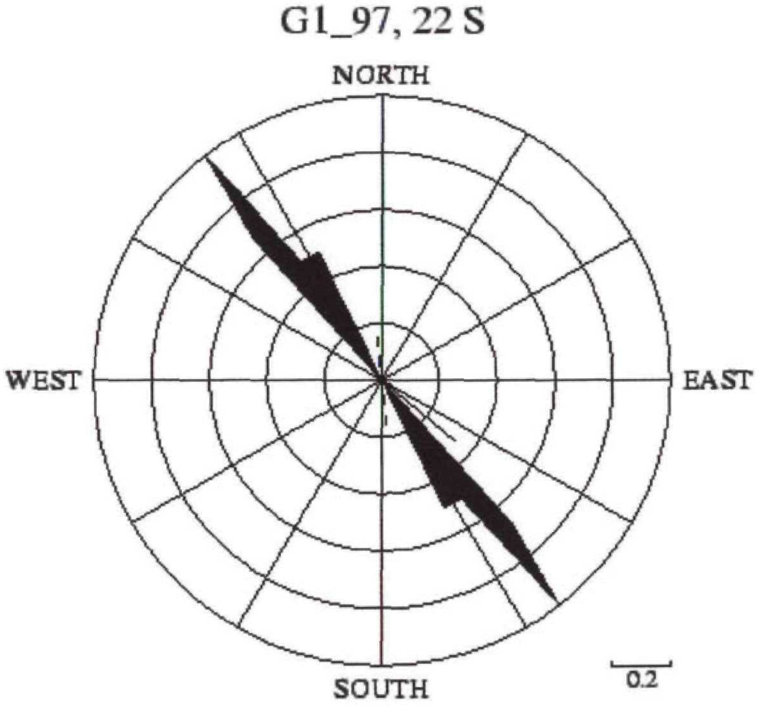

Fast polarisation ~ 145 deg.

Inversion focal mechanisms

-new selection-

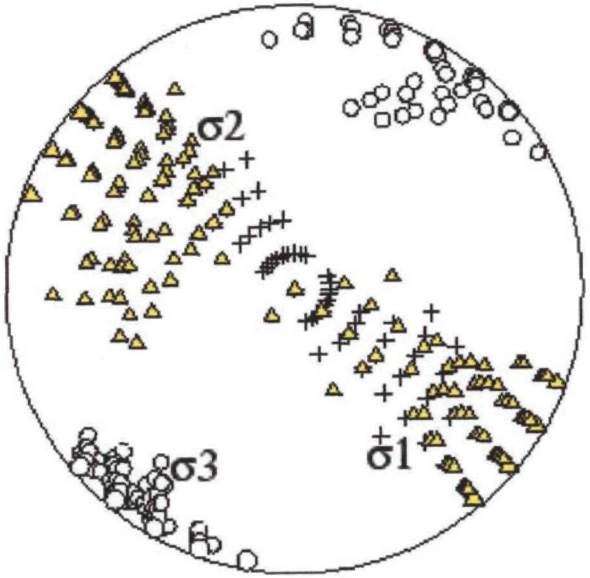

$\sigma1$ and $\sigma2$ ~ 110-150 deg.

Observations compatibility in regional context

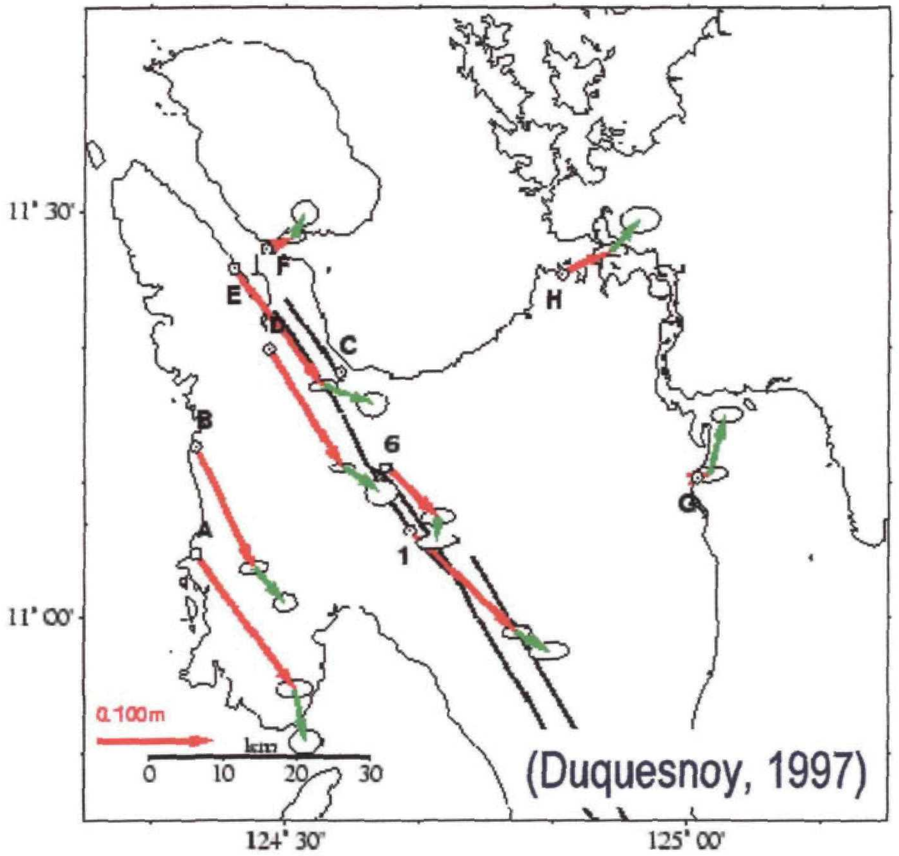

(Duquesnoy, 1997)

- Minimum principal stress orthogonal to fault
- GPS data show extention orthogonal to fault ~0.6-1.8 cm/y

Extension basins along the fault

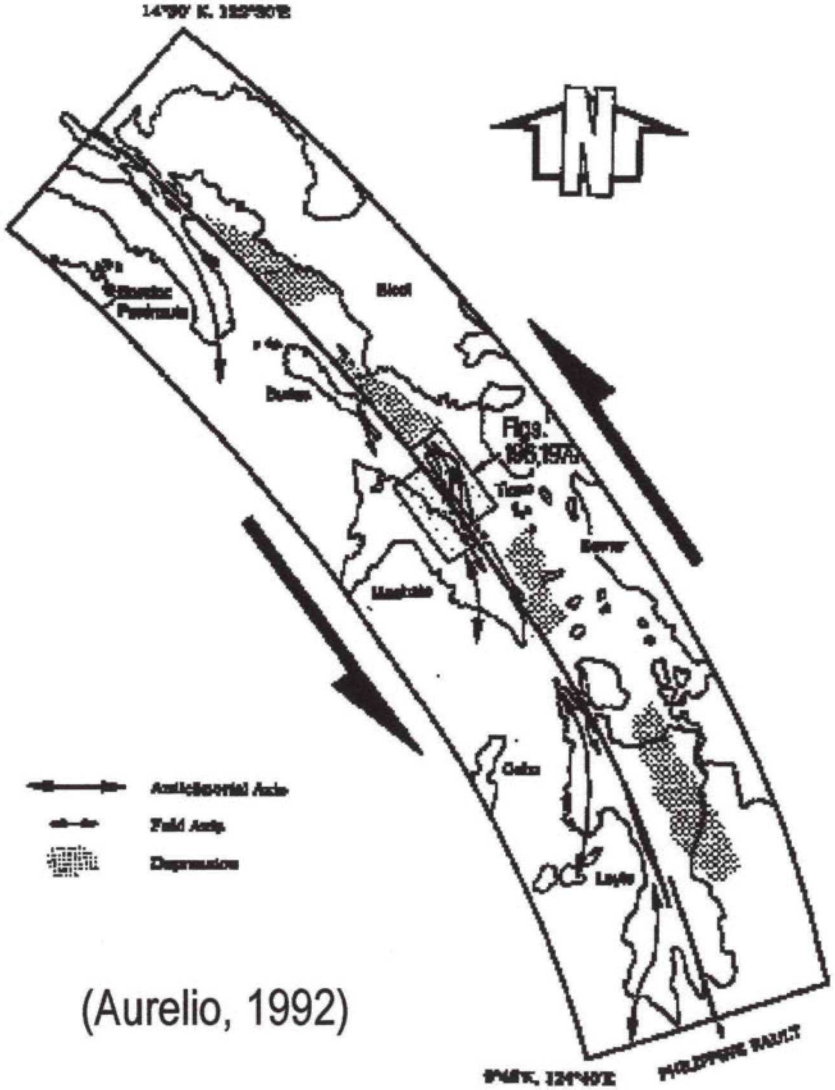

(Aurelio, 1992)